3-D Global Hybrid Simulations of Mode Conversion at the Dayside Magnetopause

by

Feng Shi

A dissertation submitted to the Graduate Faculty of
Auburn University
in partial fulfillment of the
requirements for the Degree of
Doctor of Philosophy

Auburn, Alabama
May 3, 2014

Keywords: mode conversion, magnetopause, KAWs, magnetospheric physics

Approved by

Yu Lin, Chair, Professor of Physics
Joseph D. Perez, Professor of Physics
Edward E. Thomas, Professor of Physics
Kaijun Liu, Assistant Professor of Physics

Abstract

Mode conversion at the magnetopause has been suggested to lead to the generation of kinetic Alfvén waves (KAWs) and effective mass transport from the solar wind into the magnetosphere. To investigate the mode conversion process in the dynamics dayside system, a systematic 3-D global hybrid simulation that includes the solar wind, bow shock and the geomagnetic field is carried out for the dayside magnetosphere under various interplanetary magnetic field (IMF) conditions. In the quasi-parallel (Q-$\|$) shock, the foreshock compressional pulses are self-consistently generated by the interaction between the solar wind and the dipolar geomagnetic field. The simulation results show that as the compressional pulses propagate from the magnetosheath to the magnetopause, short wavelength structures of $k_\perp \rho_i \sim 1$ with enhanced parallel electric field $E_\|$ are excited in the magnetopause boundary layer (MPBL), where $k_\perp \sim k_x$ is the perpendicular wave number nearly along the GSE x direction, and ρ_i is the ion Larmor radius. The wave phase relationship between the magnetic field and the density changes from in-phase in the magnetosheath to anti-phase in the short-wavelength MPBL perturbations. The wave polarization is predominantly compressive in the magnetosheath, whereas strong transverse wave powers appear abruptly around the MPBL. The mode conversion from the compressional pulses to KAWs is identified around the predicted Alfvén resonance points in the MPBL. As these KAWs evolve, KAW modes dominated by azimuthal wave number with $k_y \rho_i \sim 1$ are also generated. The short-wavelength KAWs in the MPBL are identified by the sharp increases in $E_\|$ and the transverse electromagnetic field polarization relation of Alfvén mode. These KAW perturbations propagate poleward into the cusps along the MPBL. Due to the differential flow convection speeds at various latitudes, the KAW packets expand along the north-south direction, while they may also merge with newly formed KAWs generated by newly-arrived compressional waves.

The mode conversion takes place downstream of the Q-$\parallel$ shock, where the driver compressional waves are the strongest in their global distribution. In the cases with a radial IMF, the mode conversion takes place in the subsolar region. In the cases with a more general IMF direction, the Q-$\parallel$ shock regions and thus the strongest mode conversion shift off the subsolar, although the KAWs may still be identified near the subsolar region around the MPBL. In the dipole field region of the magnetosphere, field line resonance associated with the standing shear Alfvén waves is found due to the mode conversion. In the presence of the IMF B_y component, the field line oscillations in the inner magnetosphere are more intense downstream of the Q-$\parallel$ shock than on the quasi-perpendicular (Q-$\perp$) side, indicating again that the KAWs from the mode conversion is in favor of the Q-$\parallel$ side. Over several periods of incoming magnetic pulses, the KAWs approximately show a symmetric pattern from north to south. This symmetry, however, is not observed in the existence of the northward component (B_z in GSM) in the IMF, because the Q-$\parallel$ is now located in the southern hemisphere where more KAWs could be perceived. While observational signatures are provided by the global simulation, the simulation results are also compared with satellite observations for the physical evidence of mode conversion.

Acknowledgments

First of all, I would like to express my heartfelt gratitude to my adviser Dr. Lin, who guided me through every step of this research topic and dissertation by instruction, enlightening and conscientious professing. Without her guidance and inspiration, I would never have been able to achieve my dream of academic goals. I even want to write down a couple of pages to express my sincere gratitude from my heart, but, instead, I would like to keep them in my mind as always.

Secondly, I would like to present a very special thanks to Dr. Xueyi Wang. Not only does he set me a brilliant example with his vast knowledge and skills in my research field, but his invaluable instructions and comments do contribute enormously to my research.

Next, I would like to give my sincere gratefulness to Dr. Perez, Dr. Liu, Dr. Thomas, and other professors and staff at the Physics Department, who have been extremely supportive and provide a friendly and academic environment while pursuing my PhD degree. Thanks again every single committee member and Dr. Zeng for taking their precious time to review this dissertation.

Besides, I would also like to extend my deep appreciation to Dr. Binying Tan, my senior sister, who explained me the computational model in great detail, to Dr. Yong Hu, my collaborator in solid state physics and currently an associated professor in Northeastern University of China, who helped me considerably in my basic understanding in the physics of condensed matter, to Dr. Wei Jiang, my collaborator in plasma community and currently an associated professor in Huazhong University of Technology, who offered me constructive suggestions always, and to Dr. Wei Kong, my another collaborator in plasma physics field and also currently an associated professor in Civil Aviation University of China, who passed on valuable advices which encouraged me through my research.

Last but not least, I would like to thank my parents faithfully and heartfully, as well as all my beloved friends, for their full support for helping me throughout this long but fulfilling journey ever since.

Table of Contents

List of Figures

List of Abbreviations

1-D	one-dimensional
2-D	two-dimensional
3-D	three-dimensional
HLBL	high-latitude boundary layer
IMF	interplanetary magnetic field
KAW	kinetic Alfvén wave
LLBL	low-latitude boundary layer
MHD	magnetohydrodynamics
MPBL	magnetopause boundary layer
ULF	ultra-low frequency

Chapter 1

An Introduction to Mode Conversion Processes

The primary goal of this chapter is to equip readers with essential background knowledge and to make the dissertation a complete composition of the following chapters.

1.1 What is Plasma

It has often been said that 99% of the matter in the universe is in the plasma state; that is, in the form of an electrified gas with the atoms dissociated into positive ions and negative electrons. Such an estimate may not be quite accurate, but it is definitely a reasonable one in the view of the fact that stellar interiors and atmospheres, gaseous nebulae, and much of the interstellar hydrogen are plasmas. In our daily lives, the occurrence of the plasmas is limited to a few examples: the flash of a lightning bolt, the glow of the Aurora Borealis, the conducting gas inside a fluorescent tube or neon sign, and the slight amount of ionization in a rocket exhaust. From our living planet of the Earth, however, as soon as one leaves its atmosphere, one encounters the plasma comprising the Van Allen radiation belts and the solar wind.

Plasmas, consisted of positively and negatively charged particles with approximately equal charge densities, can be produced by heating an ordinary gas to such a high temperature that the random kinetic energy of the molecules exceeds the ionization energy; i.e., the molecules or atoms are ionized. Because the ionization process starts at a fairly well-defined temperature, usually a few thousand K, a plasma is often referred to as the "fourth" state of matter, in distinction to the first three states of matter: solid, liquid and gas. The steady

state ionization density depends on a balance between ionization and recombination. In order to maintain a high degree of ionization, either the ionization source must be very strong, or the plasma must be very tenuous so that the recombination rate is low.

The definition of a plasma requires that any deviation from charge neutrality must be very small, which means the charge neutrality condition is equivalent to requiring that the electron and ion number densities be approximately the same. In the absence of a loss mechanism, the overall charge neutrality assumption is usually satisfied because all ionization processes produce equal amounts of positive and negative charge. However, deviations from local charge neutrality can occur. Systems that display large deviations from charge neutrality, such as vacuum tubes and various electronic devices, are not plasmas, even though some aspects of their physics are similar.

To be a plasma, the charged particles must be in an unbound gaseous state. This requirement can be made more specific by requiring that the random kinetic energy be much greater than the average electrostatic energy, and is imposed to provide a distinction between a plasma, in which the particles move relatively freely, and condensed matter, such as metals, where electrostatic forces play a dominant role. In a plasma, long range electric forces are much more important than short range ones. Because many particles feel the same long range forces, a plasma is dominated by collective motions. The long range forces acting on these charged particles make a plasma distinctively different from the ordinary gases mainly composed of neutral particles.

Broadly speaking, plasmas can be divided into two categories: natural and man-made. It is an interesting fact that most of the material in the visible universe, as mentioned at the very beginning, is in the plasma state. Of these the former are the majority, which includes most of the stars and a significant fraction of the interstellar medium; on the other hand, almost all the laboratory plasmas, such as glow discharged "gas" in fluorescent tube mentioned previously, belong to the latter. From this point of view, plasmas play a major role in the universe. Plasma physics is relevant to the formation of planetary radiation belts,

the development of sunspots and solar flares, the acceleration of high velocity winds that flow outward from the Sun the other stars, the generation of radio emissions from the Sun and other astrophysical objects, and the acceleration of cosmic rays.

In the Earths atmosphere, the low temperatures and high pressures that are commonly present are not favorable for the formation of plasmas except under unusual conditions. Probably, the most common plasma phenomenon encountered in the Earths atmosphere is lightning. In a lightning discharge the atmospheric gas is ionized and heated to a very high temperature by the electrical currents that are present in the discharge. Because of the high recombination rate the resulting plasma exists for only a small fraction of a second. Less common is ball lightning, which consists of a small ball of hot luminous plasma that lasts for up to tens of seconds. Another terrestrial plasma phenomenon, readily observable at high latitudes, is the aurora, which is produced by energetic electrons and ions striking the atmosphere at altitudes of 80 to 100 km. At higher latitudes, from one hundred to several hundred km, the Earth is surrounded by a dense plasma called the ionosphere. The ionospheric plasma is produced by ultra violet radiation from the Sun, and also exists on the night side of the Earth since the recombination rate is rather low at high latitudes. The ionosphere plays an important role in radio communication by acting as a reflector for low frequency radio waves. At even higher altitudes, the Earth is surrounded by a region of magnetized plasma called the magnetosphere. Planetary magnetospheres have now been observed at all the magnetized planets and exhibit many of the plasma processes that are believed to occur at magnetized astronomical objects such as neutron stars.

Numerous applications of basic plasma physics can be found in man-made devices. One of the most important of these is the attempt to achieve controlled thermonuclear fusion. Since fusion requires a temperature at least of $10^7 K$ to overcome the Coulomb repulsion between nuclei, controlled fusion necessarily involves very high temperatures. Because fusion plasmas would be quickly cooled by the walls of any ordinary container, considerable effort has gone into attempts to confine plasmas by magnetic fields. Although the principles of such

magnetic confinement may appear at first glance to be straightforward, attempts to achieve controlled fusion using magnetic confinement have been complicated by collective effects that develop when large numbers of particles are introduced into the machine. The effort to find a technologically and economically attractive configuration for confining a dense, hot plasma requires one of the main challenges of fusion research. In addition to fusion, numerous other devices involving plasmas exist as well. Fluorescent lights and various other devices involving plasma discharges, such as electric arc welders and plasma etching machines, are commonly in daily use. More advanced devices involve magnetohydrodynamic generators for producing electricity from high temperature gas jets, ion engines for spacecraft propulsion, various surface treatment processes that involve the injection of ions into metal surfaces, and high frequency electronic devices such as traveling wave tubes and magnetrons.

1.2 What is Mode Conversion

Plasma transport of mass, momentum and energy, as well as its heating, has been described as one of the most important issues in the plasma physics community. So far as known, all the possible means of plasma heating and transport by electromagnetic waves, which rely on collisionless dissipation, e.g. through lower hybrid resonance [9], ion cyclotron resonance [10] and parametric excitation [11], have much shorter wavelengths and intrinsic difficulties in pumping the wave energy to the plasma on a large spatial and temporal scales. In contrast, the resonance of shear Alfvén waves occurs on a much longer wavelengths and thus has been of great interest [6, 12, 13].

Alfvén wave, named after Hannes Alfvén, is a fundamental physical phenomenon in all kinds of magnetized plasmas [14]. From magnetohydrodynamics (MHD) in uniform plasmas, the hydromagnetic waves travel along ambient magnetic field at a constant velocity V_A, called the Alfvén velocity/speed, and $V_A = B/(\mu_0\rho)^{1/2}$. This is a characteristic velocity at which perturbations of the lines of force travel. This Alfvén wave mode can also be called transverse Alfvén mode or shear Alfvén mode, since the fluid motions for this mode are

entirely transverse with no compressional component [15] and its dispersion relation, for general cases, can be expressed as $\omega/k = V_A cos\theta$ (i.e. $\omega = k_\parallel V_A$ with $k_\parallel$ the parallel wave number), where θ is the angle between wave vector $\mathbf{k}$ and ambient magnetic field $\mathbf{B}$. From the dispersion relations for the slow and fast magneosonic mode [15], i.e. $\omega^2/k^2 = \frac{1}{2}(V_A^2 + V_S^2) + \frac{1}{2}\left[(V_A^2 - V_S^2)^2 + 4V_A^2V_S^2 sin^2\theta\right]^{1/2}$ and $\omega^2/k^2 = \frac{1}{2}(V_A^2 + V_S^2) - \frac{1}{2}\left[(V_A^2 - V_S^2)^2 + 4V_A^2V_S^2 sin^2\theta\right]^{1/2}$ with V_S the velocity/speed of sound waves, both of them involve magnetic field and the plasma pressure. It is for this reason that these two modes are called the magnetosonic modes. It has been well-known that Alfvén waves contribute to a variety of physical processes in space plasmas, e.g.: heating of solar and stellar coronae [16], solar and stellar wind acceleration [17], wave-particle interaction [18], turbulence [19], generation of geomagnetic perturbations (auroral activity) [20], etc. Kinetic Alfvén waves (KAWs) are the extension of (shear) Alfvén waves to the range of short (kinetic) cross-field scales comparable to the ion gyroradius and to the electron inertial length, and thus its dispersion relation is modified as $\omega = k_\parallel V_A \left[1 + \left(1 + \frac{T_e}{T_i}k_\perp^2\rho_i^2\right)\right]$, where T_e,T_i, $k_\perp$ and ρ_i are electron temperature, ion temperature, perpendicular wave number and ion gyroradius, respectively, and ignoring the damping and taking Padé approximation for the Bessel function [21, 22]. KAWs attract researchers not only because they could interact with plasma and their energy can be converted into the energy of electrons and ions (heating, acceleration, and/or transport) [6, 23], but could interact non-linearly with each other and form a power-law turbulent spectrum [24], due to the fact that KAWs can generate parallel electric fields $E_\parallel$ that facilitates particle heating and transport on scales where the ion motion decouples from the field lines due to polarization drift [25]. The local polarization relation of KAWs has also been developed, e.g. as $E_\perp/B_\perp \simeq V_A\left[1 + k_\perp^2\rho_i^2\right] / \left[1 + k_\perp^2\rho_i^2 + k_\perp^2\rho_s^2\right]^{1/2}$ with ρ_s ion acoustic gyroradius [4, 26, 27].

The existence of Alfvén wave resonance in nonuniform ideal MHD plasmas, as well as its potential applications to plasma heating and transport, has been proposed by Grad since the mid-term of last century [28]. In non-uniform plasmas, the Alfvén speed V_A can be expressed as a function of position in the direction of the nonuniformity. For simplicity

but without losing any significance and generality, the description below will reasonably assume the nonuniformity is one-dimensional (1-D) , i.e. only in x direction. The dispersion relation of the shear Alfvén wave is then of the well-known form $\omega = k_{\parallel} V_A$, where $k_{\parallel}$ is the wavenumber parallel to the magnetic field. This is also a resonance condition at x_0, a local point/plane, in space where the excited wave frequency satisfies the relation $\omega_0 = k_{\parallel} V_A(x_0)$. Thus, if a surface wave in MHD theory is excited by an external driver/source, the wave will be phase mixed by this resonance and its wave energy will be dissipated into the surrounding plasmas. Such surface waves can be obtained by setting a large wave number, $k_{\perp}$, which is perpendicular to the ambient magnetic field and the density gradient in x, so that $k_{\perp} V_A > \omega_0$ is achieved for the minimum Alfvén speed. Theoretically, the phase mixing of the waves occurs due to the fact that the shear Alfvén waves have continuous spectra in nonuniform plasmas. The corresponding wave absorption, as well as its energy dissipation, has also been evaluated analytically [29, 26].

1.3 Mode Conversion in Geo-Space

1.3.1 The Structures and Characteristics of the Magnetopause

In history and the contemporary, our human being's exploration of the Earth's geomagnetic topology and environment has never ceased [30, 31, 32]. There is also much occurring in the interplanetary plasma itself from all round our planet; that is, the solar wind. The properties of the solar wind evolve with heliocentric distances, but, generally speaking, on its way to the Earth the solar wind can be regarded as uniform and interacts with the geomagnetic field. This process roughly consists of our planet's geo-magnetic environment, and can be sketchily depicted in two-dimensions (2-D) in Figure 1.1. From this figure, the bow shock, the magnetosphere and the magnetopause, where the pressure balance occurs, can be clearly distinguished. A more detailed three-dimensional (3-D) sketch of the Earth's magnetosphere, representing the structure that has been inferred from spacecraft observations, is given in Figure 1.2.

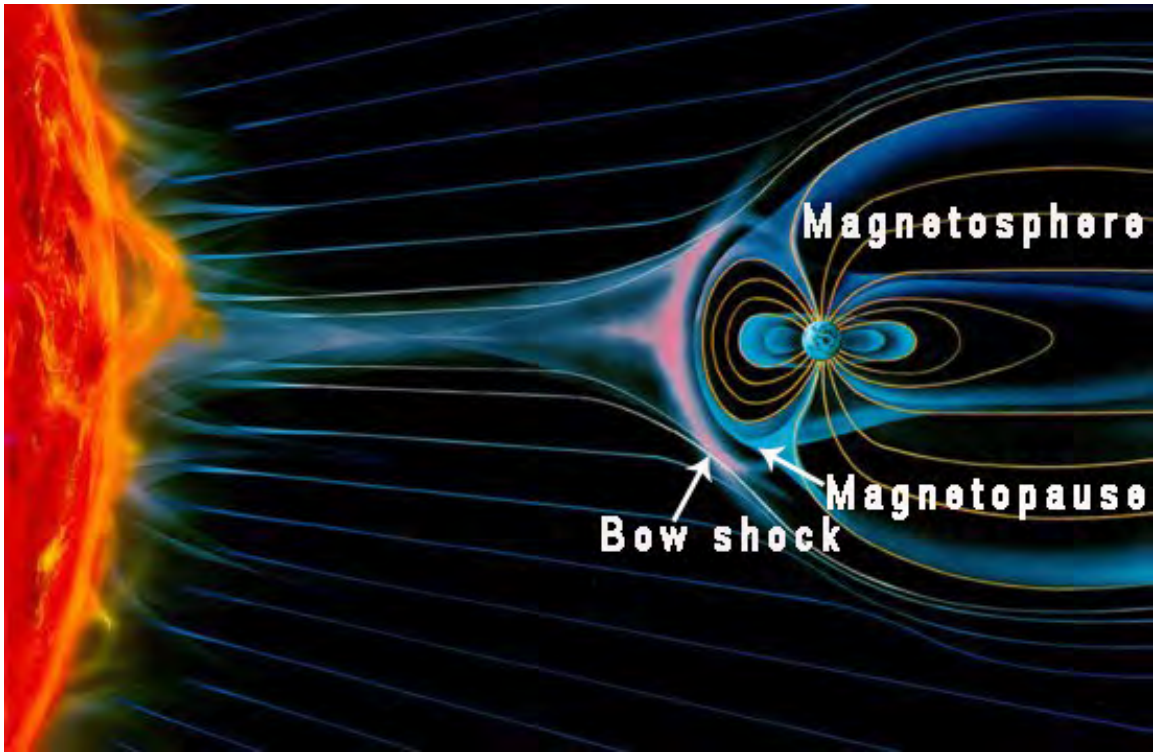

Figure 1.1: 2-D illustration of the interaction between geo-magnetic field and solar wind. Adapted online from http://naturalorder.info/now/

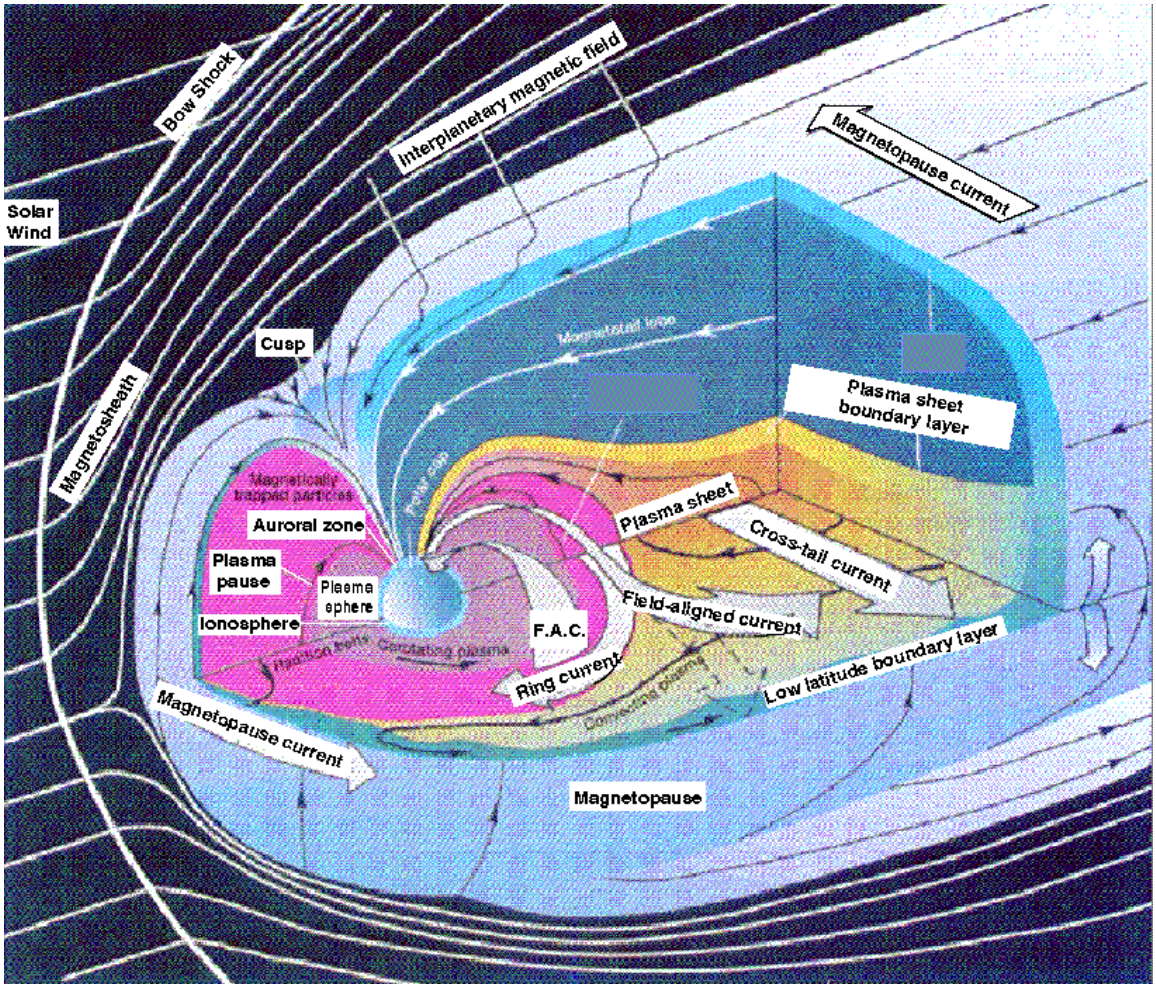

Figure 1.2: 3-D illustration of the Earth's magnetosphere structure and outer magnetic field topology inferred from spacecraft observations. Adapted online from http://www.esa-spaceweather.net/spweather/BACKGROUND/PHYS_PROC/MAGNETOSPHERE/mgsphr.gif

One of the most striking features that had amazed physicists and caused hot debate in geo-space exploration in history is that the collisionless shock even exists [33]. The collision-free bow shock stands in front of the magnetosphere, as shown in Figure 1.1 and 1.2. Early spacecraft observations have shown the dependence of bow shock structure, as well as its upstream region often referenced as foreshock region where the superthermal particles generate a rich spectrum of plasma waves, on solar wind parameters, and have proved that the magnetic profiles of quasi-parallel (Q-$\parallel$) shocks are much broader than quasi-perpendicular (Q-$\perp$) ones. The Q-$\parallel$ is referred to the region where the angle, between the magnetic field in the solar wind and the shock normal, is less than 45°, while the The Q-$\perp$ referred to the angle larger than 45°, shown in Figure 1.3. At the Q-$\parallel$ shock, the downstream thermal ions, as well as the ions reflected at the shock front, can easily backstream along the field lines and penetrate into the upstream region, leading to electromagnetic instabilities associated with ion beams, ion heating, energetic ions and compressional waves [34, 35, 36].

In geo-space plasma physics, it is well known that the Earth's magnetopause boundary layer (MPBL) , which separates the shocked solar wind from the magnetosphere (readers can refer to Figure 1.1, as well as 1.2), plays a central role in various transport processes involving mass, momentum and energy from the solar wind into the magnetosphere. The spacecrafts have detected the MPBL typically several thousands of kilometers thick. Overall, three different types of the MPBL can be recognized: the low-latitude boundary layer (LLBL) , the plasma mantle or alternatively called high-latitude boundary layer (HLBL) , and the high-latitude cusp or called entry layer [2]. Figure 1.4 presents these distinct territories over the MPBL. The characterizations of these boundary layers can be summarized in short here. The LLBL is a region that contains a mix of magnetosheath (the region between the bow shock and the magnetopause) and magnetoshphere plasma, and within which plasma flows can be found in almost any direction, but are generally intermediate between the magnetosheath flow and magnetospheric flows. The high-latitude cusp region is where the magnetic null or cusp occurs in a closed magnetopause model, first proposed by Chapman

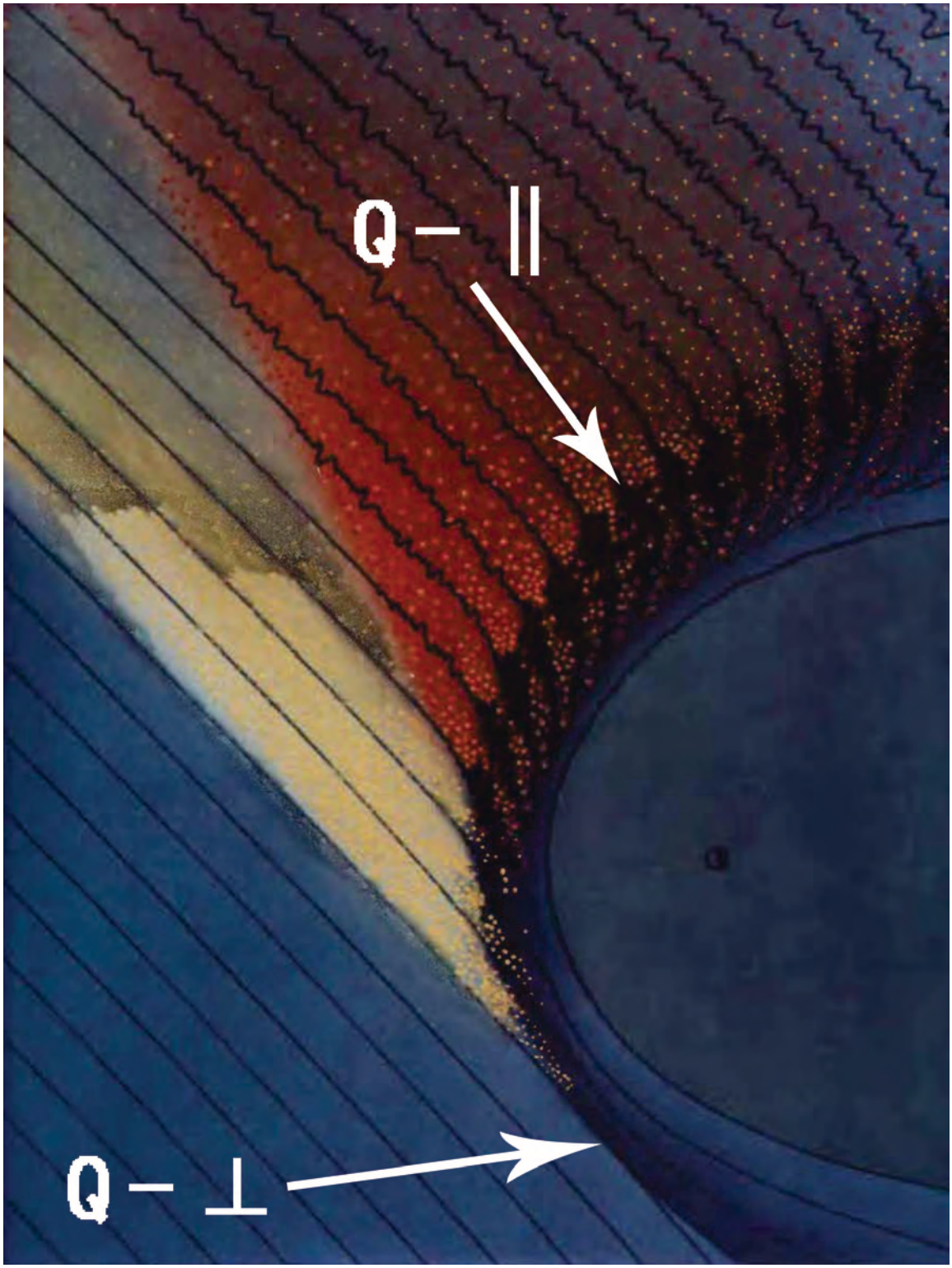

Figure 1.3: A schematic view of the upstream of the earth's bow shock and foreshock region. The IMF lines are at the Parker spiral angle (45°) relative to the sun-earth line. The Photo courtesy of ISEE/Tsurutani and Roriguez, and adapted from [1]

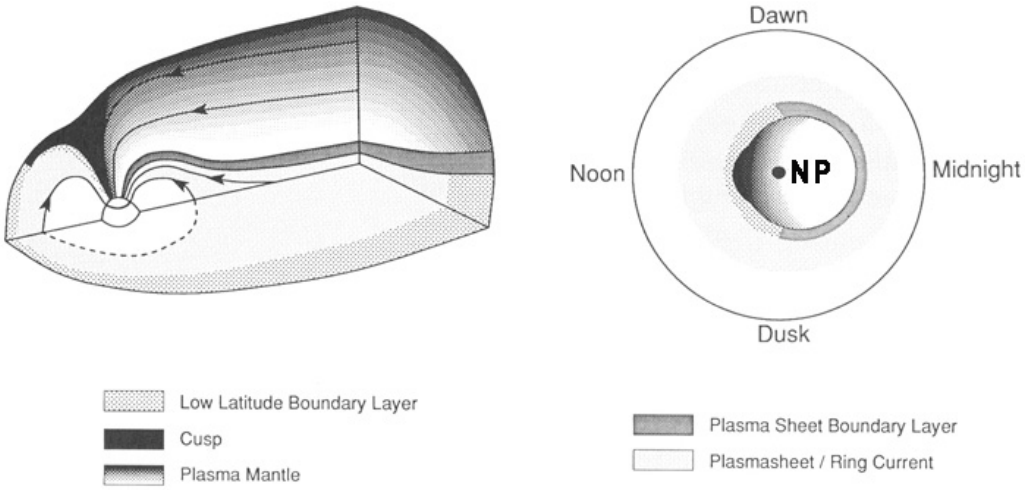

Figure 1.4: Vasyliunas's (1979) mapping of the MPBL down to the high latitude ionosphere. Adapted from Kivelson and Russell [2]

and Ferraro [37, 38]. The plasma in this region is of magnetosheath feature and the flows are low-speed, disordered, and probably turbulent. The last part, the HLBL, is found at higher latitudes tailward of the cusp. Inside the HLBL, plasma flows are always tailward, but the flow speed, density and temperature all decrease away from the magnetopause. The plasma mantle is often regarded as a spatially uniform region, with a gradual transition from magnetosheath to lobe (in magnetotail) propertities. It should be pointed out that the magnetopause's motion compels these boundaries to move back and forth across an in situ spacecraft, giving pulsating signals in the magnetopause region observations.

Satellite observations exploring this frontier also show very fascinating natures of this dynamic boundary layer. Among various transport processes, magnetic reconnection between the interplanetary magnetic field (IMF) lines and the geomagnetic field lines leads to a direct transport through an "open" boundary at the dayside magnetopause [39, 40, 41, 42, 43, 44, 45, 46], when the IMF has a southward ($B_z < 0$) component.

On the other hand, in the cases of a "closed" dayside magnetopause when the IMF has a northward ($B_z > 0$) component, strong evidence of particle cross-field line diffusion and acceleration has been brought forward for considerations [47, 48, 3, 22, 49, 50, 51]. Although with slightly occasional heating cases [52, 53, 54], the energy distribution functions of the plasma around this region substantiated the correctness of the previous mentioned concept that the plasmas consisted of those which sourced from the magnetosheath and the magnetosphere.

Meanwhile, wave-particle interaction has been suggested as an important mechanism for the cross-field lines transport at the low-latitude boundary, where large amplitude ultra-low frequency (ULF) waves are extremely abundant in the geo-observational spectrum [55, 56, 57, 58, 59, 60, 61]. Among these, the KAW deserves a particular concern since it may be one of the most fundamental processes in the deposition of energy into the plasmas near the magnetopause due to linear/nonlinear wave dissipation [4, 62, 63], as I presented to you previously, and will continue to show you more in geo-space physics in the following.

1.3.2 Mode Conversion at the Magnetopause

Since the plasma density changes inversely and sharply with the ambient magnetic field through the MPBL, the Alfvén speed V_A increases dramatically from the magnetosheath to the magnetosphere. This unique feature has led to the suggestion of an interesting ULF wave phenomenon: the mode coupling between the compressional and the Alfvén modes at the location inside the boundary layer where the Alfvén resonance condition $\omega^2 = k_\parallel^2 V_A^2$ is satisfied [26, 64, 65, 66, 67], with ω being the wave frequency and $k_\parallel$ the wave number parallel to the magnetic field. Based on the 1-D linear theory [12, 25], such mode coupling leads to the mode conversion from fast waves to KAWs [6], which can be solved by kinetic models including finite ion Larmor radius effects, as briefly reviewed in Section 1.9. Fast mode compressional waves frequently arise from the turbulent foreshock of quasi-parallel bow shock [36, 68, 69, 70], which in general have $\omega^2 > k_\parallel^2 V_A^2$. The conversion from compressionally

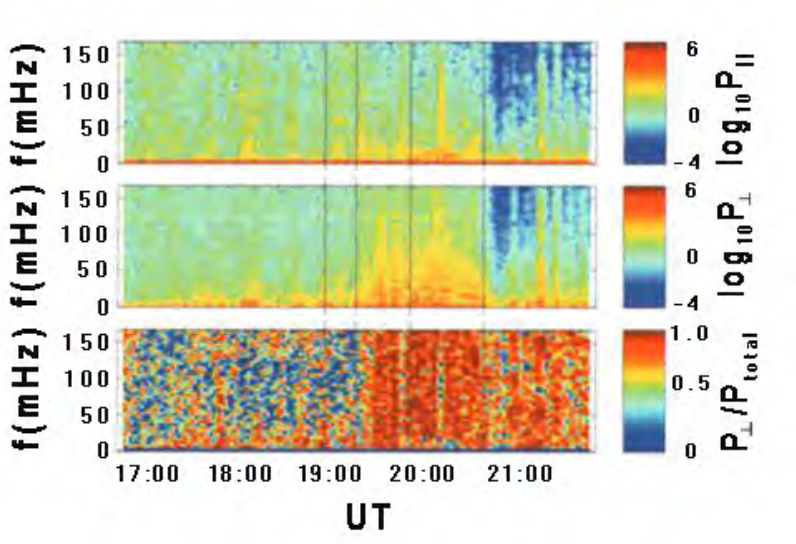

Figure 1.5: Wave power spectra for the "WIND" crossing of the magnetopause. $P_{\parallel}$, $P_{\perp}$ and P_{total} are the wave power spectra densities obtained from $\left|\delta B_{\parallel}\right|^2$, $|\delta B_{\perp}|^2$ and $|\delta \mathbf{B}|^2$, respectively. The change of wave polarization shown in the lower panel coincides with Alfvén velocity gradients encountered upon entry into the magnetopause current layer. Adapted from Johnson et al. [3]

to transversally polarized waves provides a source of kinetic-scale Alfvén waves, and has been suggested a promising mechanism for an effective plasma heating and transport across the MPBL [3, 22, 25, 71, 72, 73].

Changes in the wave polarization, from compressional in the magnetosheath to transverse in the MPBL, have been observed [3] (Figure 1.5), which provides evidence of the mode conversion. Recent multi-point spacecraft measurements of MPBL crossing substantiate the suggestion of the mode conversion process and the presence of KAWs at the magnetopause [4, 62, 74]. Figure 1.6 shows an expanded view of a magnetosphere to magnetosheath transition. The spectrograms in these observations show that the transverse electric and magnetic field components are well correlated with each other, and they match with small-scale KAW dispersion relations. Strong evidence has suggested that these waves with a broadband range in magnetic fluctuations could be characterized by

a Doppler shifted KAW spectrum [4, 75, 76]. Figure 1.7 shows the main results by using the Cluster spacecraft data and wave spectrum analysis [4]. For KAWs with $\omega < \Omega_i$, their dispersion relation is $\omega = k_z V_A \sqrt{1 + k_\perp^2(\rho_s^2 + \rho_i^2)}$, and the E/B ratio can be modeled as $|\delta E_x/\delta B_y| = \frac{V_A(1+k_\perp^2\rho_i^2)}{[1+k_\perp^2(\rho_s^2+\rho_i^2)]^{1/2}} \simeq V_A\sqrt{1+k_\perp^2\rho_i^2}$ if $\rho_i \gg \rho_s$, where $\rho_s = (T_e/m_i)^{1/2}/\Omega_i$, $\rho_i = (T_i/m_i)^{1/2}/\Omega_i$, Ω_i is the ion cyclotron frequency, and T_e and T_i are the electron and ion temperatures, respectively. Observations have also indicated that these KAWs may play a significant role in particle acceleration, heating and transport through Landau damping, transit time damping, as well as transverse ion acceleration via demagnetization or stochastic ion scattering on the ion-cyclotron scale field structures [4, 62, 77, 78]. Moreover, transports of large cross-field electromagnetic energy flux across the MPBL have been observed in these observations, which indicate waves are strong enough to provide an effective particle diffusion coefficient.

Besides the features described above, yet another notable phenomenon of magnetic pulsation structures, so called magnetic field line resonance which is believed to be caused by shear Alfvén waves due to mode conversion process, inside the magnetosphere has to be mentioned [5, 79, 80, 67, 81, 82]. A typical result of harmonically structured pulsations observed by AMPTE (Active Magnetospheric Particle Tracer Explorers) CCE satellite [5] is shown in Figure 1.8. The long-period continuous pulsations can be characterized and brief reviewed as the following [79]: 1. at higher latitude the mostly circularly polarized pulsations reverse their sense of polarization near noon [83], whereas there is no such systematic reversal at lower latitude [84]; 2. polarization reversal also occurs at a different latitude, and the demarcation line coincides with the line of peak wave amplitude and linear polarization [83]; 3. systematic change of the orientation angle in the H-D plane occurs from the second to the first (the first to the second) quadrant near noon in the northern (southern) hemisphere [84]; 4. the frequence independent of latitude for each of the events, but when averaged over many events, the frequency of the peak amplitude is a decreasing function of latitude [85].

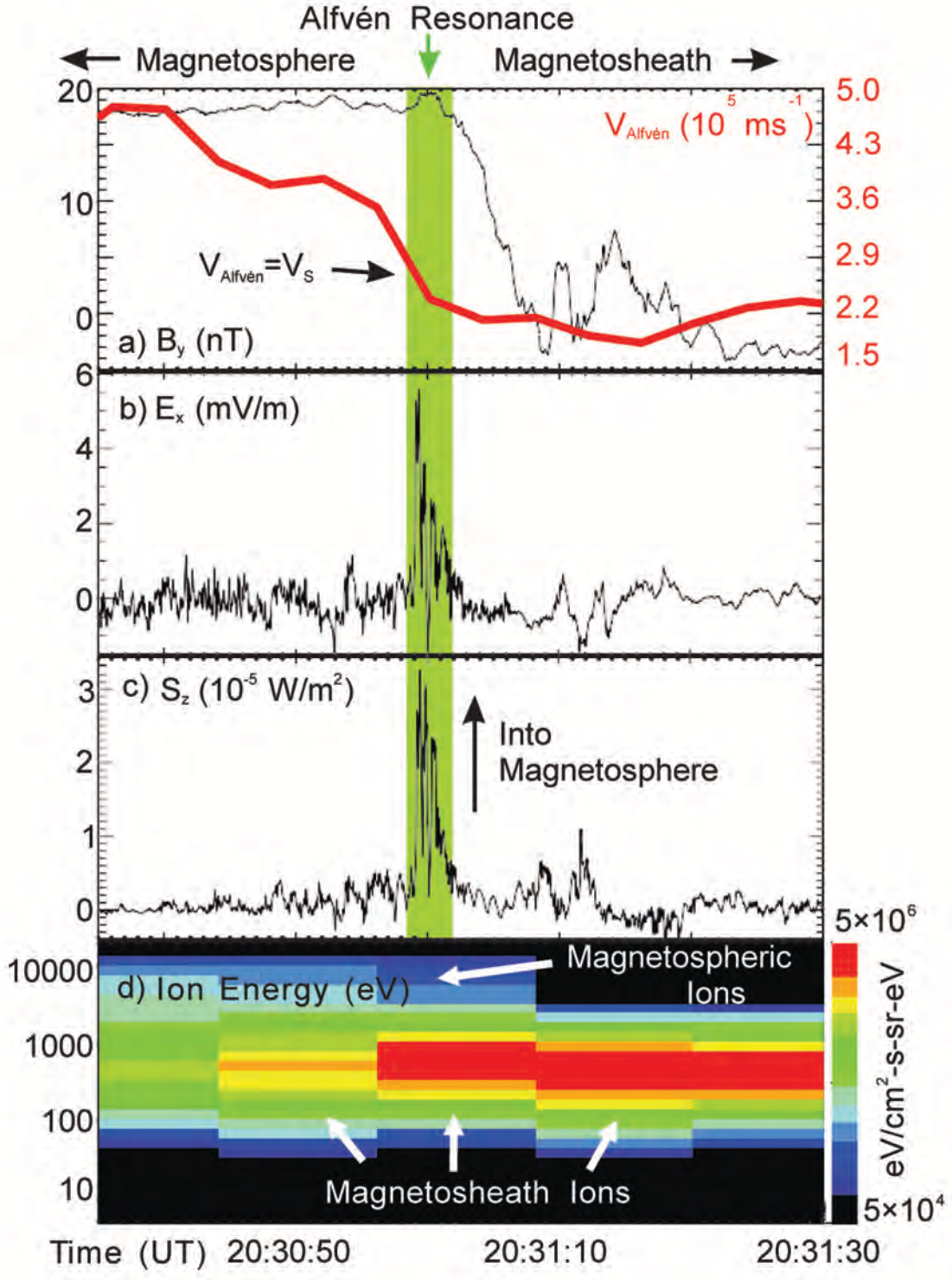

Figure 1.6: (a) Y_{BN}-component magnetic field; the red trace shows the local Alfvén speed. (b) The X_{BN}-component electric field. (c) The wave Poynting flux normal to the magnetopause boundary. (d) Ion energy spectrogram. "BN" is defined in the boundary normal coordinate system where X_{BN} and Y_{BN} lie in the plane of the magnetopause and point closest to the Z_{GSM} and Y_{GSM} directions, respectively. Adapted from Chaston et al. [4]

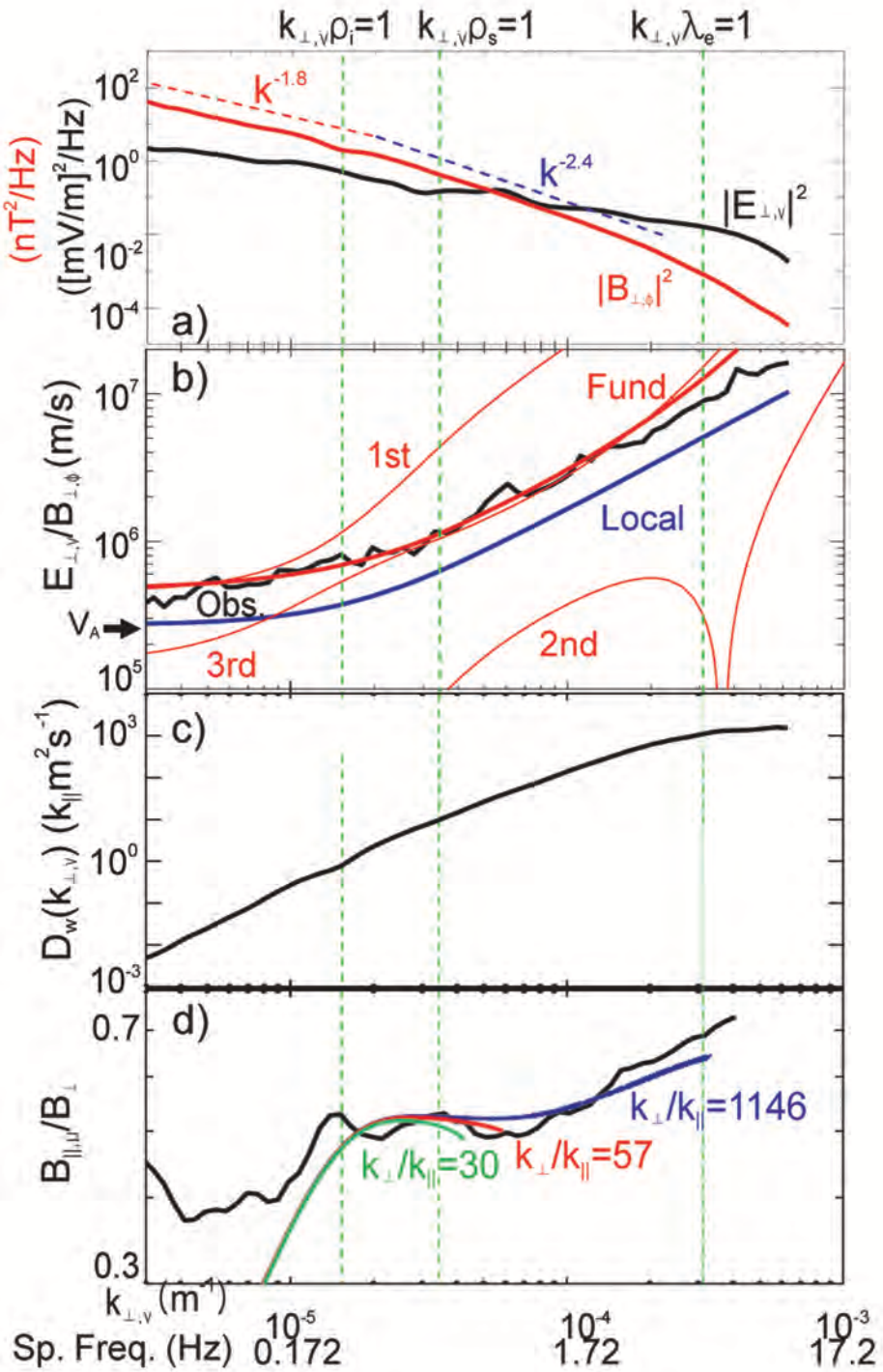

Figure 1.7: (a) Averaged spectral energy density in $E_{\perp,\nu}$ (black) and $B_{\perp,\phi}$ (red). (b) Averaged $E_{\perp,\nu}/B_{\perp,\phi}$ spectra from observations (black), local wave dispersion (blue) and non-local solutions (red) for the fundamental through to third harmonic. (c) Diffusion coefficient at each $k_{\perp,\nu}$. (d) Averaged ratio of compressive to transverse magnetic amplitudes (black) and that given by local wave dispersion for $k_\perp/k_\parallel = 30, 57, 1146$. Adapted from Chaston et al. [4]

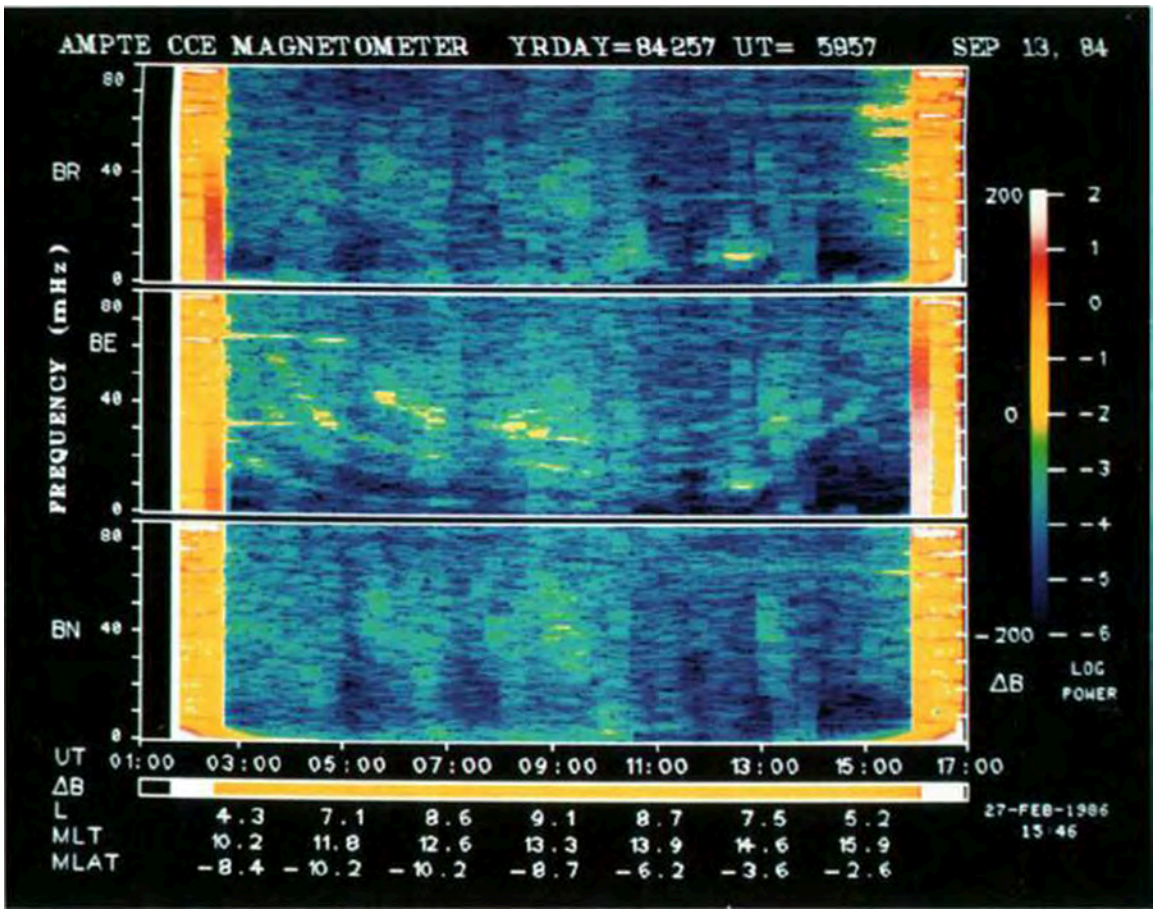

Figure 1.8: Three component dynamic power spectra of AMPTE CCE magnetic field data for a full orbit from 0126 to 1706 UT September 13, 1984. The geomagnetic B_R, B_E and B_N are radially outward from the center of the earth, magnetically eastward and perpendicular to the other two components, respectively. The bottom colored panel represents δB, the difference in field magnitude between the observed total field and the value determined from the IGRF (International Geomagnetic Reference Field) 1980 model. Adapted from Engebretson et al. [5]

1.4 Analytical Model of Mode Conversion

As the title tells, in this section, I will briefly review the theoretical models of mode conversion and the associated wave equations.

1.4.1 MHD Model

In this model, ideal MHD equations can be introduced in the calculations, and for further simplicity of analysis, a so-called 1-D layer/slab model with sheared and straight magnetic field lines could be adopted [12, 26]. Under this configuration, the equilibrium properties of the plasmas, such as mass density ρ_m, pressure P and the ambient magnetic field $\mathbf{B}$, vary in only one direction x. Hence, it is reasonably to assume $\mathbf{B}(\mathbf{x})$ has the form given by

$$\mathbf{B}(x) = B_z(x)\,\mathbf{e}_z + B_y(x)\,\mathbf{e}_y, \tag{1.1}$$

The equilibrium condition gives the relation between magnetic field $\mathbf{B}(x)$ and pressure P by

$$\frac{d}{dx}\left(P + \frac{B^2}{2\mu_0}\right) = 0, \tag{1.2}$$

After linearization of the standard set of MHD equations, taking use of the fluid displacement vector $\boldsymbol{\xi}$, we get the equation of motion for the fluid

$$\mu_0\rho_m\ddot{\boldsymbol{\xi}} = (\mathbf{B}\cdot\nabla)^2\boldsymbol{\xi} - \mathbf{B}(\mathbf{B}\cdot\nabla)(\nabla\cdot\boldsymbol{\xi}) - \mu_0\nabla\tilde{p}, \tag{1.3}$$

where $\tilde{p} = p + \mathbf{b}\cdot\mathbf{B}/\mu_0$, grouped as the total perturbed pressure. Here, $\mathbf{b}$, the total perturbed magnetic field, is related to $\boldsymbol{\xi}$ via Maxwell's equations and given by

$$\mathbf{b} = (\mathbf{B}\cdot\nabla)\boldsymbol{\xi} - \mathbf{B}(\nabla\cdot\boldsymbol{\xi}) - (\boldsymbol{\xi}\cdot\nabla)\mathbf{B}, \tag{1.4}$$

Taking use of the adiabatic equation of state and the continuity equation, the perturbed plasma pressure p can be expressed as

$$p = -\xi_x \frac{d}{dx} P - \gamma P \left(\nabla \cdot \boldsymbol{\xi} \right) = p_1, \tag{1.5}$$

To go further, assume the perturbations have the form

$$\boldsymbol{\xi} = \boldsymbol{\xi} \left(x \right) \exp \left[i \left(k_z z + k_y y - \omega t \right) \right], \tag{1.6}$$

where $\omega = \omega_0 + i\delta$, and $\delta \to 0^+$.

By introducing the local Cartesian coordinates with $\mathbf{e}_\parallel = \mathbf{B}/B$ and $\mathbf{e}_\perp = \mathbf{e}_\parallel \times \mathbf{e}_x$, the component form of Equation (1.3) can be rewritten as

$$\epsilon \xi_\parallel = i k_\parallel \mu_0 \tilde{p} + i B^2 k_\parallel \left(i k_\parallel \xi_\parallel + i k_\perp \xi_\perp + \frac{d\xi_x}{dx} \right), \tag{1.7}$$

$$\epsilon \xi_\perp = i k_\perp \mu_0 \tilde{p}, \tag{1.8}$$

and

$$\epsilon \xi_x = \mu_0 \frac{d\tilde{p}}{dx}, \tag{1.9}$$

where $\epsilon \left(x \right) = \omega^2 \mu_0 \rho_m - k_\parallel^2 B^2$, $k_\parallel \left(x \right) B \left(x \right) = k_z B_z + k_y B_y$, and $k_\perp \left(x \right) B \left(x \right) = k_y B_z - k_z B_y$.

Based on Equations (1.4) and (1.5), the expression of $\xi_\perp \left(x \right)$ can be further rewritten in terms of $\xi_x \left(x \right)$ as

$$\xi_\perp \left(x \right) = \frac{i \alpha k_\perp B^2}{\alpha k_\perp^2 B^2 - \epsilon} \frac{d\xi_x}{dx}, \tag{1.10}$$

where

$$\alpha \left(x \right) = 1 + \frac{\gamma \beta \omega^2}{\omega^2 - \gamma \beta k_\parallel^2 V_A^2}, \tag{1.11}$$

and

$$\beta \left(x \right) = \frac{\mu_0 P}{B^2}, \tag{1.12}$$

To further simplify these equations by means of α and β, one can assume that the ambient plasma is low β, i.e. $\gamma\beta \ll 1$, so $\omega_0^2 \gg \gamma\beta k_\parallel^2 V_A^2$ and $\alpha(x) \simeq 1 + \gamma\beta \sim O(1)$ can be established. Substituting Equations (1.8) and (1.10) into Equation (1.9), one can then finally get the wave equation of ξ_x

$$\frac{d}{dx}\left(\frac{\epsilon\alpha B^2}{\alpha k_\perp^2 B^2 - \epsilon}\frac{d\xi_x}{dx}\right) - \epsilon\xi_x = 0. \tag{1.13}$$

Equation (1.13) contains the shear Alfvén, the magnetosonic/compressive, and the ion acoustic waves. In the context of nonuniform plasmas, all three waves are coupled. Equation (1.13) deserves to bear particular attention that it has a singular solution at the resonance point $x = x_0$ where $\epsilon = 0$. It is this singularity that leads to the wave phase mixing, and the energy of the excited waves is dissipated thereafter. The dissipated energy goes to other waves, i.e. so called mode conversion process, with a continuous spectrum as in the case of Landau damping. Mathematically, the process is reversible with an infinitely long recurrence time. In reality, the small Ohmic or viscous dissipation could destroy the reversibility and the dissipated energy will be converted into thermal energy [26].

1.4.2 Kinetic Multi-fluid Model

In Section 1.4.1, a simple 1-D MHD model has been presented and we see that the Alfvén resonance point is located at the singular point where $\epsilon = 0$. However, the ion finite larmor radius effects provide a finite parallel electric field, a perpendicular velocity that modifies the $\mathbf{E} \times \mathbf{B}$ drift, and a gyro-viscosity tensor (to the momentum equations), but all of these are neglected in such one-fluid MHD models. In order to study these kinetic effects on MHD phenomena, especially in the cases where core plasma kinetic effects, such as KAWs, it is important to modify the MHD model so that it properly addresses the relevant core plasma kinetic effects [21].

For a brief review, a plasma model with multiple ion species is considered, and a general kinetic multi-fluid model which eliminates temporal scales with frequency higher than the ion cyclotron frequency. Since the ambient magnetic field can be perturbed by orders of magnitude in the magnetosphere, it is naturally necessary for a global model to be valid at the ion cyclotron frequency of each ion species, as well as in the MHD regime. A typical example is the case in which ion cyclotron waves generated in the central plasma sheet by ion temperature anisotropy frequently associated with ground-based observations. The magnetic field varies several orders of magnitude between the central plasma sheet and the ionosphere, and must be sufficiently general to include ion cyclotron resonances. The kinetic-multi-fluid model consists of a set of fluid equations which are closed by the solutions of kinetic equations for each species. The fluid equations consist of continuity equations and momentum equations for each particle species and will be closed provided the particle pressure tensors are obtained from solutions of the Vlasov equation. The particle kinetic physics is incorporated through plasma pressure tensors. Because of small electron mass, the electron momentum equation can be replaced by Ohm's law and the electron density determined by the charge quasi-neutrality condition. In this form, the model is sufficiently general to describe global structures with frequency up to the ion gyro-frequency. Thus, it is appropriate for studying ion-cyclotron waves and other low-frequency phenomena.

For each particle species the density continuity equation and momentum equation can be given by

$$\frac{\partial n_j}{\partial t} + \nabla \cdot (n_j \mathbf{V}_j) = 0, \tag{1.14}$$

and

$$n_j m_j \left(\frac{\partial}{\partial t} + \mathbf{V}_j \cdot \nabla \right) \mathbf{V}_j = n_j q_j \left(\mathbf{E} + \mathbf{V} \times \mathbf{B} \right) - \nabla \cdot \mathbf{P}_j, \tag{1.15}$$

where q_j is the particle charge, m_j is the particle mass, the pressure tensor for each species is defined in its moving frame by

$$\mathbf{P}_j = m_j \int (\mathbf{v} - \mathbf{V}_j)(\mathbf{v} - \mathbf{V}_j) f_j d^3v, \tag{1.16}$$

here f_j is the particle distribution function for species j.

A generalized Ohm's law that relates the current to the electric field is obtained by multiplying (1.15) by q_j/m_j and by summing over all particle species by ignoring $O(m_e/m_i)$ and thus given by

$$\frac{m_e}{n_e e^2}\left[\frac{\partial \mathbf{J}}{\partial t} + \nabla\cdot(\mathbf{JV} + \mathbf{VJ})\right] + \eta\mathbf{J} = \mathbf{E} + \frac{1}{n_e}\left(\sum_i n_i q_i \mathbf{V}_i - \mathbf{J}\right)\times\mathbf{B} + \frac{1}{n_e}\nabla\cdot\left(\mathbf{P}_e^{cm} - \sum_i \frac{q_i m_e}{e m_i}\mathbf{P}_i^{cm}\right), \tag{1.17}$$

where the summation over i is for all ion species, $e = |q_e|$, the center-of-mass pressure tensor for each species is defined relative to the bulk flow velocity $\mathbf{V}$ by

$$\mathbf{P}_j^{cm} = m_j \int (\mathbf{v} - \mathbf{V}_j)(\mathbf{v} - \mathbf{V}_j) f_j d^3v, \tag{1.18}$$

here $\mathbf{P}_j^{cm} = \mathbf{P}_j + n_j m_j (\mathbf{V} - \mathbf{V}_j)(\mathbf{V} - \mathbf{V}_j)$, and the plasma resistivity (η) is added to mimic collisional effects. In deriving the generalized Ohm's law, one can take use of the charge-neutrality condition, $n_e e = \sum_i n_i q_i$, which is equivalent to the condition $\nabla\cdot\mathbf{J} = 0$. Note that for a single ion species, the generalized Ohm's law reduces to the well-known one-fluid form with $\mathbf{V}_i = \mathbf{V}(1 + O(m_e/m_i))$. For multiple ion species, however, the generalized Ohm's law relates the electric field to the density and fluid velocity of all ion species. This complication arises because the diamagnetic and polarization drift velocities are different for each ion species. The one-fluid mass density and momentum can thus not be used to couple with the generalized Ohm's law.

Therefore, one can employ the density and momentum equations for each ion species. The electron momentum equation is replaced by the generalized Ohm's law. The electric and

magnetic fields are related to the plasma current and are obtained form Maxwell's equations in the magneto-static limit: the Faraday's law

$$\frac{\partial \mathbf{B}}{\partial t} = -\nabla \times \mathbf{E}, \tag{1.19}$$

here $\mathbf{E}$ is the electric field; and the Ampere's law becomes

$$\nabla \times \mathbf{B} = \mathbf{J}, \tag{1.20}$$

with the neglection of displacement currents; meanwhile we still have

$$\nabla \cdot \mathbf{B} = 0, \tag{1.21}$$

To close the above multi-fluid equations, one needs to specify the pressure tensor for each particle species. There are several ways to achieve this, such as prescribing a fluid description for ions and electrons, or otherwise computing the pressure tensor from the particle distribution functions [21].

Finally, for demonstration purpose, by making use of multi-fluid theory [21, 86], and expressing the linearized equations in terms of $\delta p_1 = B_0 \delta B_\parallel + \delta p$ and $\delta B_\perp$ [87], the equation holding the singularity then becomes

$$\left[\omega^2 \left(1 - \lambda_e^2 \nabla_\perp^2\right) - k_\parallel^2 V_A^2 \left(1 - \rho_s^2 \nabla_\perp^2\right)\right] B_0 \delta B_\perp = i k_\parallel V_A^2 \nabla_\perp \delta p_1, \tag{1.22}$$

where the electron inertial effects $\lambda_e = c/\omega_{pe}$ and electron pressure effects on the ion acoustic Larmor radius scale $\rho_s^2 = T_e/m_i\Omega_i^2$ are both included in this equation. It is obvious that the ratio of electron pressure to electron inertial effects, ρ_s/λ_e, determines their relative importance; the electron pressure effects are dominant if $\rho_s/\lambda_e = (4\pi n T_e/B^2)\sqrt{m_i/m_e} > 1$, which is the case when $\beta_e/2 > \sqrt{m_e/m_i} \simeq 0.02$.

1.4.3 Kinetic Model

Ultimately, it is the ion kinetic effects that remove the singularity in Equation (1.13), which is derived from ideal MHD equations as previously shown in Section 1.4.1. As before, only 1-D slab geometry model is presented here. Let the x-axis be the direction of the nonuniformity, and z-axis the direction of the unperturbed ambient magnetic field B_0. Then the plasma displacement vector, $\boldsymbol{\xi}$, is of only 1-D component form $\xi_x = \xi_x(x)\exp[i(k_y y + k_z z - \omega t)]$, and Equation (1.13) under such configuration can be rewritten as

$$\frac{d}{dx}\left(\frac{\epsilon\alpha B_0^2}{\alpha k_y^2 B_0^2 - \epsilon}\frac{d\xi_x}{dx}\right) - \epsilon\xi_x = 0, \tag{1.23}$$

where $\beta(x) = \mu_0 P/B^2$. ϵ and α are related to the ambient plasmas, given by

$$\epsilon(x) = \omega^2 m_i n_0 \mu_0 - k_z^2 B_0^2 = B_0^2\left(\frac{\omega^2}{V_A^2} - k_z^2\right), \tag{1.24}$$

and

$$\alpha(x) = 1 + \frac{1}{2}\left(\gamma\beta\omega^2\right)\left[\omega^2 - \frac{1}{2}\gamma\beta k_z^2 V_A^2\right]^{-1}, \tag{1.25}$$

The notations here are of conventional meanings, such as the ion mass m_i, the background plasma number density n_0, the space permeability μ_0, the ratio of the specific heats γ, the pressure ratio of the plasma to the magnetic field β, and the Alfvén speed V_A.

As stated before, if we assume that the wave frequency ω and the parallel wave number k_z are constant and fixed by the external sources, $\epsilon(x)$ could be equal to zero at a certain location x_0 which is the so called Alfvén resonance point/location. At the location x_0, the local Alfvén waves would resonate with the applied external frequency. The solution of the wave equation (1.23) near the resonance point x_0 has the form

$$\begin{aligned} \xi_x &= c\ln(x - x_0), && x > x_0, \\ &= c\left(\ln|x - x_0| + i\pi\right), && x > x_0, \end{aligned} \tag{1.26}$$

The imaginary part in Equation (1.26) appears via the theoretical solutions in the different domains $x > x_0$ and $x < x_0$, and denotes the resonant absorption of the external perturbations in the ambient plasma. The absorption rate could be evaluated up to almost a hundred percent if k_y is chosen to be one over the scale size of the plasma nonuniformity

$$\kappa = \frac{\partial \ln n_0}{\partial x}. \tag{1.27}$$

The logarithmic singularity exists owing to the fact that the ideal MHD equations do not allow propagations of the shear Alfvén waves across the magnetic field. Consequently, it is a natural expectation that if a finite ion Larmor radius correction is introduced, the fact that ions can no longer be frozen into a particular magnetic field line of force will enable their propagations across the magnetic field and thus resolve the singularity. That is, the solution of Equation (1.26) is invalid within the range $|x - x_0| \lesssim \rho_i$, where ρ_i is the ion gyroradius. The finite electron inertia effects can also contribute in the same way and eliminates the singularity in the range $|x - x_0| \lesssim \rho_s$, where $\rho_s = \rho_i \left(T_e/T_i\right)^{1/2}$, and T_e and T_i are electron and ion temperatures, respectively. In order to include these effects, one has to take use of kinetic equations. For the demonstration and simplicity here, I will only present the mode conversion process; that is, any dissipative effects will not be included. The Vlasov equation for ions and the drift kinetic equation for electrons are adopted in such an analytical context.

The linearized Vlasov equation for the perturbed distribution function of ions can be expressed as

$$\frac{\partial f_i}{\partial t} + \mathbf{v} \cdot \frac{\partial f_i}{\partial \mathbf{x}} + \frac{e}{m_i} \left(\mathbf{E} + \mathbf{v} \times \mathbf{B}\right) \cdot \frac{\partial f_i^{(0)}}{\partial \mathbf{v}} + \frac{e}{m_i} \left(\mathbf{v} \times \mathbf{B}_0\right) \cdot \frac{\partial f_i}{\partial \mathbf{v}} = 0, \tag{1.28}$$

where

$$\frac{\partial \mathbf{B}}{\partial t} = -\nabla \times \mathbf{E}, \tag{1.29}$$

and $\mathbf{E}$ has the meaning of the electric field of the waves.

According to the literature [6], the unperturbed distribution function can be rewritten as

$$f_i^{(0)} = g\left(x + v_y/\omega_{ci}\right) f^{(0)}\left(\mathbf{v}\right), \tag{1.30}$$

where $f^{(0)}\left(\mathbf{v}\right)$ is the Maxwellian distribution function with the ion temperature T_i, and g is another function denoting the nonuniformity in the ambient plasma, which in this case is in x direction.

Similarly, the linearized Vlasov equation for the perturbed distribution function of electrons, yielding to the drift kinetic equation, is given by

$$\frac{\partial f_e}{\partial t} + v_z \frac{\partial f_e}{\partial z} + \left(\frac{E_y}{B_0} + v_z \frac{B_x}{B_0}\right) \frac{\partial f_e^{(0)}}{\partial x} - \frac{e}{m_e} E_z \frac{\partial f_e^{(0)}}{\partial v_z} = 0, \tag{1.31}$$

If assuming the plasma is of low-β as before, then one can easily achieve the point that the magnetic compression by the wave is negligible, and thus can take use of the scalar potential φ in the calculation of the electric field to describe the perpendicular components in $\mathbf{E}$, i.e.

$$\mathbf{E}_\perp = -\nabla_\perp \varphi, \tag{1.32}$$

Here, I want to remind our readers that this is a rational and powerful approximation in many analytical works, such as the newly developed GeFi model [88].

One of the advantages for Equation (1.32) is that we have the relation $\left(\nabla \times \mathbf{E}\right)_z = 0$. Since the waves introduced here are electromagnetic, a non-zero component $\mathbf{E}_z$ (i.e. $\mathbf{E}_\parallel$) must be identified not as $-\partial\varphi/\partial z$. For consistency, another potential, ψ, could be exploited [89], given by

$$E_z = -\frac{\partial \psi}{\partial z}, \tag{1.33}$$

with $\psi \neq \varphi$. Certainly the potentials ψ and φ must meet the requirements of the appropriate field equations. From literatures [6, 89], the Poisson's equation has the following form

$$\nabla_{\perp}^{2}\varphi + \frac{\partial^{2}\psi}{\partial z^{2}} = \frac{e}{\epsilon_{0}}\left(n_{e} - n_{i}\right), \tag{1.34}$$

and the Ampére's law has the form

$$\left(\nabla \times \mathbf{H}\right)_{z} = J_{iz} + J_{ez}, \tag{1.35}$$

Substitute Faraday's Law, Equation (1.29), into Poisson's equation, and taking use of Equation (1.35), then Equation (1.34) can be simplified as

$$\frac{\partial}{\partial z}\nabla_{\perp}^{2}\left(\varphi - \psi\right) = \mu_{0}\frac{\partial}{\partial t}\left(J_{iz} + J_{ez}\right), \tag{1.36}$$

In the equations above, the ion number density n_i, the electron number density n_e, the ion current density J_i, and the electron current density J_e could be calculated from the distribution function f_j with subscript j being the species for ions or electrons

$$n_{j} = n_{0}\int f_{j}d\mathbf{v}, \tag{1.37}$$

and

$$\mathbf{J}_{j} = q_{j}n_{0}\int \mathbf{v}f_{j}dv, \tag{1.38}$$

Up till now, the whole set of Equations from (1.28) to (1.38) characterizes the electromagnetic waves in the MHD wave frequency range with no restrictions on the wavelength of perpendicular scale, but with the restriction only on absence of compressive magnetic field perturbations.

By making some assumptions, one can go further to simplify this set of equations and find the beauty of the mode conversion of the Alfvén waves at the Alfvén resonance point from kinetic theory.

The first assumption is that the frequency range is below the ion cyclotron frequency. This is in favor of using the quasi-neutrality approximation and the Poisson's Equation (1.34) can be reduced to the simple form

$$n_i = n_e, \tag{1.34'}$$

The second assumption is that the wavenumber, k_y, perpendicular both to the ambient magnetic field and to the nonuniformity direction, is much less than ρ_i^{-1}, and that the nonuniformity scale is much greater than the ion Larmor radius, so one can get the relation

$$\frac{\omega}{\omega_{ci}} \gg k_y \kappa \rho_i^2, \tag{1.39}$$

This relation could be used to simplify the second variable v_y/ω_{ci} in nonuniformity function g in Equation (1.30), which means that drift waves are neglected.

The last assumption to be made is that the wavelength in the nonuniformity direction x near the Alfvén resonance point of the mode conversion is small enough but still larger than the ion Larmor radius. This allows one to follow the previous work [90] to expand the wave equation in the power series of $\rho_i d/dx$.

By taking all these assumptions, the Fourier transformation of the equations containing the amplitude of the number density and the current density perturbations can be attained, after tedious calculations, as follows

$$\frac{en_i}{\epsilon_0} = \frac{\omega_{pi}^2}{\omega_{ci}^2}\left[\frac{d}{dx}\left(1 + \frac{3}{4}\rho_i^2\frac{d^2}{dx^2}\right)\left(g\frac{d\varphi}{dx}\right) - gk_y^2\varphi\right] + \frac{\omega_{pi}^2}{\omega^2}k_z^2 g\psi, \tag{1.40}$$

$$\frac{en_e}{\epsilon_0} = \frac{\omega_{pe}^2}{v_{Te}^2}g\psi, \tag{1.41}$$

$$\mu_0 J_{iz} = \frac{\omega_{pi}^2}{c^2}\frac{k_z}{\omega} g\psi, \tag{1.42}$$

and

$$\mu_0 J_{ez} = -\frac{\omega_{pe}^2}{c^2 v_{Te}^2}\frac{\omega}{k_z} g\psi, \tag{1.43}$$

Note that in these equations, the ion and electron plasma frequency, ω_{pi} and ω_{pe}, can be regarded as constants and expressed by the values at the maximum plasma density where $g(x)$ is normalized to unity. c and v_{Te} represent the speed of light and the electron thermal speed, respectively.

To see the behavior of mode conversion to the KAWs at the Alfvén resonance point, $x = x_0$ where $\omega^2 = k_z^2 V_A^2 / [g(x = x_0)]$, one can only take the regions near the resonance point into account. Then these equations can be simplified further in a low-β plasma, given the fact that $V_A^2 \gg c_s^2 = T_e/m_i$ in low-β plasmas. It is noted that one can remove the possibility of a mode coupling to the ion acoustic waves by taking use of this assumption. One can then also be able to derive the wave equation by substituting ψ from Equations (1.34′), (1.36), from (1.40) to (1.43)

$$\left(\frac{\omega^2}{k_z^2 V_A^2}\frac{3}{4}\rho_i^2\frac{d^3}{dx^3} + \frac{d^2}{dx^2}\frac{1}{g}\frac{T_e}{T_i}\rho_i^2\frac{d}{dx}\right)\left(g\frac{d\varphi}{dx}\right) + \left[\frac{d}{dx}\left(\frac{\omega^2}{k_z^2 V_A^2}g - 1\right)\frac{d}{dx} - k_y^2\left(\frac{\omega^2}{k_z^2 V_A^2} - 1\right)\right]\varphi = 0, \tag{1.44}$$

where the Alfvén speed V_A is the value at the maximum density, and g is the unitary normalized nonuniformity function.

From Equation (1.44), if one takes use of the limit $\rho_i \to 0$, this wave equation can be reduced greatly to

$$\frac{d}{dx}\left[\epsilon(x)\frac{d\varphi}{dx}\right] - k_y^2\epsilon(x)\varphi = 0, \tag{1.45}$$

This reduced equation is equivalent to Equation (1.13) derived from MHD theory near $\epsilon = 0$ (Alfvén resonance point).

Besides, if one proceeds in a uniform background plasma, i.e. $g = 1$, Equation (1.44) can be decoupled into two wave equations

$$\nabla_{\perp}^{2}\varphi = 0, \tag{1.46}$$

and

$$\left[\bar{\rho}^{2}\frac{d^{2}}{dx^{2}} + \left(\frac{\omega^{2}}{k_{z}^{2}V_{A}^{2}} - 1\right)\right]\varphi = 0, \tag{1.47}$$

where $\bar{\rho}^{2} = \left(\frac{3}{4} + T_{e}/T_{i}\right)\rho_{i}^{2}$, and $k_{y} \ll d/dx$ condition is used in the derivation of Equation (1.47).

Equation (1.46) describes a quasi-static electromagnetic wave mode (cut-off mode) in the presence of an external source. In the circumstances that there is no external sources, such a wave equation denotes a surface wave. Equation (1.47) represents the wave equation for a bulk or body wave. Specifically, it is the desired Alfvén wave with finite ion Larmor radius and finite electron inertia correction. It is this wave that is often referred to as the KAW [6, 7].

Therefore, one can distinguish the wave coupling from Equation (1.45) between a surface MHD mode, or externally driven electromagnetic perturbations, and the KAW. From Equation (1.47), it can be seen that after the mode conversion process occurs, the KAWs propagate to the higher density side where $k_{z}^{2}V_{A}^{2}(x) < k_{z}^{2}V_{A}^{2}(x = x_{0})$, as analogous to the case of the Bernstein wave [91].

To go further in the demonstration of the mode conversion, the nonuniform density profile must be given. Since after the mode conversion the waves are expected to propagate into the higher density side, the solution depends on whether or not the converted waves can propagate all the way across the plasma column or dissipate significantly before they reach the other side.

As an illustrative example studied by Hasegawa and Chen [6], a simple linear profile of the plasma density is assumed as

$$g\left(x\right) = \kappa x + a, \tag{1.48}$$

where x is a normalized distance, and its origin is located at the Alfvén resonance point where $g\left(x=0\right)\omega^2/k_z^2V_A^2 = 1$, or $a\omega^2/k_z^2V_A^2 = 1$, with $0 < a < 1$. Equation (1.44) then can be simplified near $x \sim 0$ to the form

$$\rho^2\left(\frac{d^2E_x}{dx^2}\right) + \kappa x E_x = E_0, \tag{1.49}$$

where

$$\rho^2 = \left(\frac{3}{4} + \frac{k_z^2V_A^2}{\omega^2}\frac{T_e}{T_i}\right)\rho_i^2, \tag{1.50}$$

and

$$E_x = -\frac{\partial\varphi}{\partial x}, \tag{1.51}$$

In Equation (1.49), E_0 is a integration constant denoting a value of E_x at a large negative x. Note that E_x is also associated with the external source field.

In this derivation, another assumption should be made: $|dg/dx/g| \ll |d\varphi/dx/\varphi|$; it means that the amplitude of the waves varies much faster than that of the densities (i.e. WKB approximation). The wave equation of the type of Equation (1.49) has been studied broadly associated with the mode conversion of the electromagnetic waves to Langmuir waves, and it is well-known that its solution can be expanded by Airy functions [92].

For completeness, the pursuit of the solutions for Equation (1.49) will be restated briefly in the following [6], and then I will move on to present the linear damping of the KAWs.

First a scale length is defined as

$$\Delta = \left(\rho^2/\kappa\right)^{1/3}, \tag{1.52}$$

and a normalized electric field intensity is given as

$$\bar{E}_x = -\frac{E_x}{E_0}\frac{(\rho\kappa)^{2/3}}{\pi}, \tag{1.53}$$

the general solution is given by

$$\bar{E}_x = c_1 A_i\left(-x/\Delta\right) + c_2 B_i\left(-x/\Delta\right) + G_i\left(-x/\Delta\right), \tag{1.54}$$

where A_i and B_i are Airy functions, and G_i is a function related to the integrals of A_i and B_i.

The plasma we are considering is in the semi-finite domain in $x > 0$. Thus, to the $x > 0$ direction, the appropriate boundary conditions for the KAWs would be the right (positive x direction) going waves with no reflections at $x \to \infty$. The asymptotic solution for $|x/\Delta| \gg 1$ can be achieved as, for $x > 0$,

$$E_x = -\frac{\pi^{1/2} E_0}{(\kappa\rho)^{2/3}}\left(\frac{\Delta}{x}\right)^{1/4} \exp\left\{i\left[\frac{2}{3}\left(\frac{x}{\Delta}\right)^{3/2} + \frac{\pi}{4}\right]\right\} + \frac{E_0}{\kappa x}, \tag{1.55}$$

and for $x < 0$ can be attained as

$$E_x = \frac{E_0}{\kappa x}, \tag{1.55$'$}$$

The first term on the r.h.s. in Equation (1.55) denotes the KAWs. The second term on the r.h.s. in Equation (1.55) and the term on the r.h.s. in Equation (1.55$'$) represent the source field.

The KAWs propagate to the higher density region $x \geq 0$ of the resonance point, as shown in Equation (1.54). The qualitative property of the mode converted KAWs is presented in Figure 1.9.

It is noted that the solution for $x < 0$ part is equivalent to the previous one attained with the ideal MHD theory. Consequently, the plasma impedance, and thus the absorption rate, seen from the external circuit remains unchanged from the MHD calculations [6, 26].

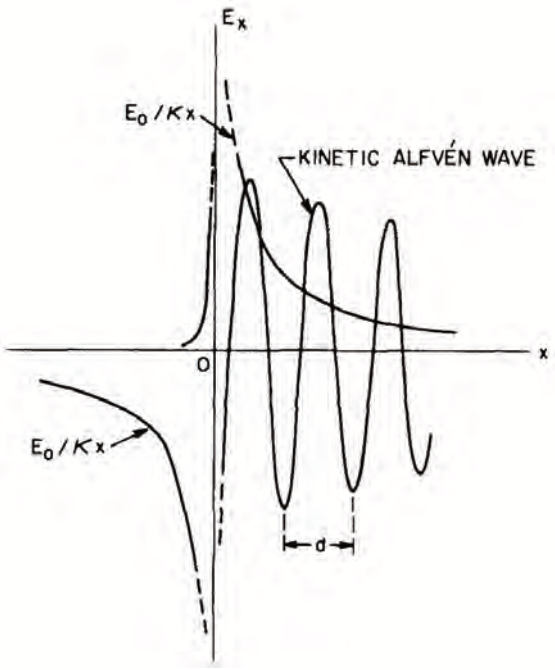

Figure 1.9: Schematic diagram of the x-component of the wave electric field near the spatial resonance point ($x = 0$). $x > 0$ region corresponds to the higher density side where the KAWs are excited. Also note that plasma heating process happens when the KAWs are dissipated by wave-particle interactions. Adapted from Hasegawa and Chen [6]

When the converted KAWs, however, is reflected to the plasma side, the solution at $x < 0$ is modified from MHD result and accordingly so does the the external plasma impedance.

Now let's turn to the meat part of this subsection, the linear damping of the KAWs. With no restrictions/approximations on the size of the perpendicular wavelength, it is also convenient to show the detailed behavior of KAWs [6]. An additional Fokker-Plank collision term on the r.h.s. of the Vlasov equation has to be added and after a long arithmetic manipulation, one can attain a new set of equations including the number density and the current density perturbations

$$\frac{en_i}{\epsilon_0} = -\frac{\omega_{pi}^2}{v_{Ti}^2}\left[1 - I_0\left(\lambda_i\right)e^{-\lambda_i}\right]\varphi + \frac{\omega_{pi}^2 k_z^2}{\omega^2} I_0\left(\lambda_i\right)e^{-\lambda_i}\left(1 - i\delta_i\right)\psi \\ -i\frac{\omega_{pi}^2}{v_{Ti}^2}\frac{\nu_{ii}}{\omega}\varphi\left\{\begin{array}{ll} \frac{7}{10}\lambda_i^2 & \lambda_i \ll 1 \\ \frac{3(\pi+1)}{8\sqrt{\pi}}\lambda_i^{1/2} & \lambda_i \gg 1 \end{array}\right\}, \tag{1.40′}$$

$$\frac{en_e}{\epsilon_0} = \frac{\omega_{pi}^2}{v_{Te}^2}\left(1 + i\delta_e\right)\psi, \tag{1.41′}$$

$$\mu_0 J_{iz} = \frac{\omega_{pi}^2}{c^2}\frac{k_z}{\omega} I_0\left(\lambda_i\right)e^{-\lambda_i}\left(1 - i\delta_i\right)\psi, \tag{1.42′}$$

$$\mu_0 J_{ez} = -\frac{\omega_{pe}^2}{c^2 v_{Te}^2}\frac{\omega}{k_z}\left(1 + i\delta_e\right)\psi, \tag{1.43′}$$

where $\lambda_i = k_x^2\rho_i^2$, $I_0\left(\lambda_i\right)$ is the modified Bessel function of the first kind, and ν_{ii} is the ion-to-ion collision frequency. δ_i and δ_e denote the damping rates for ions and electrons, respectively. Specifically, in the collisional regime δ_e is expressed as

$$\delta_e = \omega\nu_{ei}/\left(k_z v_{Te}\right)^2, \tag{1.56}$$

where ν_{ei} is the electron ion collision rate. By contrast, in the collisionless regime,

$$\delta_i = 2\sqrt{\pi}\beta_i^{-3/2}\exp\left(-\beta_i^{-1}\right), \tag{1.57}$$

$$\delta_e = \sqrt{\pi}\beta_i^{-1/2}\left(T_i/T_e\right)^{1/2}\left(m_e/m_i\right)^{1/2}, \tag{1.58}$$

here β_i is defined as the ion pressure.

Hasegawa and Chen [6] studied the mode converted structures and derived the corresponding dispersion relation by taking use of the Equations (1.40′) to (1.43′). For demonstration and future reference in later sections, the procedure will be reproduced briefly.

Starting from the quasi-neutrality condition, the following equation can be obtained,

$$\left(\frac{\omega_{pi}^2 k_z^2}{\omega^2} I_0 e^{-\lambda_i} - \frac{\omega_{pe}^2}{v_{Te}^2}\right)\psi - \frac{\omega_{pi}^2}{v_{Ti}^2}\left(1 - I_0 e^{-\lambda_i}\right)\varphi = 0, \tag{1.59}$$

and the Ampére's becomes

$$\left(\frac{\omega_{pi}^2}{c^2 k_x^2} I_0 e^{-\lambda_i} - \frac{\omega_{pe}^2}{c^2 k_x^2}\frac{\omega^2}{k_z^2 v_{Te}^2} + 1\right)\psi - \varphi = 0, \tag{1.60}$$

Note that in these equations and below, the argument of the modified Bessel function has been changed to $\lambda_i\,(= k_x^2\rho_i^2)$. The dispersion relation can be achieved by eliminating ψ and φ,

$$\left(I_0 e^{-\lambda_i} - \frac{\omega^2}{k_z^2 c_s^2}\right)\left[1 - \frac{\omega^2}{k_z^2 V_A^2}\frac{1}{\lambda_i}\left(1 - I_0 e^{-\lambda_i}\right)\right] = \frac{\omega^2}{k_z^2 v_{Ti}^2}\left(1 - I_0 e^{-\lambda_i}\right), \tag{1.61}$$

where c_s is the ion acoustic speed. Equation (1.61) clearly shows the linear coupling of the Alfvén wave with the ion acoustic wave. In low-β plasmas, this coupling is weak and it is possible to decouple these waves for each mode. The dispersion relation for the Alfvén mode (KAW mode) is given by

$$\frac{\omega^2}{k_z^2 V_A^2} = \frac{\lambda_i}{1 - I_0 e^{-\lambda_i}} + \frac{T_e}{T_i}\lambda_i, \tag{1.62}$$

and for the ion acoustic mode by

$$\frac{\omega^2}{k_z^2 c_s^2} = \frac{I_0 e^{-\lambda_i}}{1 + \left(1 - I_0 e^{-\lambda_i}\right)\frac{T_e}{T_i}}, \tag{1.63}$$

Note that the finite ion Larmor radius effect comes into the Alfvén waves positively and into the ion acoustic waves negatively. Thus, the dispersion relations for small and large λ_i, for the KAWs, become

$$\omega^2 = \begin{cases} k_z^2 V_A^2 \left[1 + k_x^2 \rho_i^2 \left(\frac{3}{4} + \frac{T_e}{T_i}\right)\right] & \lambda_i \ll 1, \\ k_z^2 V_A^2 k_x^2 \rho_i^2 \left(1 + \frac{T_e}{T_i}\right) & \lambda_i \gg 1, \end{cases} \tag{1.62$'$}$$

and the ion acoustic waves after this correction become

$$\omega^2 = \begin{cases} \frac{k_z^2 c_s^2 \left(1 - k_x^2 \rho_i^2\right)}{1 + k_x^2 \rho_i^2 (T_e/T_i)} & \lambda_i \ll 1, \\ \frac{k_z^2 c_s^2 / \sqrt{2\pi} k_x \rho_i}{1 + (T_e/T_i)} & \lambda_i \gg 1, \end{cases} \tag{1.63$'$}$$

Taking full use of these expressions, one can finally get the phase and amplitude relations among different components of the wave fields. The results for the KAWs are listed below

$$\begin{cases} E_x = -ik_x\varphi, \\ E_y = -ik_y\varphi, \\ E_z = ik_z \left(\frac{T_e}{T_i}\right) \left(1 - I_0 e^{-\lambda_i} \varphi\right), \\ B_x = i \frac{k_y k_z \varphi}{\omega} \left[1 + \frac{T_e}{T_i} \left(1 - I_0 e^{-\lambda_i}\right)\right], \\ B_y = -i \left(\frac{k_x k_z \varphi}{\omega}\right) \left[1 + \frac{T_e}{T_i} \left(1 - I_0 e^{-\lambda_i}\right)\right], \end{cases} \tag{1.64}$$

Since $k_x \sim \rho_i^{-1} \gg k_y \gg k_z$, from this set of equations (1.64), we can conclude that the dominant field perturbations are E_x and B_y. Note that this is a useful conclusion of mode conversion process near the subsolar region at the Earth's magnetopause. It should also be noted that these waves accompany an electric field in the direction of the ambient magnetic field, i.e. $E_\parallel$.

1.5 Previous Hybrid Simulations of Mode Conversion at the Magnetopause

Hybrid simulations in 2-D and 3-D have been carried out by [87, 7] for mode conversion at the magnetopause in slab geometries under a steady-state, monotonic fast-mode driver. These simulations, which solve the fully kinetic ion physics in a self-consistent electromagnetic field, illustrate how the incoming compressional fast-mode waves are mode converted to short wavelength KAWs ($k_\perp \rho_i \sim 1$) at the Alfvén resonant surface. These work show that the behaviors of mode conversion depends on wave frequency, wave vector, Alfvén speed profile, ion β_i in the magnetosheath, electron-to-ion temperature ratio, and the incident wave amplitude. Moreover, the 3-D simulation shows the excitation of KAWs with the perpendicular and azimuthal wave vector component due to the nonlinear physics, which is crucial for large transport across the boundary [7]. Specifically, KAWs with a large azimuthal wave number $k_y \rho_i \sim 1$ that is perpendicular to both the background magnetic field and the wave vector of the incident compressive waves are nonlinearly excited in the mode conversion process; i.e. strong wave perturbations with finite wavelength along y (i.e. azimuthal) are aroused while k_y mode are not seen in the incident fast-mode waves. Figure 1.10 shows a spectral analysis of the power of B_x in the k_y-$k_\parallel$ plane for the wave structures when mode conversion occurs. Unlike 2-D results, 3-D simulations clearly show the presence of wave powers at large $k_y \sim 1$ with harmonics of $k_\parallel$, as well as the harmonics of the nonlinearly excited $k_y \sim 1$ modes. In addition, strong ion heating in the resulting KAWs, cascaded from mode converted compressional waves at the Alfvén velocity gradient, is also found in these simulations. It has been also pointed out that the coupling of KAWs to the large scale convectively turbulent plasmas may be of great importance in the coupling between the ionosphere and magnetosphere [93], in the heating of the solar wind and corona [94], and in the suppression of the turbulent transport in laboratoy plasmas [95].

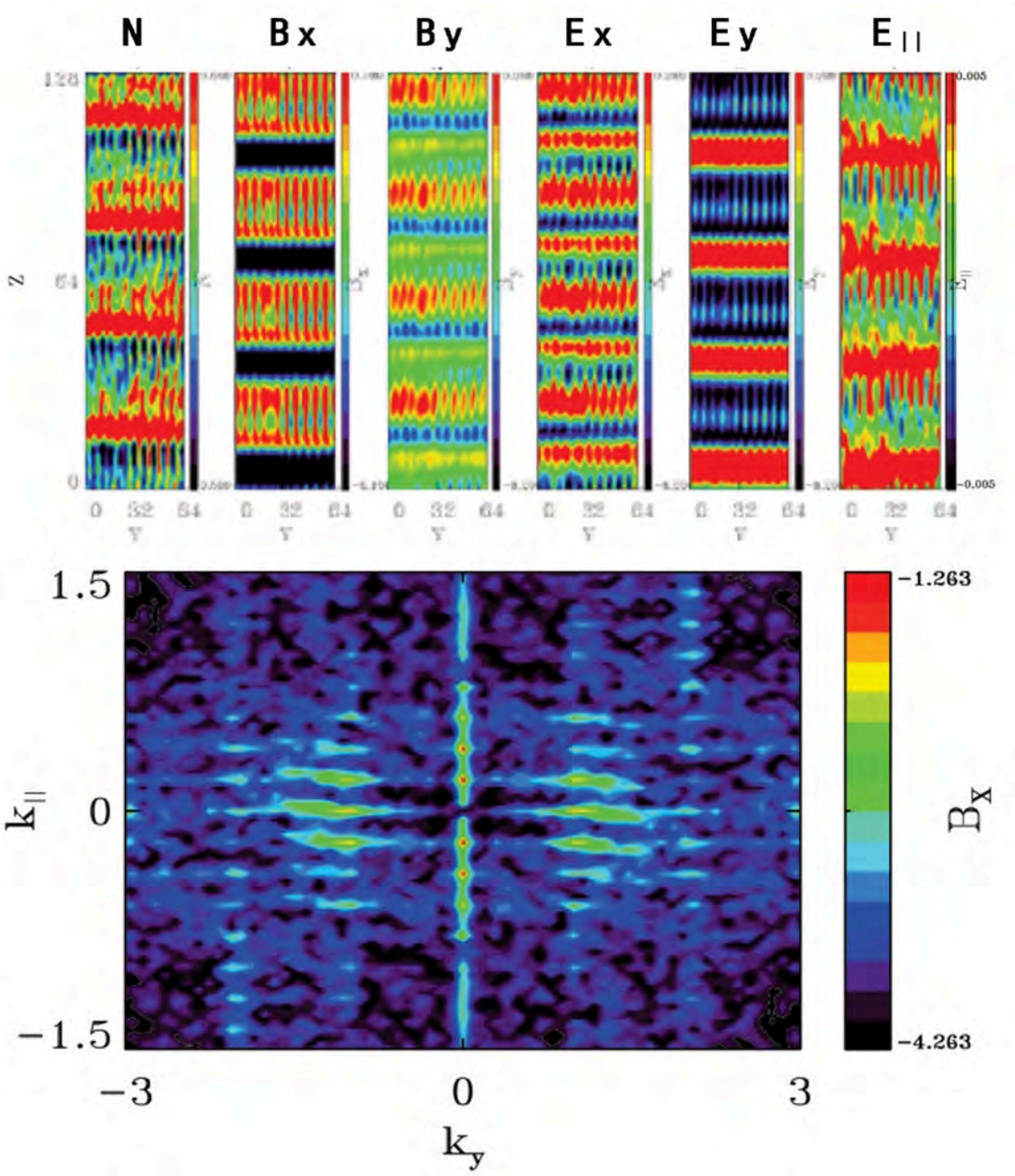

Figure 1.10: Top panel: Contours of various quantities in the y-z plane at the Alfvén resonance point, showing the excited k_y mode from the 3-D simulation of mode conversion. Bottom panel: k_y-$k_{\|}$ spectra of B_x structures in the top panel of 3-D simulations. Adapted from Lin et al. [7]

1.6 Objectives and Outline of the Dissertation

Those simulations [87, 7] described in Section 1.5, however, are based on an over-simplified configuration of the MPBL. In the global magnetosphere, the foreshock waves interact with the magnetopause in the form of wave pulses with finite spatial extent and time duration, while the mode conversion as predicted by theories occurs in a highly localized region around the Alfvén resonance points. In reality, the transient foreshock wave forms, the global nonuniformity, and the presence of the background flow convection change the characteristics of the plasmas around the magnetopause radically, and hence must be included and considered to understand the mode conversion and the evolution of the resulting KAWs. Based on these considerations, it is essentially necessary to perform realistic global-scale hybird simulations of mode conversion at the dayside magnetopause, in order to understand the physics of transport in the magnetosphere and explain spacecraft observations in geo-space. This is where my Dissertation comes from. For such purpose, the simulation is conducted for cases with a northward IMF ($B_z \geq 0$) to exclude the reconnection at the magnetopause, and singles out the transport at the "closed" magnetosphere.

The outline of this Dissertation is stated as follows. The simulation model is described in Chapter 2. The simulation results are presented in Chapter 3. The mode conversion is studied by tracking the evolution of wave structures from the magnetosheath to the magnetopause, and the structure of KAWs is around the magnetopause. How the IMF conditions control the mode conversion process is studied in Chapter 4. A concluding summary is given in Chapter 5.

Chapter 2

3-D Global-Scale Hybrid Simulation Model

2.1 Simulation Scheme

The dayside global-scale hybrid simulation model utilized in this study was first developed by Swift [8] and then extended to 3-D simulations of the dayside magnetosphere by Lin and Wang [36] in 2005. In this hybrid model, ions are treated as fully kinetic particles, except for the inner most magnetoshpere region of $r < 7R_e$, and the electrons are treated as a purely massless fluid. That two fluids approximation is adopted to dominate the evolutions of inner magnetosphere stems from the fact that the fluid plasma in inner region hardly affects the kinetics in the region around the magnetopause.

The ion motions are described by their equation of motion, in the simulation unit,

$$\frac{d\mathbf{v}_i}{dt} = \mathbf{E} + \mathbf{v}_i \times \mathbf{B} - \nu(\mathbf{V}_i - \mathbf{V}_e), \tag{2.1}$$

where $\mathbf{v}_i$ is the ion particle velocity, $\mathbf{E}$ is the electric filed, $\mathbf{B}$ is the magnetic field, ν is the collision frequency, or say the resistivity, and $\mathbf{V}_i$ and $\mathbf{V}_e$ are the bulk flow velocities of ions and electrons, respectively.

The electric field is obtained from the momentum equation of the electron fluid

$$\mathbf{E} = -\mathbf{V}_e \times \mathbf{B} - \nu(\mathbf{V}_e - \mathbf{U}_i) - r\frac{d\mathbf{V}_e}{dt} - \nabla P_e/N, \tag{2.2}$$

where r is electron-to-ion mass ration, P_e is the thermal pressure of the electrons, and N is the electron density, or the ion number density based on the assumption of quasi-charge neutrality which is obtained by calculating the zero moment of ions in the particle discrete

phase space. The collisional frequency ν, equivalent to resistivity, is set to be nearly zero around the MPBL regions so that the parallel electric field is mainly determined by the electron pressure gradient [36].

The total ion bulk flow velocity $\mathbf{U}_i$ in Equation (2.2) can be estimated from

$$\mathbf{U}_i = \frac{N_i}{N}\mathbf{V}_i + \frac{N_f}{N}\mathbf{V}_f, \tag{2.3}$$

where N_i is particle ion density, and N_f fluid ion density. $\mathbf{V}_f$ has obviously the meaning of fluid ion bulk flow velocity.

The Ampére's law is used to evaluate the electron bulk flow velocity

$$\mathbf{V}_e = \mathbf{U}_i - \frac{\nabla \times \mathbf{B}}{\alpha N}, \tag{2.4}$$

where in our simulation the value $\alpha = (4\pi e^2/m_i c^2)$. I shall discuss this parameter in next subsection later.

In our simulation, the fluid ion density is presumed so that we do not have to bother the transport of ion density. The viability of this approximation has been proved reasonably and effectively enough in the inner magnetosphere-ionosphere global system [8, 36]. But the solution of transport equation of fluid ion velocity is indeed required since the ionospheric plasma plays an important role in the conduction of field-aligned currents and the transmission of Alfvén waves in inner boundary/magnetosphere region. The fluid ion equation of motion is estimated from

$$\frac{d\mathbf{V}_f}{dt} = \mathbf{E} + \mathbf{V}_i \times \mathbf{B} - \nu(\mathbf{V}_f - \mathbf{V}_e), \tag{2.5}$$

Here, we dropped the pressure term, and this is a rational assumption especially in the context of the cold and comparatively dense ionosphere plasma. Given the fact that the term $\mathbf{V}_f \cdot \nabla \mathbf{V}_f$ is small, the total time derivative in Equation (2.5) can be reduced to partial

time derivative $\partial \mathbf{V}_f/\partial t$. By far, we are able to see the point that the set of Equations (2.1), (2.2), and (2.5) is momentum conserving.

For the convenience in coding, taking use of Equations (2.2), (2.3), and (2.4), we can rewrite and group terms in a time stepping algorithm. Note that this means the magnetic field $\mathbf{B}$ is presumably known, and its updated algorithm will be given soon. We then get the form

$$\frac{d\mathbf{v}_i}{dt} = \left(\frac{\nabla \times \mathbf{B}}{\alpha N} - \mathbf{U}_i\right) \times \mathbf{B} + \nu \frac{N_f}{N} \left(\mathbf{V}_f - \mathbf{V}_i\right) + \mathbf{v}_i \times \mathbf{B}, \tag{2.6}$$

Likewise, Equation (2.5) for the fluid ion could be transformed to

$$\frac{\partial \mathbf{V}_f}{\partial t} = -\mathbf{V}_f \cdot \nabla \mathbf{V}_f + \left(\frac{\nabla \times \mathbf{B}}{\alpha N}\right) \times \mathbf{B} - \frac{N_p}{N} \left(\mathbf{V}_i - \mathbf{V}_f\right) \times \mathbf{B} + \nu \frac{N_p}{N} \left(\mathbf{V}_i - \mathbf{V}_f\right), \tag{2.7}$$

Now, we can safely turn to the update of magnetic field with Faraday's law

$$\frac{\partial \mathbf{B}}{\partial t} = -\nabla \times \mathbf{E}, \tag{2.8}$$

By taking use of Equation (2.2), it can be rewritten as

$$\frac{\partial \mathbf{B}}{\partial t} = -\nabla \times \left[\left(\frac{\nabla \times \mathbf{B}}{\alpha N} - \mathbf{U}_i\right) \times \mathbf{B}\right] - \nabla \times \left(\nu \frac{\nabla \times \mathbf{B}}{\alpha N}\right), \tag{2.9}$$

The first term $\nabla \times \mathbf{B}/\alpha N$ on the r.h.s. represents the propagation of whistler mode in the limit that the propagation frequency is much less than the gyro-frequency. The second term containing $\mathbf{U}_i$ on the r.h.s. corresponds the propagation of Alfvén modes. The last term on the r.h.s. has the meaning of diffusion so could smooth out noisy fluctuations in the magnetic field. Note that the significant role the eletron inertia plays is to incur electron polarization drift term and thus the Equation (2.9) can be modified by Ampére's law (2.4)

to the form

$$\frac{\partial}{\partial t}\left[\mathbf{B}+r\nabla\times\left(\frac{\nabla\times\mathbf{B}}{\alpha N}-\mathbf{U}_i\right)\right]=r\nabla\times(\mathbf{V}_e\cdot\nabla\mathbf{V}_e)-\nabla\times\left[\left(\frac{\nabla\times\mathbf{B}}{\alpha N}-\mathbf{U}_i\right)\times\mathbf{B}\right]-\nabla\times\left(\nu\frac{\nabla\times\mathbf{B}}{\alpha N}\right), \tag{2.10}$$

It is obvious that the correction is only of the order of the electron-to-ion mass ratio. Besides, Equation (2.10) can be further grouped and rewritten, for the computational convenience, as

$$\frac{\partial}{\partial t}\mathbf{B}'=-r\nabla\times[\mathbf{V}_e\times(\nabla\times\mathbf{V}_e)]-\nabla\times\left[\left(\frac{\nabla\times\mathbf{B}}{\alpha N}-\mathbf{U}_i\right)\times\mathbf{B}+\nu\frac{\nabla\times\mathbf{B}}{\alpha N}\right], \tag{2.11}$$

where

$$\mathbf{B}=\mathbf{B}'-r\nabla\times\left(\frac{\nabla\times\mathbf{B}}{\alpha N}-\mathbf{U}_i\right), \tag{2.12}$$

from these, $\mathbf{B}$ can be solved and updated by iteration.

One more point that has to be mentioned is in our simulations, to maintain as accurate as possilbe in the computation of $\nabla\times\mathbf{B}$, stemming from small differencing errors, the magnetic field is splitted into two portions

$$\mathbf{B}=\mathbf{B}_0+\mathbf{B}_1. \tag{2.13}$$

where $\mathbf{B}_0$ corresponds to curl-free part, and $\mathbf{B}_1$ denotes the variable part which is to be updated only.

As for the time-stepping algorithm, the velocities are known at half time steps, and the positions and fields are advanced at even time steps. In this Dissertation, the leapfrog technique is employed for the subcycling update of the magnetic field. Interpolation has been used for the update of both fields and particles. Second-order accuracy has been achieved in the discretization.

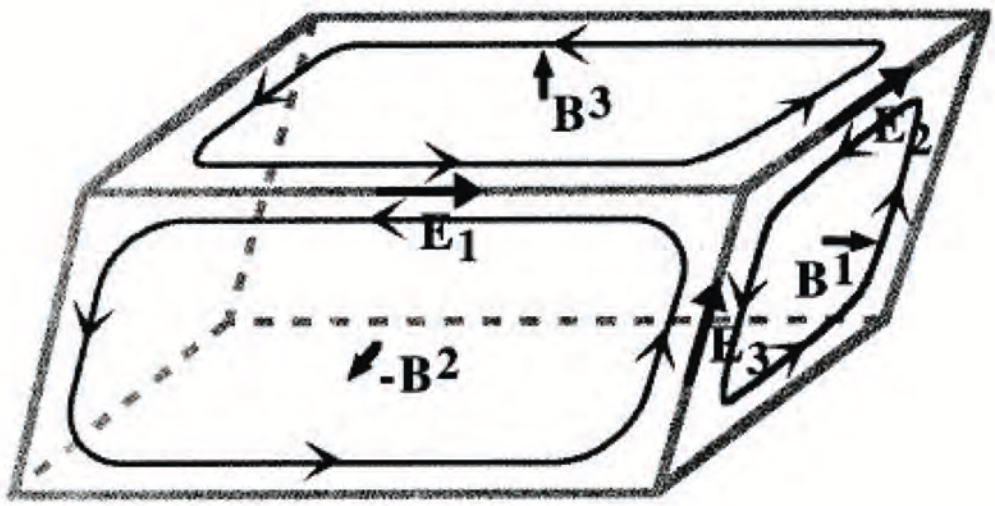

Figure 2.1: A typical curvilinear coordinate cell showing the components of the magnetic and electric fields. Adapted from [8]

2.2 Curvilinear Coordinates

This section describes the use of the curvilinear coordinates. The corresponding Cartesian positions of the curvilinear grid points can be calculated through a table of geometrical coeffcients. Figure 2.1 shows a typical curvilinear coordinate cell, of which the center is at the grid point i, j, k, while the corner point is at $i+\frac{1}{2}$, $j+\frac{1}{2}$, $k+\frac{1}{2}$ and $i+\frac{1}{2}$, $j+\frac{1}{2}$, $k-\frac{1}{2}$, etc. Correspondingly, a dual cell is defined as a cell with centers at the half grid points and corners at the whole grid points, i, j, k. The magnetic field components are shown as vectors on cell faces with the components pointing normal to the faces while the electric field resides on the cell edges. The magnetic field components can be presented by taking the scalar product of $\mathbf{B}$ with the unit vector normal to the cell surfaces. In another word, the magnetic field can be presented in contraviant components

$$\mathbf{B} = \mathbf{l}_1\hat{B}^1 + \mathbf{l}_2\hat{B}^2 + \mathbf{l}_3\hat{B}^3, \tag{2.14}$$

where $\mathbf{l}_1$, $\mathbf{l}_2$,and $\mathbf{l}_3$ are tangent vectors, while $\hat{B}^1$, $\hat{B}^2$ and $\hat{B}^3$ are contravarient tensor components. Note that a set of reciprocal basis vectors ω's can also be defined so that the magnetic field can be expressed as

$$\mathbf{B} = \boldsymbol{\omega}_1 \hat{B}^1 + \boldsymbol{\omega}_2 \hat{B}^2 + \boldsymbol{\omega}_3 \hat{B}^3, \tag{2.15}$$

where $\boldsymbol{\omega}^i \cdot \mathbf{l}_j = \delta^i_j$. For instance, applying this to the right-facing face of the parallelepiped cell, which is centered at $(i + \frac{1}{2}, j, k)$, the discretization of Farady's law gives

$$\begin{aligned}\left[\frac{(\hat{B}^1)^{n+1} - (\hat{B}^1)^n}{\Delta t} \cdot \frac{\mathbf{l}_1}{l_1} \cdot \mathbf{A}^1\right]_{i+\frac{1}{2},j,k} &= \left(\hat{E}^{n+\frac{1}{2}} \cdot \mathbf{l}_3\right)_{i+\frac{1}{2},j-\frac{1}{2},k} - \left(\hat{E}^{n+\frac{1}{2}} \cdot \mathbf{l}_3\right)_{i+\frac{1}{2},j+\frac{1}{2},k} \\ &+ \left(\hat{E}^{n+\frac{1}{2}} \cdot \mathbf{l}_2\right)_{i+\frac{1}{2},j,k+\frac{1}{2}} - \left(\hat{E}^{n+\frac{1}{2}} \cdot \mathbf{l}_2\right)_{i+\frac{1}{2},j,k-\frac{1}{2}},\end{aligned} \tag{2.16}$$

where $l_{2,3}$ are the lengths of the cell edges and reside at the center of the edges. $\mathbf{A}^1 = \mathbf{l}_2 \times \mathbf{l}_3$ is the area of the corresponding cell surface and l_1 is the corresponding dual cell tangent vector.

The length of tangent vectors ($\mathbf{l}$'s) are the difference between coordinates specified in the coefficient table as mentioned previously

$$(\mathbf{l}_2)_{i+\frac{1}{2},j,k+\frac{1}{2}} = (\mathbf{r})_{i+\frac{1}{2},j+\frac{1}{2},k+\frac{1}{2}} - (\mathbf{r})_{i+\frac{1}{2},j-\frac{1}{2},k+\frac{1}{2}}, \tag{2.17}$$

where the $\mathbf{r}$'s are the position of the coordinate points.

The particle position is updated from

$$\left(q^i\right)^{n+1} = \left(q^i\right)^n + \Delta t \mathbf{M}^i \cdot \mathbf{v}^{n+\frac{1}{2}}, \tag{2.18}$$

where the vector tensor $\mathbf{M}^i$ convert $\mathbf{v}$ into particle position q^i in a contravariant form. Note that the positions of particles are also position-dependent and thus they are interpolated from the grid to the particle position using bilinear weighting in 3-D.

2.3 Simulation Setups

In the previous section, we have mentioned that $\alpha = (4\pi e^2/m_i c^2)$ in Equation (2.4), so that $(\alpha N)^{-1/2}$ is the ion inertial length. In our simulation, α is always coupled with the density, and vice versa. Therefore, the value of α scales the density in our simulation and controlled by the ion inertial length.

For the presentation and completeness here, the physical quantities are normalized as follows. The magnetic field $\mathbf{B}$ is scaled by the IMF $\mathbf{B}_0$; the ion number density N by the solar wind density N_0; the time t by the inverse of the solar wind ion gyrofrequency, Ω_{i0}^{-1}; the plasma flow velocity $\mathbf{V}$ by the solar wind Alfvén speed V_{A0}; the temperature by V_{A0}^2; and the length by the Earth radius R_E.

Spherical coordinates are adopted in our 3-D simulation, and the same as previous ones [36, 96, 97]. The simulation domain contains the system of the bow shock, magnetosheath, and magnetosphere in the dayside region with GSM $x > 0$ and a geocentric distance $4R_E \leq r \leq 22R_E$. The Earth is located at the origin $(x, y, z) = (0, 0, 0)$. Outflow boundary conditions are utilized at $x = 0$, while inflow boundary conditions of the solar wind are applied at $r = 22R_E$. The inner boundary at $r = 4R_E$ is assumed to be perfectly conducting, and an additional cold ion fluid is used to model the inner magnetosphere at $r < 7R_E$.

As stated in the previous chapter, to exclude the possibility of reconnection in "open" magnetopause cases, the IMFs setup in the simulation are all without southward components. A radial IMF is assumed for the case shown in Chapter 3, whereas northward IMF components are set in Chapter 4. The ion inertial length in the solar wind is chosen as $d_{i0} = 0.1R_E$. A uniform solar wind plasma with ion beta value $\beta_i = 0.5$ and Alfvén Mach number $M_A = 5$ is employed, which flows into the system along the $-x$ direction with an isotropic drifting Maxwellian distribution. A total of about 4×10^8 particles are used, and the number density of the macro ion-particles is set to be $N_0 = 11,000R_E^{-3}$ in the solar wind. An isothermal electron equation of state is assumed, with $\beta_e = 2.0$ to ensure a temperature ratio $T_e/T_i \simeq 0.1$ - 0.2 at the magnetopause.

Nonuniform grid spacing is used in the radial direction, with a higher resolution of $\Delta r = 0.05R_E$ around the magnetopause in order to identify the small scale KAWs, while $\Delta r = 0.1R_E$ to $0.14R_E$ in the solar wind and magnetosheath regions. A total grid of $N_r \times N_\phi \times N_\theta = 180 \times 104 \times 130$ is used. The time step to advance the positions of particles is $0.05\Omega_{i0}^{-1}$.

Chapter 3

3-D Global-Scale Simulations of Mode Conversion Processes associated with radial IMFs at the Magnetopause

3.1 Introduction

In order to identify the mode conversion processes in the global system around the dayside magnetosphere, in this chapter I will present 3-D global-scale hybrid simulations of the dayside magnetosphere associated with a quasi-parallel bow shock case, with IMF purely in the B_x direction. In the previous 3-D global hybrid simulations [36], whistler-type electromagnetic waves and compressional waves/pressure pulses generated in the foreshock of the quasi-parallel shock are found to propagate onto the magnetosphere and lead to short wave-length pulses with enhanced parallel electric field in the magnetopause. In this chapter, a detailed analysis will also be presented to show that these waves are the KAWs generated by the mode conversion from the compressional pulses, with a radial IMF $B_{x0} = -B_0$, $B_{y0} = 0$, $B_{z0} = 0$.

3.2 Simulation Results

3.2.1 Overall Structure

Figure 3.1 shows contours of the magnetic field strength B and ion density N in the noon meridian and equatorial planes at $t = 150$. Typical magnetic field lines in the 3-D perspectives are also displayed in the magnetic field contours. The self-consistently generated bow shock is saturated around a standoff radial distance of $12R_E$ at $t = 40$, while the magnetopause is roughly at $10R_E$ in the subsolar region. Compressional pulses in B and N and transverse magnetic field perturbations are present in the magnetosheath, which surrounds

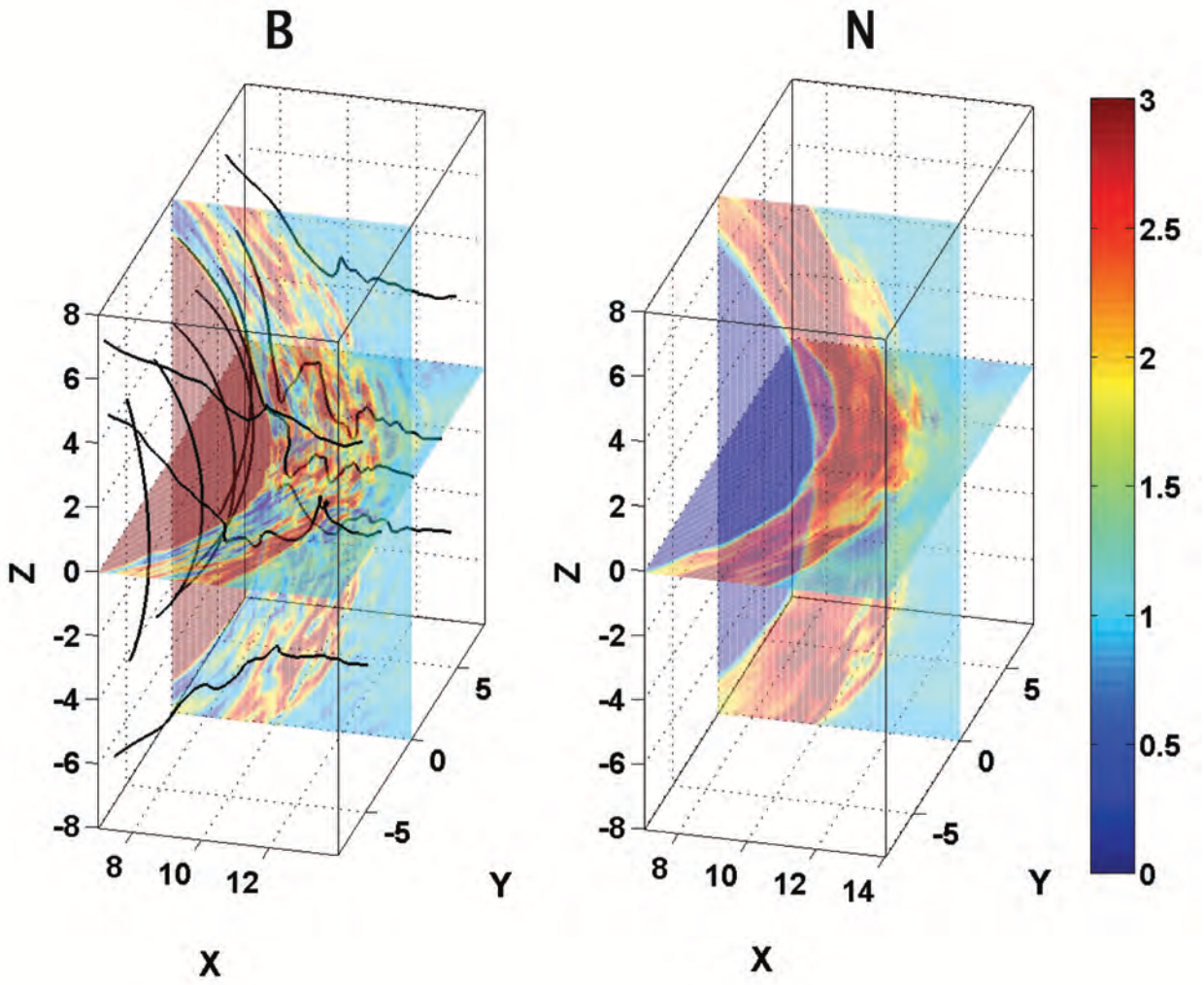

Figure 3.1: Spatial contours of geo-magnetic field strength B and ion density N at $t = 150$ showing the 3-D structures of self-consistently generated bow shock and magnetopause, as well as the compressive pulses in the magnetosheath. Typical field lines are also shown in the magnetic field plot.

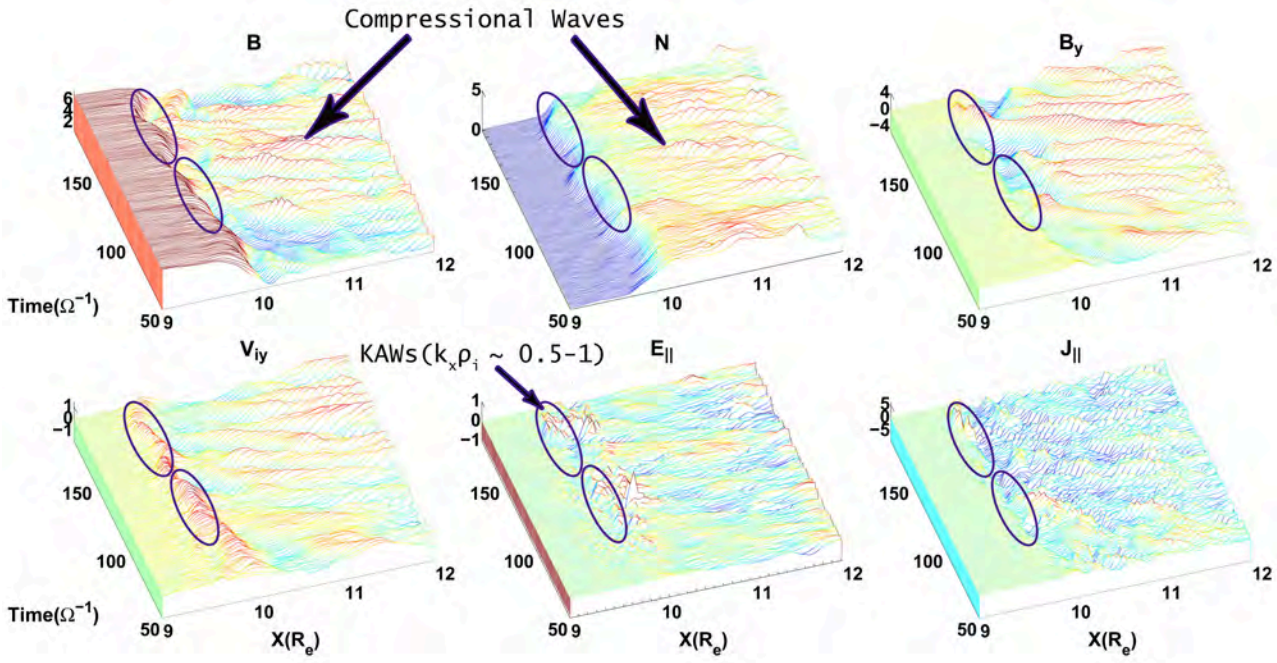

Figure 3.2: Time evolution of spatial profiles of various quantities along the Sun-Earth line during the time interval t = 50 - 180. The circles highlight areas with locally excited $E_{||}$ around the MPBL, which are shown to be KAW structures in later sections.

the magnetosphere and located in the region between the bow shock and magnetopause. The wave perturbations are mainly due to the turbulence in the bow shock and foreshock region generated by backstreaming ions in the foreshock of the quasi-parallel shock [36], which is around the low-latitude regions with $|z| < 3R_E$, and are carried earthward by the shocked solar wind plasma. Specifically, the shock front could be identified from the earthward enhanced magnetic field and ion density. The magnetopause can be distinguished through the sharply increased (decreased) magnetic field (ion density) toward the Earth downstream of the bow shock. In addition to the compressional pulses, diamagnetic cavities with decreased magnetic field and density are also generated in the foreshock (not shown here) and propagate through the magnetosheath. The foreshock compressional waves develop into elongated structures along the field lines, with wave vectors $k_\perp \gg k_{||}$. The dynamics and evolution of the fast-mode/whistler compressional waves and diamagnetic cavities have been simulated in great details [36, 98, 70].

Figure 3.2 illustrates the spatial profiles of various quantities along the Sun-Earth line in a time sequence from t = 50 - 180. The incoming fast-mode compressional wave pulses with perturbations of B and N constantly propagate onto the magnetopause. The oscillating MPBL can be identified from the sharp increase of B and decrease of N around $x = 9.9R_E$. Note that the bow shock is located near $12R_E$ and not shown in Figure 3.2. Specifically, the fast-mode waves generated near the bow shock at about $t = 100$ propagate onto the MPBL at a later time about $t = 120$. The typical Alfvén speed is about $1.4V_{A0}$ around $11R_E$ in the magnetosheath outside the MPBL. At this location, the compressional waves are seen to propagate sunward with a speed about 2 - $3V_{A0}$ in the plasma frame, while the earthward and azimuthal plasma convection speed is about $5V_{A0}$, giving a net wave propagation speed of $\sim$ 2 - $3V_{A0}$ in the simulation (Earth) frame of reference. Near the magnetopause at $x \simeq 10.5R_E$, the x-component velocities of these wave pulses are significantly slowed down. The compressional pulses then consequently impinge on the magnetpause obliquely. In addition, the transverse perturbations can be seen from the profiles of B_y and ion flow velocity V_{iy}.

When the series of wave packets interact with the magnetopause, strong perturbations in the parallel electric field $E_\parallel$ are excited near and inside (shown in circled regions) the MPBL transition, from $t \simeq$ 120 - 140 and 160 - 180. These excited waves are dominated with short wavelengths of $k_x\rho_i \simeq 0.5$ - 1. Meanwhile, perturbations in the parallel current $J_\parallel$, B_y, and V_{iy} are also evident near the magnetopause region. These correlated perturbations can be considered a good indicator of possible signature of KAWs. In the following, I will present a detailed identification of the mode conversion from compressional to transversely dominated KAWs.

3.2.2 Conversion from Compressional Waves in the Magnetosheath to Transverse Waves in the MPBL

Figure 3.3 presents the spatial contours of magnetic field components B_x and B_y, field strength B, ion density N, ion bulk flow velocity components V_{ix}, V_{iy}, and V_{iz}, and parallel current $J_\parallel$ in the equatorial plane at $t = 150$. In this figure, the magnetopause can be identified from the sharp changes in B and N as described above. Wave structures are seen in $r > 10R_E$ in the magnetosheath, with wave fronts largely perpendicular to the magnetopause boundary. Meanwhile, wavy motions are produced at the magnetopause due to the arrival of the compressional waves. The three circles at $y = 5R_E$, $y = 0$ (subsolar region), and $y = -5R_E$ in each plot of Figure 3 mark the regions of strongly distorted magnetopause. Large-amplitude perturbations are seen in B_y, V_{iy}, V_{iz}, and $J_\parallel$ in these magnetopause surface waves. These waves propagate eastward and westward away from the subsolar area along the magnetopause.

To understand the dynamical interaction between the foreshock/magnetosheath waves and the magnetopause, Figures 3.4(a) and 3.4(b) depict time variations of B and N along the sun-earth line at fixed positions $x = 9.8R_E$ and $x = 11.8R_E$, respectively. Figure 3.4(a) shows that at earlier times before $t = 80$, when B is high and N is low, the location $x = 9.8R_E$ is on the magnetospheric side in MPBL. As time goes on, the magnetopause sweeps through this location three times, as seen from the oscillating B and N, so that it is on the magnetosheath side at $t \simeq 180$. The oscillating magnetopause results in the background low-frequency, anti-phase oscillations in B and N. Meanwhile, a remarkable feature is that the high-frequency oscillation structures in Figure 3.4(a) also denote an anti-phase relation between B and N. Therefore, the MPBL is dominated by the anti-phase relation between the magnetic field and the density. On the other hand, the location $x = 11.8R_E$ in Figure 3.4(b) is always in the magnetosheath. No background low-frequency oscillation is found here. The perturbations are of high frequency, dominated by an in-phase relation between B and N but also mixed with a few anti-phase structures. Overall, the wave polarization changes distinctively from

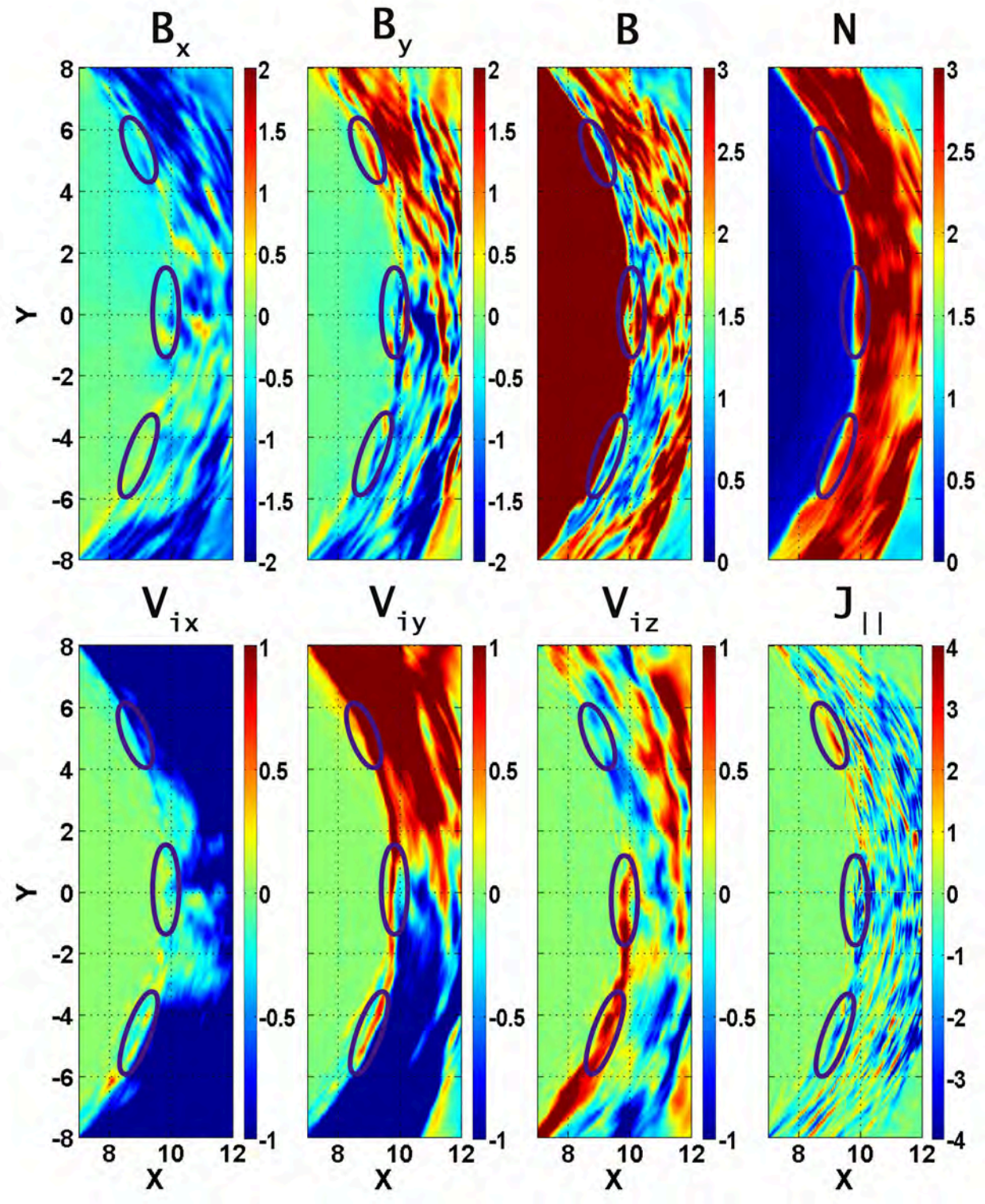

Figure 3.3: Contours of various quantities in the equatorial plane at $t = 150$. The three circles at $y = -5$, 0, $5R_E$ in each plot spot the strong perturbations round the MPBL.

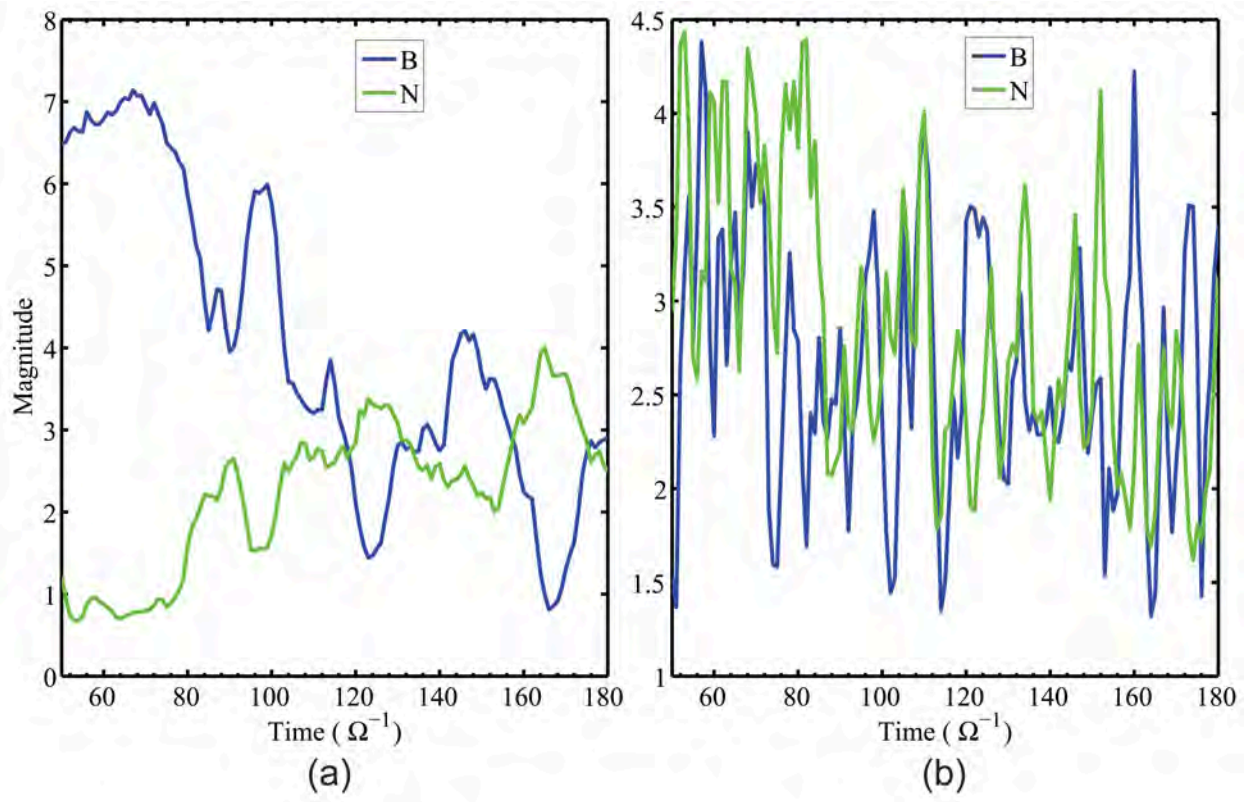

Figure 3.4: Time variations of B and N at two locations along the sun-earth line: (a) anti-phase relation at $x = 9.8R_E$ in the MPBL, and (b) predominantly in-phase relation at $x = 11.8R_E$ in the magnetosheath.

a predominantly in-phase relation between B and N in the magnetosheath to an anti-phase relation in the MPBL.

The power spectra of the transverse (B_y) and compressional (B) components of the magnetic field, as a function of x at $(y, z) = (0.0, -1.0)R_E$, are shown in Figure 3.5. The frequency ω, normalized by the solar wind Ω_{i0}, at various locations is obtained from the simulation data in the time duration from $t = 62$ - 190. During this time interval, the bow shock is oscillating around $x = 12R_E$, and the magnetopause is around $x = 9.8R_E$. The magnetosheath is occupied predominantly by compressional waves, whereas relatively weak transverse wave powers are also present. These waves propagate toward the magnetopause, while they are Doppler-shifted in the simulation (Earth) frame of reference due to the magnetosheath flows, which are spatially dependent. The compressional wave powers in the

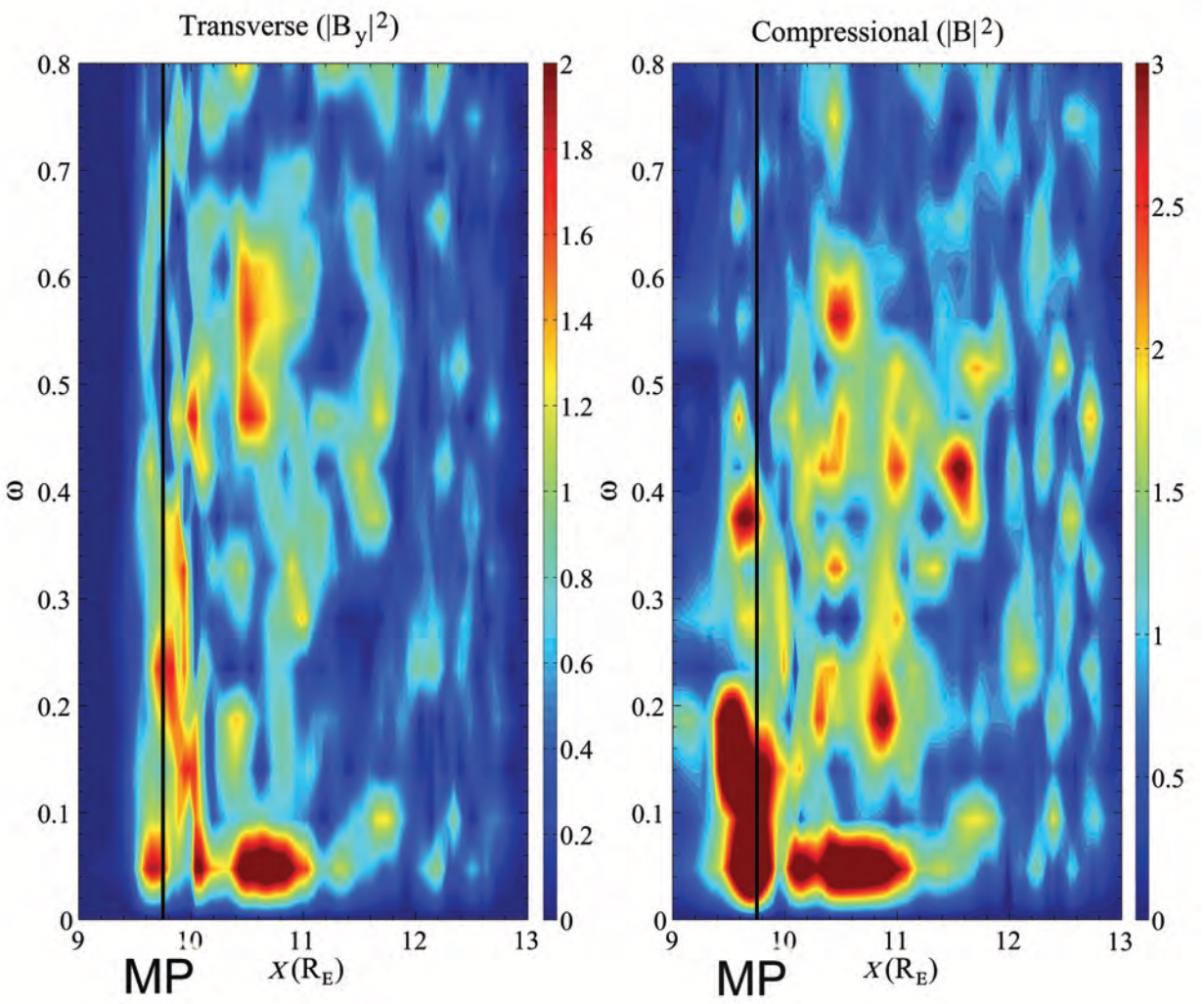

Figure 3.5: Power spectra of transverse and compressional components as a function of x at $(y, z) = (0.0, -1.0)R_E$.

magnetosheath are of broadband, from ω = 0.1 - 1.0. Around the MPBL from x = 9.6 - 10.0R_E, however, significant transverse wave powers appear abruptly, with a spectral width of ω = 0.2 - 0.4. These transverse waves exist in the same region where B and N have an anti-phase relation, as discussed in Figure 3.4(a).

Note that the strong compressional wave power in the MPBL in low frequencies of $\omega \sim$ 0.1 - 0.2 is caused by the oscillation of the magnetopause. Wave powers at a very low frequency, $\omega < 0.1$, is present in both the compressional and transverse oscillations, and in both the magnetosheath and the magnetopause. These powers are caused by a

systematic motion of the entire regions of the magnetosheath and magnetopause. The anti-phase relation between the magnetic field and the density, the dominance of the broadband transverse wave powers in the MPBL, and the excitation of the parallel electric field (shown in Figure 3.2) appear to be consistent with the presence of KAWs through a mode conversion from the compressional waves.

3.2.3 Identification of the Mode Conversion and Generation of KAWs

To further pinpoint the dynamical mode conversion process that may have occurred in the MPBL, I now have presented a detailed analysis of wave structures around the MPBL. Figure 3.6 shows the spatial cut of physical quantities B, N, B_y, $E_\parallel$, and $J_\parallel$ through the magnetopause region along the sun-earth line at $t = 163$, where the magnetic field decreases and the density increases from $x = 9.5$ - $10R_E$. Correspondingly, the local Alfvén speed V_A increases approximately from 0.5 to 9.9 V_{A0} from $x = 10$ - $9.5R_E$ inward.

The parallel wavelength of incoming waves from the magnetosheath is measured to be 3 - $8R_E$ approximately, which corresponds to $k_\parallel \rho_i \sim 0.04$ - 0.1, where $\rho_i \sim 0.5 d_{i0}$ is the local ion Larmor radius. The perpendicular wavelength is about 0.2 - $0.5R_E$, corresponding to $k_\perp \rho_i \sim 0.5$ - 1. The ion gyrofreqency Ω_i is about 4 - $5\Omega_{i0}$ at the magnetopause, while the dominant incident wave frequency ranges from 0.2 - $0.5\Omega_{i0}$, as discussed in Figure 3.5, and thus $\omega^2/\Omega_i^2 \ll 1$. The incident wave has $\omega > k_\parallel V_A$, as described previously. For the average dominant $\omega \sim 0.3\Omega_{i0}$ as measured in the MPBL to be consistent with the frequency due to the mode conversion, the Alfvén resonance condition for the subsolar locations with nearly a zero flow convection speed, $\omega = k_\parallel V_A(1 - \omega^2/\Omega_i^2) \simeq k_\parallel V_A$, requires $V_A \simeq 2.2 V_{A0}$. This value of the Alfvén speed corresponds to $x \simeq 9.75R_E$ as V_A ramps up into the MPBL, as indicated by the yellow vertical line in Figure 3.6.

The spatial profiles of physical quantities around the MPBL confirm the existence of the predicted Alfvén resonance point. Around this average location of the predicted Alfvén resonance point, $E_\parallel$ is strongly enhanced, as seen in Figure 3.6, and it then shows a purely

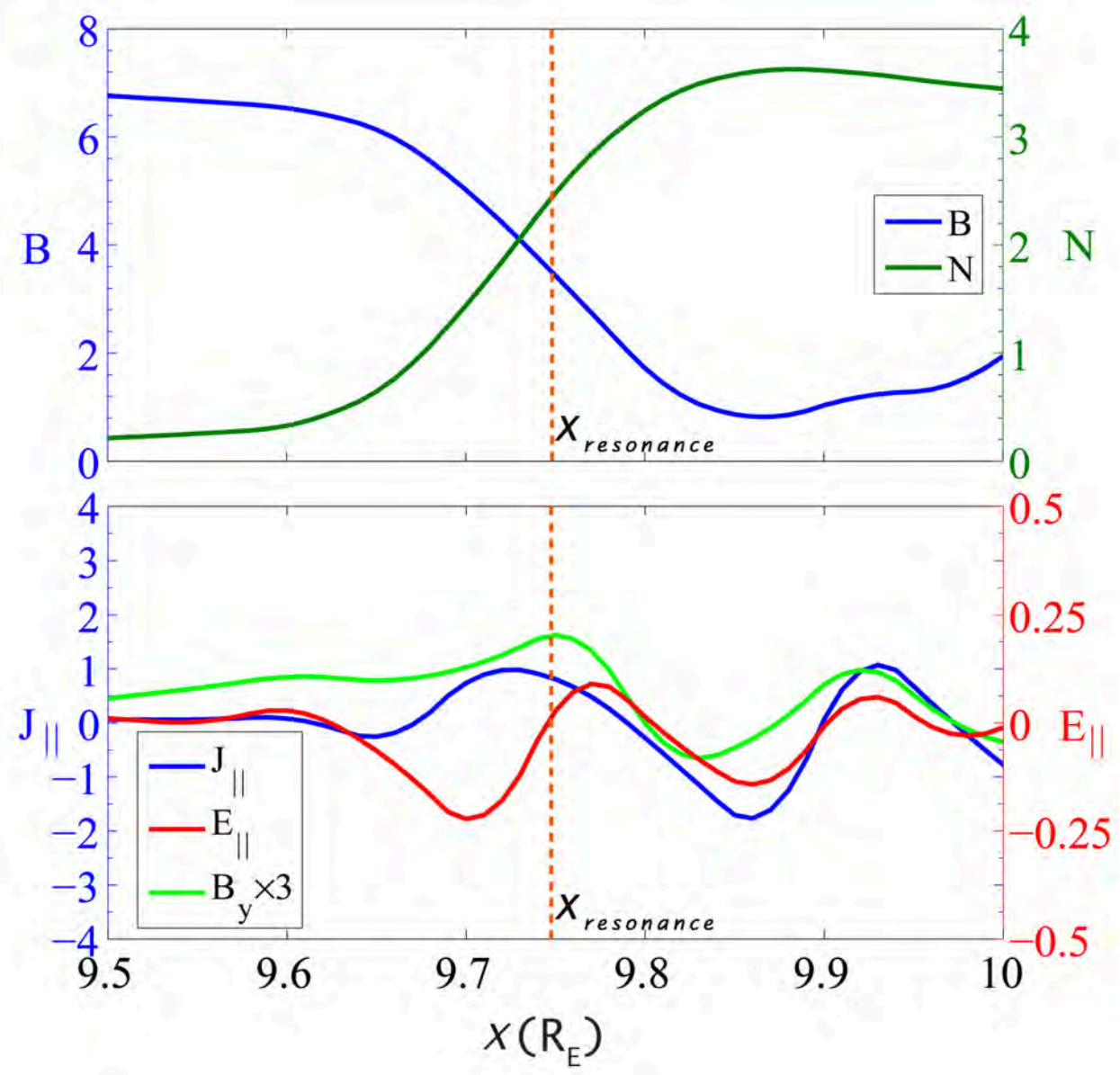

Figure 3.6: Spatial cuts of various quantities through the MPBL along sun-earth line at $t = 163$. The vertical dotted lines mark the average location of the predicted Alfvén resonance point.

decay spatial profile on the magnetospheric side, consistent with theories of the mode conversion [6] shown in Figure 1.9. The waves propagate back to the magnetosheath side. Similar behaviors are seen in $J_\parallel$ and B_y. The correlation of these quantities are consistent with the KAW structures in the analytical theory [6] and previous hybrid simulations of mode conversion for a local magnetopause [87, 7].

The mode-converted Alfvén mode waves can be identified by examining the wave polarization relation. Suppose a background magnetic field pointing in the z direction and a KAW with the wave vector $\mathbf{k}$ in the xz plane, as in the subsolar MPBL. The wave polarizations in Alfvén waves are dominated by perturbations in B_y and E_x. Based on the kinetic theory, $\delta E_x = V_A \delta B_y \left\{1 + T_e/T_i[1 - I_0(\lambda_i)e^{-\lambda_i}]\right\}$ in the KAW, where $\lambda_i = k_x^2\rho_i^2$, and $I_0(\lambda_i)$ is the modified Bessel function of the first kind. In our simulation, $k_x\rho_i \approx 0.5$ - 1, the averaged $T_e/T_i \approx 0.2$ at the magnetopause, and thus $\delta E_x \simeq \sqrt{1 + k_\perp^2\rho_i^2} V_A \delta B_y \simeq 1.1 V_A \delta B_y$ is required for KAWs based on the Pade approximation. Figure 3.7 presents the results at $t = 150$ in the xz plane due to the arrival of pressure pulses at the MPBL. Figure 3.7(a) shows the contours of $E_\parallel$, in which the enhancement of the parallel electric field in the MPBL is highlighted with the circled region. Consistent with the theoretical prediction for KAWs, the waves in the MPBL are found to be dominated by δB_y and δE_x. Figure 3.7(b) shows δE_x vs. δB_y for all the MPBL points inside this circle, with the violet dashed lines marking the polarization relation $\delta E_x = \pm 1.1 V_A \delta B_y$ for KAWs around the subsolar MPBL. The perturbed quantities δB_y and δE_x are defined relative to the "equilibrium" values after $t = 50$, which are calculated by taking the average field values over data time duration from $t = 50$ - 150. Here, V_A is the local Alfvén speed based on the equilibrium magnetic field and density. It is seen from Figure 3.7 that the Alfvén mode polarization relation is nearly satisfied in the circled region. For majority regions outside the MPBL, however, the relation is found to be poorly satisfied.

The signs of slope of the solid lines in Figure 3.7(b) represent the direction of the Alfvén mode propagation along z, which is nearly the direction of the magnetic field lines. In this

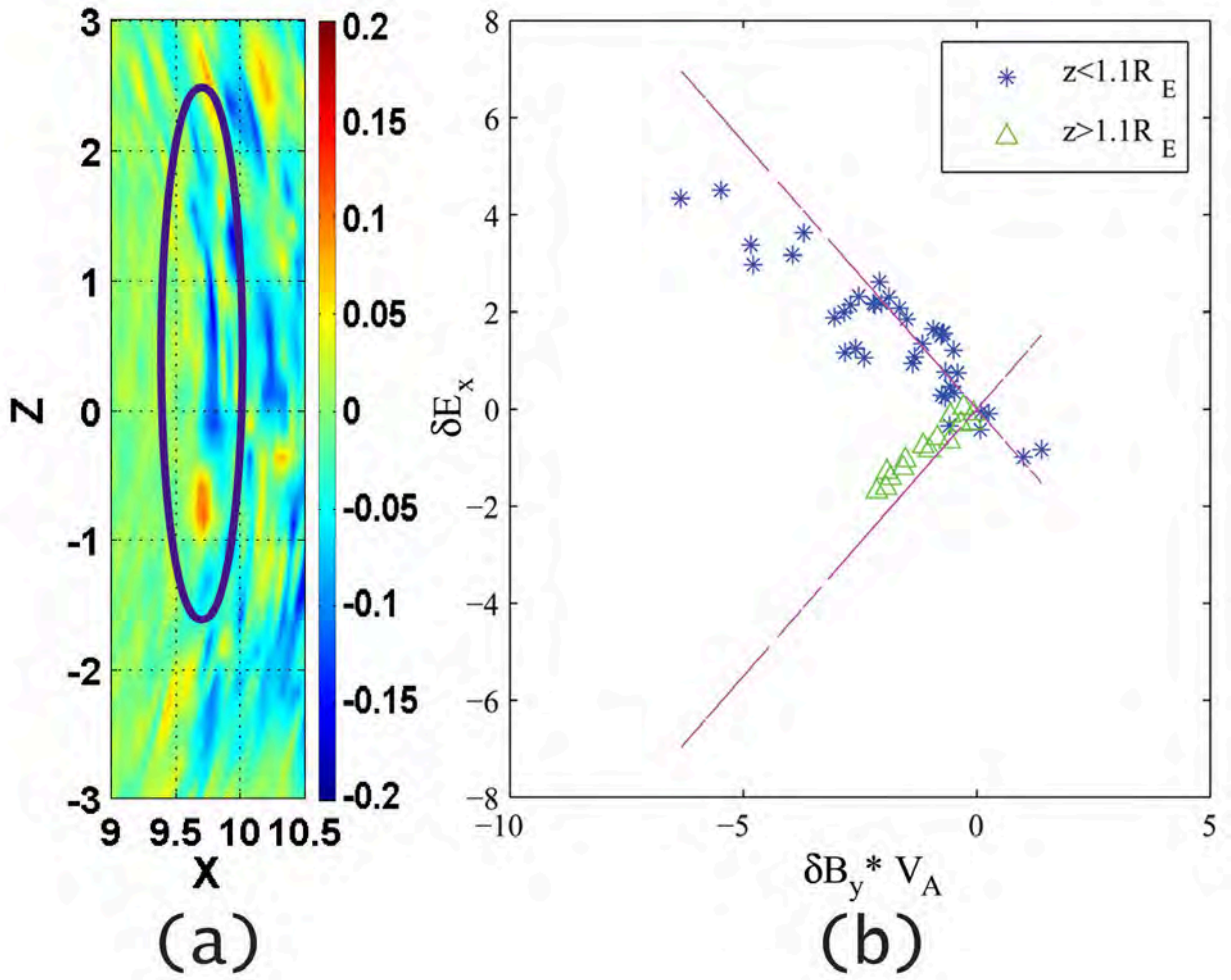

Figure 3.7: (a) Spatial profile of $E_{\parallel}$ around the MPBL in the noon-meridian plane at $t = 150$. (b) Corresponding polarization relation at the spatial points inside the circled regions in (a) showing Alfvén modes propagating in the opposite directions along the field lines. The violet dashed lines in (b) denote the theoretically predicted polarization relation $\delta E_x = \pm 1.1 V_A \delta B_y$ for the KAWs.

case, the wave structures in the MPBL obtained from the simulation consist of two parts: the positive slope for $z > 1.1R_E$, indicating a wave branch traveling northward along the field lines, and the negative slope for $z < 1.1R_E$, denoting another branch propagating southward along the field lines. This result is in agreement with our expectation that pulses coming onto the MPBL would break up into two parts that propagate to the opposite directions along the field lines.

The polarization relation of the waves with an enhanced parallel electric field, again marked by circles, in the equatorial MPBL are shown in Figure 3.8 for $t = 150$ (top row) and $t = 163$ (bottom). The Alfvén mode polarization relation is again nearly satisfied in these waves. The waves in this plane are seen to propagate either northward or southward. Specifically, at $t = 150$, the wave structures in the region with $-1.5R_E < y < -0.85R_E$ have a positive slope in the δE_x-δB_y plot and thus propagate northward. In the region with $-0.85R_E < y < 0$, both positive and negative slopes are seen, and the Alfvén mode waves propagate either northward or southward. In the region with $0 < y < 0.3R_E$, the waves propagate southward along the field lines. At $t = 163$, strongly enhanced $E_\parallel$ is again present in the MPBL, as shown in the bottom left plot of Figure 3.8, due to the arrival of a new pressure pulse. These Alfvén waves now propagate northward with the Alfvén speed, as shown in the bottom right column of Figure 3.8. Moreover, large $k_y\rho_i \sim 1.8$ appears in the wave structures in the MPBL, as seen in the $E_\parallel$ contour plot. The presence of large azimuthal wave numbers is crucial to the particle transport across the field lines. Previous work [7] have shown with simulations of a local slab magnetopause boundary that perpendicular and azimuthal wave numbers can be generated in the 3-D mode conversion due to the nonlinear parametric decay instability of KAWs.

In short, based on the wave polarization relation, the simulation has demonstrated that the resulting waves in the MPBL due to the mode conversion from the compressional pulses are indeed Alfvén mode waves. Together with the properties that these Alfvén waves are

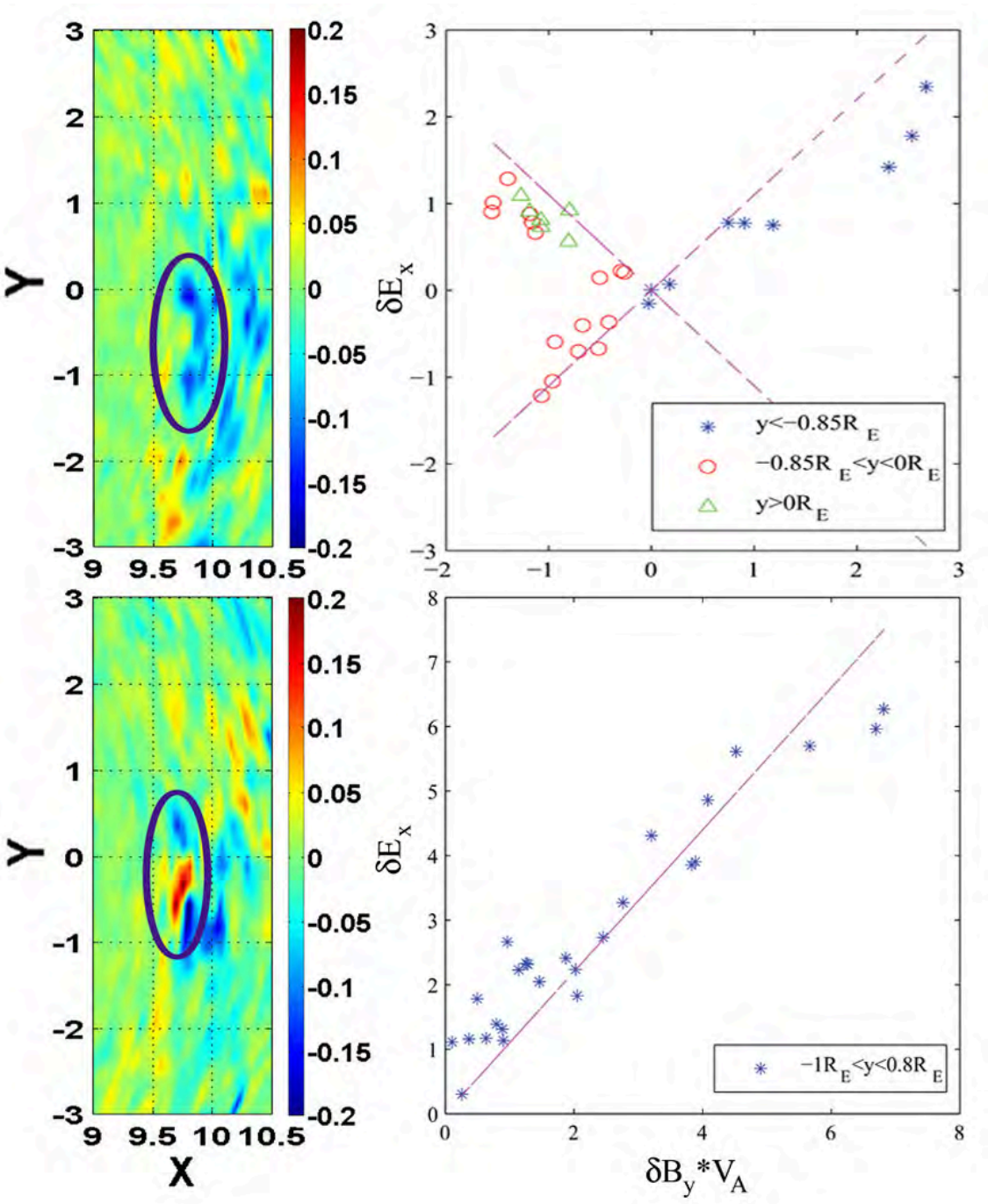

Figure 3.8: Top left: Spatial profile of $E_{\parallel}$ around the MPBL in the equatorial plane at $t = 150$. Top right: Corresponding polarization relation in the circled regions on the top left showing Alfvén modes propagating in different directions along the field lines. Bottom left: Spatial profile of $E_{\parallel}$ around the MPBL in the equatorial plane at $t = 163$; Bottom right: Corresponding polarization relation in the circled regions on the bottom left showing Alfvén modes. The violet dashed lines on left panels represent the theoretically predicted polarization relation $\delta E_x = \pm 1.1 V_A \delta B_y$ for the KAWs.

of large $k_\perp \rho_i$ and with an enhanced $E_\parallel$ and transverse magnetic field perturbations, I have shown that these waves are kinetic Alfvén waves.

3.2.4 Generation and identification of KAWs dominated by the azimuthal wave numbers

Besides the features described above, the $E_\parallel$ structure is seen to have clearly evolved into waves with a large $k_y \rho_i \sim 0.4$ at the later time of $t = 163$ in Figure 3.9. The presence of large azimuthal wave numbers k_y is crucial to the particle transport across the field lines. [7] have found with simulations of a local slab magnetopause boundary that following a stage dominated by the linear physics of mode conversion, which leads to the excitation of KAWs with large k_x, perpendicular and azimuthal $k_y \rho_i$ are generated in the nonlinear stage when the amplitude of KAWs generated by linear mode conversion becomes large enough to drive a nonlinear parametric decay process.

Since the plasma and magnetic field are nearly uniform in the azimuthal direction in the subsolar MPBL, a spectral analysis can be easily performed by Fourier transform in the k_y space. Thus, to further test the dependence of the wave polarization on the wave number, we now analyze the wave spectrum of $E_\perp(k_\perp)/B_\perp(k_\perp)$ from our simulation and compare it with the polarization relation based on the analytical theory of KAWs. The test is performed for the azimuthal k_y modes along a line segment at $x = 9.82R_E$ from $3R_E \leq y \leq 3R_E$, which is located inside the subsolar MPBL. In these modes dominated by k_y, the transverse polarization of the electromagnetic field is dominated by δE_y and δB_x. The dots in Figure 3.9 show the dependence of $E_y(k_y)/B_x(k_y)$ on k_y obtained from the simulation at $t = 150$, where $E_y(k_y)$ and $B_x(k_y)$ are the Fourier spectra of E_y and B_x. The analytical relation, $E_y/B_x \simeq V_A\sqrt{1 + k_y^2\rho_i^2}$ for KAWs dominated by $k_\perp = k_y$ in this case with $T_e/T_i \ll 1$, is also denoted by a green line in Figure 3.9, where the values of the average background Alfvén speed, V_A, at the local line segment is marked at $k_y \sim 0$. The results show a consistency between the simulation and the analytical theory. The predominant wave power in the

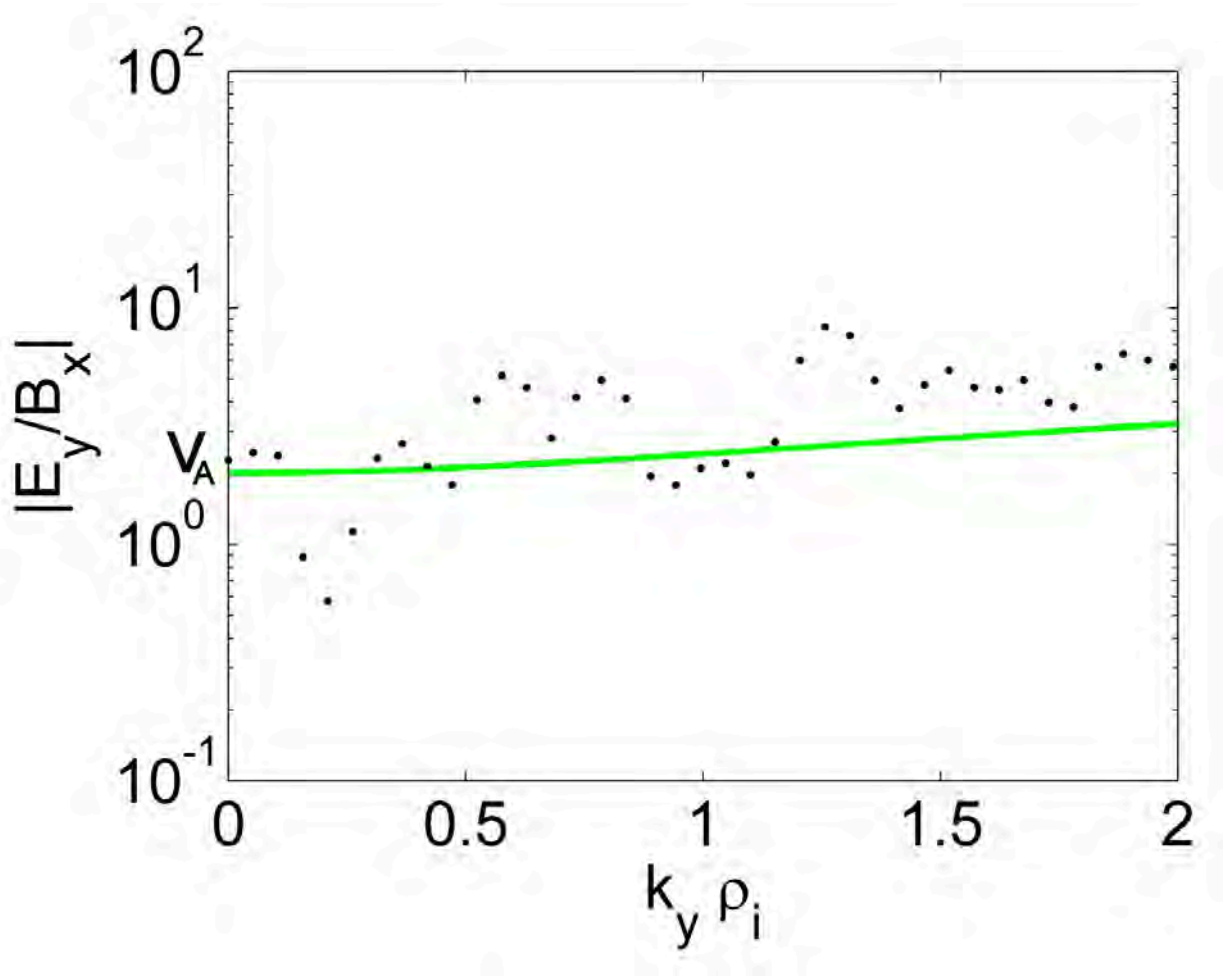

Figure 3.9: The dots show the wave spectrum of $E_y(k_y)/B_x(k_y)$ as a function of k_y for the azimuthal k_y modes of KAWs obtained from the simulation at $x = 9.82R_E$ and $-3R_E \leq y \leq 3R_E$ within the equatorial subsolar MPBL at $t = 150$. The analytical relation $E_y/B_x V_A \sim \sqrt{1 + k_y^2 \rho_i^2}$ is denoted as the green line. The value of the local average background Alfvén speed is marked on the figure at $k_y \sim 0$.

simulation is found to be in the range of $k_y\rho_i \sim 0.3$ - 1. At the higher wave number with $k_y\rho_i \sim 1$ or larger, the waves exhibit the characteristics of KAW modes, whereas at small $k_y\rho_i$ the modes approach the MHD shear Alfvén wave. The results are also consistent with satellite observations of KAWs at the magnetopause [4, 62, 74], in which $k_\perp$ is typically inferred from measurements as a Doppler shifted frequency using the Taylor hypothesis so that a plot of the frequency spectrum shows that the wave becomes electrostatic at higher frequency.

In order to determine whether the magnitude of the excited $E_\parallel$ is consistent with that predicted by theories of mode conversion, the dots in Figure 3.10 depict the ratio $|E_\parallel(k_y)|/|E_y(k_y)|$ as a function of k_y obtained from the simulation for the same line segment as that exploited to obtain Figure 3.9. Note that the modes dominated by k_x due to the linear mode conversion have $k_y = 0$ [87], whereas the $k_y = 0$ modes are excluded in Figure 3.10. The analytical relation, $\left|\delta E_\parallel\right| / \left|\delta E_\perp\right| = \left(k_\perp\rho_i\right)\left(k_\parallel\rho_i\right)\left(T_e/T_i\right) / \left(1 + k_\perp^2\rho_i^2\right)$, based on the two-fluid linear theory [6, 99, 21, 27] are denoted by the green line in Figure 3.10, where $E_\perp = E_y$ for these modes dominated by $k_\perp = k_y$. It is found that the strength of the parallel electric field obtained from the simulation is in good agreement with that of the KAWs predicted by the theory. Such result is also consistent with the previous hybrid simulation of mode conversion [87].

In addition, by comparing the values of $E_{TD} = -\left[m_i v_{i\perp}^2 / \left(2\bar{B}\right)\right] ik_\parallel B_\parallel\left(k_y\right)/e$ and $E_{LD} = E_\parallel\left(k_y\right)$ (with $\bar{B}$ being the background magnetic field strength), which represent the effective parallel electric field associated with the transit time damping and the Landau damping based on the quasilinear theory [62], respectively, it is found that the magnitude of the transit time damping is roughly 4 - 8 times of that of the Landau damping, consistent with theories [27] and observations [62]. Moreover, the previous theoretical study of [25] has also indicated that magnetic drift effects contribute significantly to the diffusion coefficient in the mode conversion at the magnetopause. Detailed analysis on ion cross-field line diffusion in the mode conversion in our simulation is beyond the scope of this paper. Our examination also

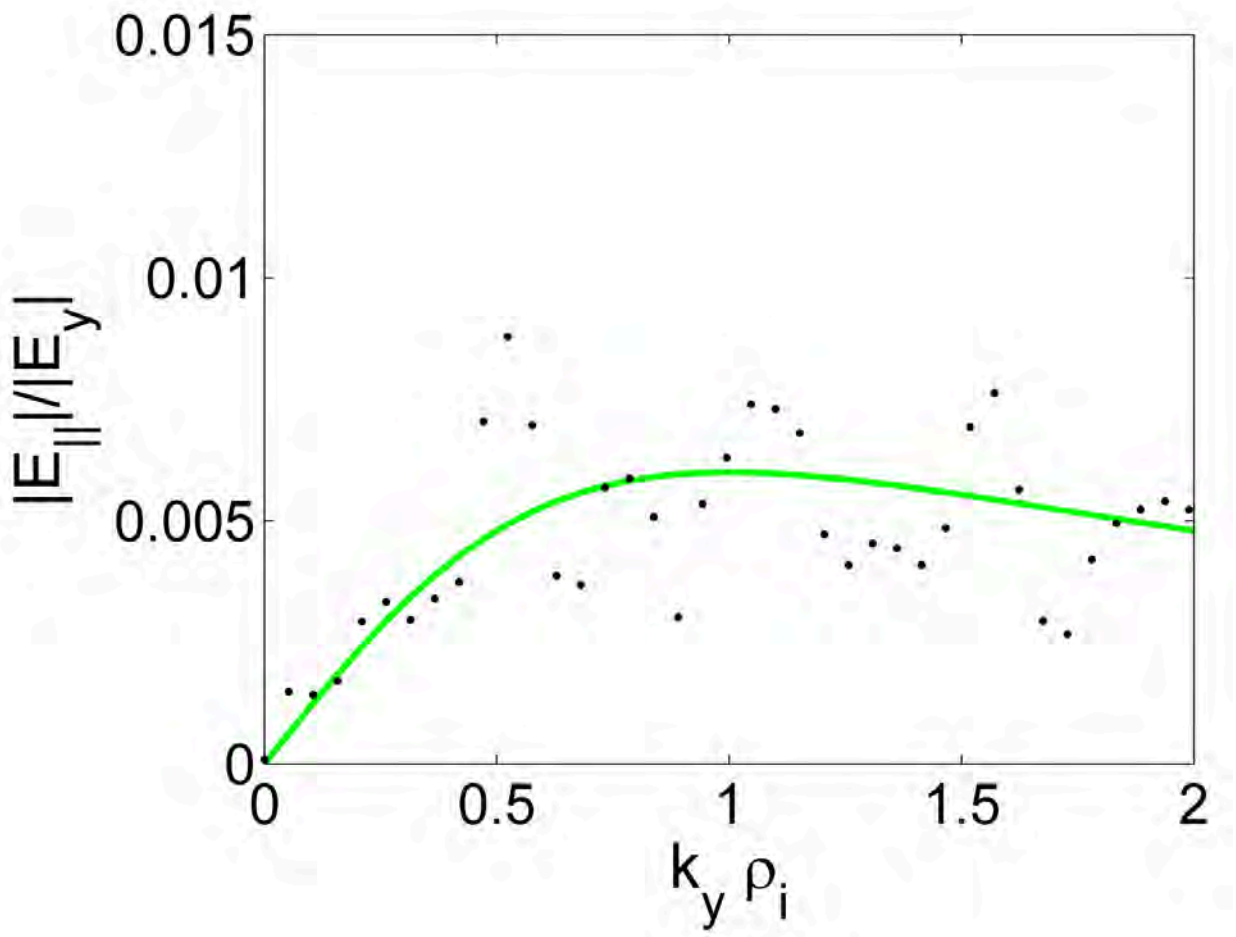

Figure 3.10: Ratio of $|E_\parallel(k_y)|/|E_y(k_y)|$ for the azimuthal k_y modes of KAWs in the subsolar MPBL, along the same line adopted in Figure 3.9, at $t = 150$. The dots are obtained from the simulation, and the green line indicates the relation $(k_y\rho_i)(k_z\rho_i)(T_e/T_i)/(1 + k_y^2\rho_i^2)$ obtained from the two-fluid linear theory.

shows that the presence of $\delta B_\parallel$, which is in an anti-phase relation with δN as seen in Figure 3.4, is consistent with the total pressure balance, $\delta B_\parallel/\bar{B} = -\mu_0 \delta P_i/\bar{B}^2 = -\mu_0 \left(T_0 \delta N_i\right)/\bar{B}^2$, in this high beta plasma. Consider the quasi-charge neutrality for $\omega^2 \ll k_\perp^2 V_A^2$ in KAWs. With the density perturbation $\delta N/N_0 = \left(ie/k_\parallel\right) \delta E_\parallel/T_e$ in the KAWs [6, 78], the pressure balance leads to $\delta B_\parallel/\bar{B} \sim (-\beta_i/2) \left[\left(k_y\rho_i\right)^2/(1 + (k_y\rho_i)^2)\right] \left[ie\delta E_y/\left(k_y T_i\right)\right]$, which is nearly satisfied in our simulation for the predominant spectral range $k_y\rho_i \sim 0.3$ - 1.

Simply put, based on the wave polarization relation and spectral analysis in sections 3.2.3 and 3.2.4, the simulation has demonstrated that the resulting waves in the MPBL due to the mode conversion from the compressional pulses are kinetic Alfvén mode waves indeed.

3.2.5 Global Distribution and Poleward Propagation of the Alfvén Waves

In order to examine the longitudinal and latitudinal structures associated with the mode conversion, the plot of $E_\parallel$ and B_y around the subsolar region at $t = 163$ is presented in Figure 3.11. The contours are shown for equatorial plane ($z = 0$) between $x = 9R_E$ and $10.5R_E$ and $y = -2R_E$ and $2R_E$, the noon meridian plane ($y = 0$) between $x = 9R_E$ and $10.5R_E$ and $z = -2R_E$ and $2R_E$, and the plane with $x = 9.75R_E$. Typical magnetic field lines within this region are also plotted, with arrows indicating the field directions. At this moment, more pressure pulses hit the dusk side of $y = 0$ than the dawn side, leading to strongly correlated perturbations in the parallel electric field and the azimuthal magnetic field perturbations. A transition from the magnetosheath-like field lines to the dipole-like lines (ordered and predominantly northward) is observed. The Alfvénic transverse kinks in the field lines are pronounced in the regions with the enhanced perturbations in $E_\parallel$ and B_y. These perturbations are carried away from subsolar area by the convective flows.

Now, I will discuss the poleward movement of Alfvén waves originating from the subsolar region due to the mode conversion. The northward propagation of KAWs will be focused. The subsolar region is abundant of compressional drivers in front of the magnetopause. As a

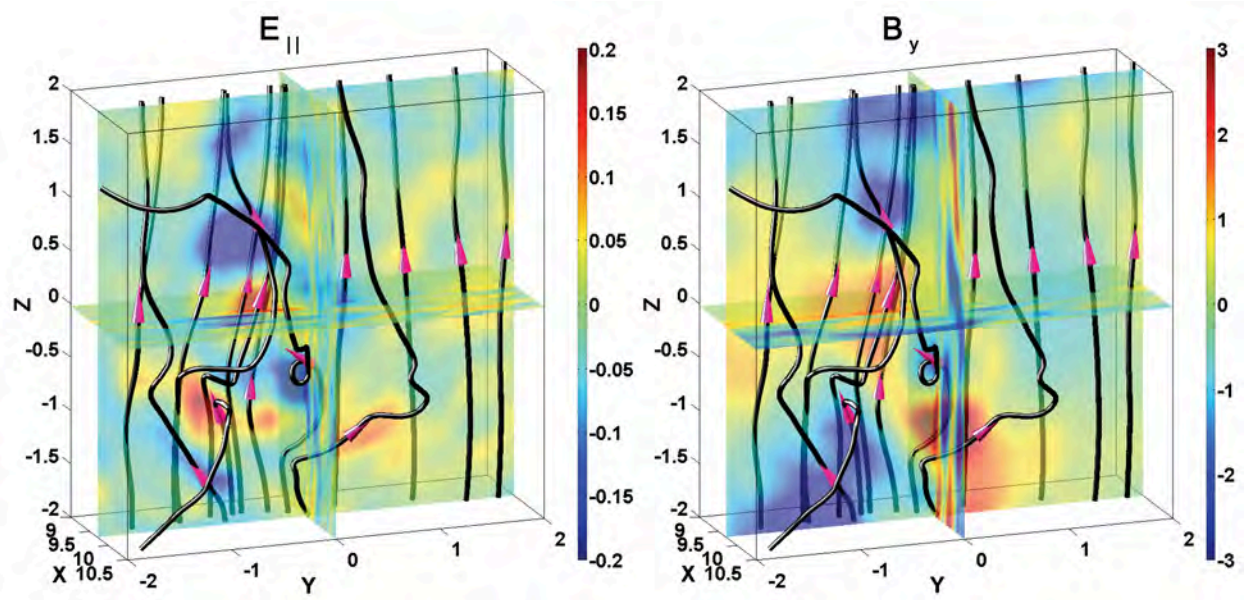

Figure 3.11: Contours of $E_{\|}$ and B_y around the subsolar region at $t = 163$, for equatorial plane ($z = 0$) between $x = 9R_E$ and $10.5R_E$ and $y = -2R_E$ and $2R_E$, the noon meridian plane ($y = 0$) between $x = 9R_E$ and $10.5R_E$ and $z = -2R_E$ and $2R_E$, and the plane with $x = 9.75R_E$. Typical magnetic field lines within this region are also plotted, with arrows indicating the field directions.

result, KAWs continuously form in the subsolar area, i.e., downstream of the quasi-parallel shock. They are seen to propagate along the field lines down to the cusp region.

Figure 3.12 shows the contours of B_y, $J_\parallel$, and the field-aligned Poynting vector $S_\parallel$ at three different times (t = 120, 140, and 164) in the noon meridian plane around the magnetopause boundary, from $r = 6R_E$ to $10R_E$, where $S_\parallel = (\delta\mathbf{E} \times \delta\mathbf{B}) \cdot \mathbf{b}$, and $\mathbf{b} = \mathbf{B}/B$. The sequential propagation of a group of KAWs is tracked with circled regions in Figure 3.12. At $t = 120$, a compressional pulse has come onto the magnetopause, and meanwhile strong perturbations in B_y, $J_\parallel$, and $S_\parallel$ are seen from $z = -0.5R_E$ to $z = 1.5R_E$ around the magnetopause, inside the circled subsolar region in the left column. Another strong perturbation (advent with magnetic pulses at an earlier time $t \simeq 114$) from $z = 1R_E$ to $z = 3R_E$ can be distinguished in the northern part of the circled region as well. The quantities B_y, $J_\parallel$, and the positive (poleward) $S_\parallel$ are well correlated in these KAWs. The propagation speeds of both the leading and trailing edges of the white circle in this subsolar region with an ignorable flow convection are estimated at about V_A in the Earth frame, as expected for the Alfvén modes. KAW perturbations formed at earlier times can also be seen ahead of the tracked KAWs in the higher latitudes along the magnetopause. For a typical IMF of $10nT$ and a solar wind density of $5/c.c.$, $S_\parallel$ is $\sim 1.5 \times 10^{-5} W/m^2$ averaged over the wave packet period, consistent with the observations of [4].

At $t = 140$, the circled region is elongated and expands along the magnetopause due to the larger background convection speed of the leading edge as it moves to a higher latitude, as seen in the middle column of Figure 3.12. The B_y perturbations in the middle part of these KAWs thus appear weaker due to the expansion, at $z \simeq 4.5R_E$. But the trailing part is then merged with KAWs generated by some newly arriving pressure pulses. Enhancement of the local perturbations in B_y and $J_\parallel$ appear at $z \simeq 2.5R_E$. Enhanced poleward $S_\parallel$ again exists correspondingly. The propagation speed of the leading part of the KAW perturbations is roughly equal to $4V_{A0}$, and that of the trailing part is about $1.8V_{A0}$. The convective flow speed $V_z \sim 2.0V_{A0}$ at the leading edge, where the local Alfvén speed is around 2 - $2.5V_{A0}$.

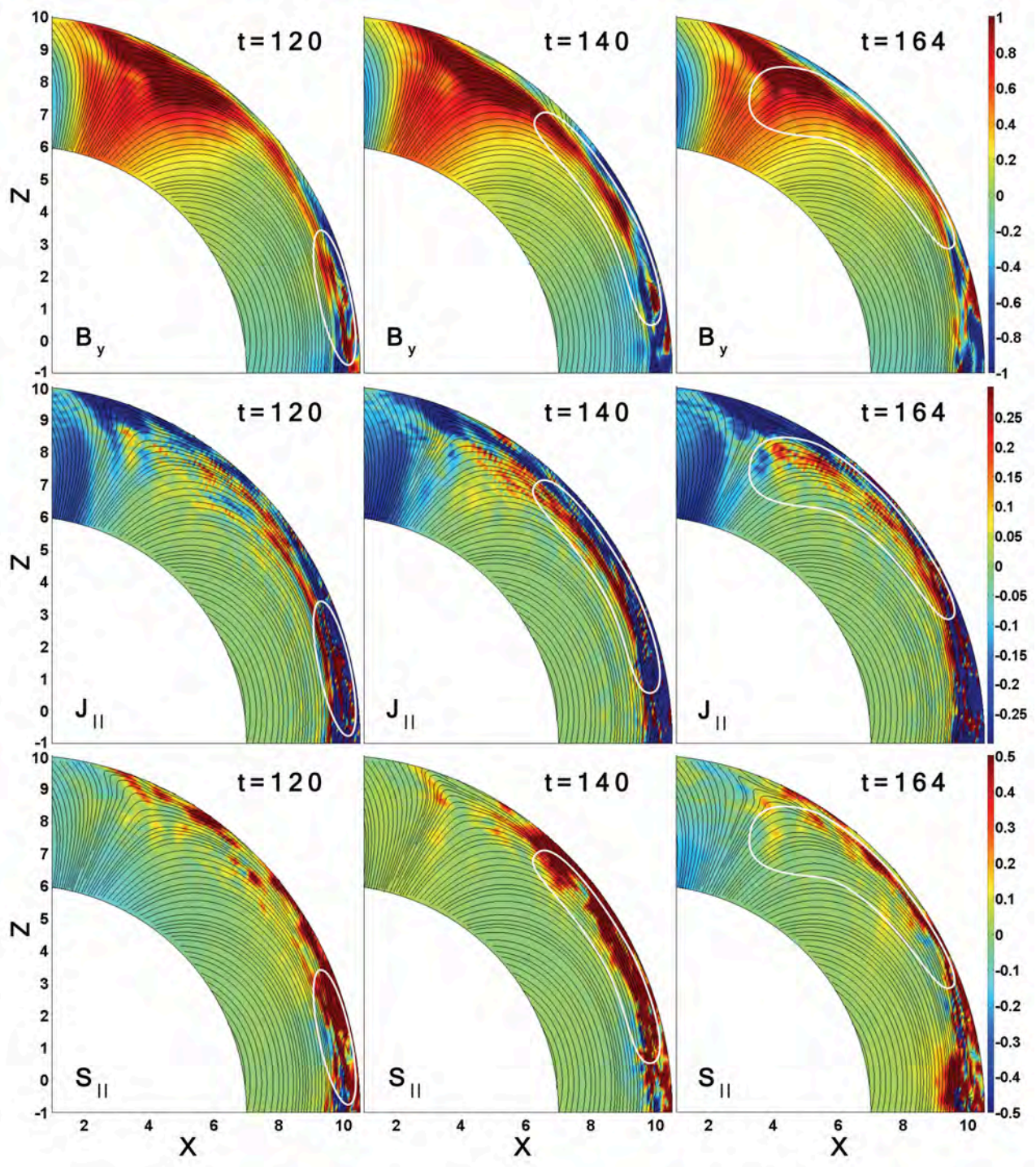

Figure 3.12: Contours of (top row) B_y, (middle) $J_\parallel$, and (bottom) the field-aligned Poynting flux $S_\parallel$ at three different times $t = 120$, 140, and 164 in the noon meridian plane around the magnetopause boundary, from $r = 6R_E$ to $10R_E$. The sequential propagation of a group of KAWs is tracked with the circled regions.

Therefore, the propagation speed of the leading part is about 80 - 90% of its local V_A in the wave frame, very close to the theoretical prediction based on Alfvén waves. The propagation speed of the trailing part appears to be much smaller than the theoretically predicted speed, mainly because of the merging with newly formed KAWs at the local magnetopause. In addition, note that the radial transmission of the foreshock compressional waves also leads to the resonance of closed field lines in the dipole field region [5]. The global generation of Alfvén waves and the field line resonance in the outer magnetosphere has been discussed by Lin and Wang [36] for a case similar to the one presented here.

At $t = 164$, the north-south expansion of the circled region causes further weakened perturbations in the trailing part. In the circled region, the perturbations are seen deeper radially inside the outer magnetosphere. The leading part of the tracked KAW perturbations has propagated into the northern cusp region, where the wave patterns have reached $(x, z) = (3.5, 7.0)R_E$, as seen in the right column of Figure 3.12. Overall, pulses of newly-formed KAWs on the closed field lines continuously propagate into the cusp due to the self-consistent interaction of the magnetopause with foreshock waves.

3.3 Effects of Mach Number: Subcritical Shock

In the theoretical descriptions of collisionless shock waves, when interplanetary plasma's Alfvén Mach number exceeds a certain "critical" Mach number ($\sim$ 2 - 3), no continuous solutions to the fluid dynamic equations exist if resistivity is the only transport coefficient, and an additional dissipative process (traditionally ion viscosity) must be included in order to attain solutions [100]. Thus, for the collisionless shocks the case of $M_A \simeq 3$, above which the dispersive shocks dominate, is termed as "subcritical" Mach number conventionally [101]. Although the encounter of subcritcal Q-$\parallel$ shocks in geo-space are relatively rare, the persistence of large amplitude and low frequency magnetic fluctuations downstream from the shock ramps, with lower-amplitude waves extending upstream, consists of unique features that do not exist in higher Mach number shocks [102, 103, 104]. Numerous simulations of

such subcritical shocks found that the broadened shock ramps are quite different from those of re-forming shocks achieved at higher Mach numbers [105, 106]. Other numerical studies also show that, unlike the cases at higher Mach numbers, the wave group velocity is directed upstream away from the shock and thus no energy returns to the shock [107]. Consequently, not only are the downstreams of the subcritical shocks distinct from the ones of higher Mach number shocks, but even the patterns of the magnetopause may be quite different from those at higher Mach numbers. Besides, the mode conversion process associated with a subcritical Q-∥ shock has been reported. Therefore, in this section, I will make some discussion of the impact of a radial IMF associated with a subcritical Q-∥ shock ($M_A = 3$) on the mode conversion process at the dayside magnetopause, as the title of this section stands. But because a thorough identification of mode conversion process at the dayside MPBL has been conducted in the previous section, I will make comparisons and emphasize the major differences in the presence of subcritical Q-∥ bow shock, also referred to as "switch-on" shock [108, 109].

3.3.1 Overall Structures for the Case of $M_A = 3$

The 3-D structures of B, with typical field lines, and N at $t = 80$ are shown in Figure 3.13. The most striking feature that is quite different from the previous case is the much weaker magnitude of the magnetic pulses in the magnetosheath and the much thicker magnetosheath. Specifically, when M_A decreases, the foreshock waves are carried downstream less significantly. As a result, we see weaker magnetic pulses (earthward propagation in the Earth/simulation frame of reference) in the magnetosheath, shown in Figure 3.14. In the time sequence from $t = 80$ - 90, the oscillating MPBL can be recognized around $x = 10.5R_E$. Note that, albeit the weaker perturbations can be distinguished in both B and N, compared with $M_A = 5$, the interaction time between pulses and the MPBL can be much longer, since the solar wind plasma, whose convective speeds are much lower, carries the relative small magnitude pulses away less quickly in x-direction. $E_\parallel$, therefore, regarded as one of the

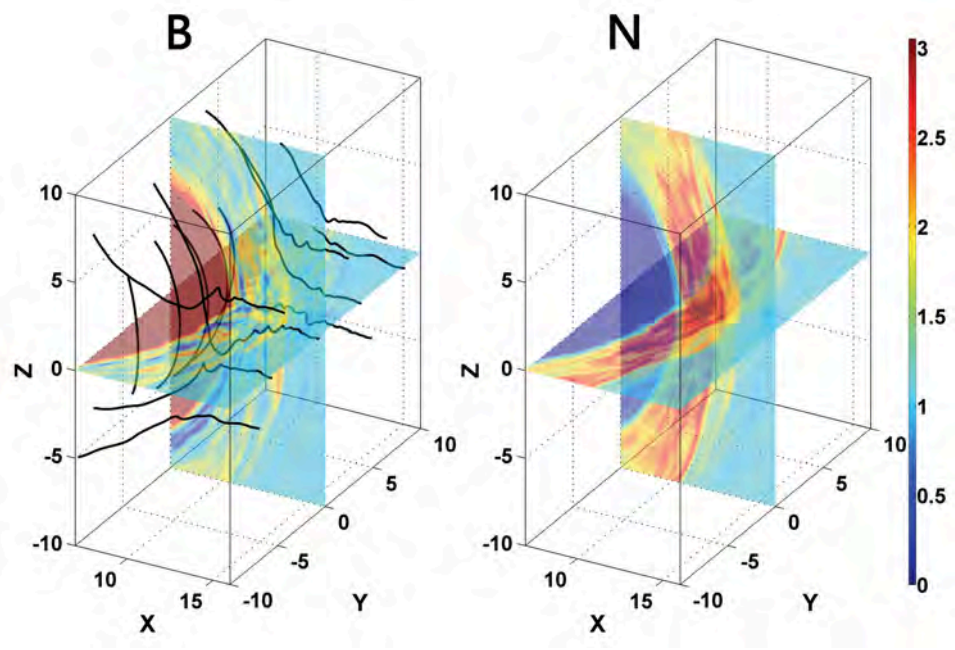

Figure 3.13: Spatial contours of geo-magnetic field strength B and ion density N at $t = 80$ showing the 3-D structures of self-consistently generated bow shock and magnetopause, with IMF $M_A = 3$. Typical field lines are also shown in the magnetic field plot.

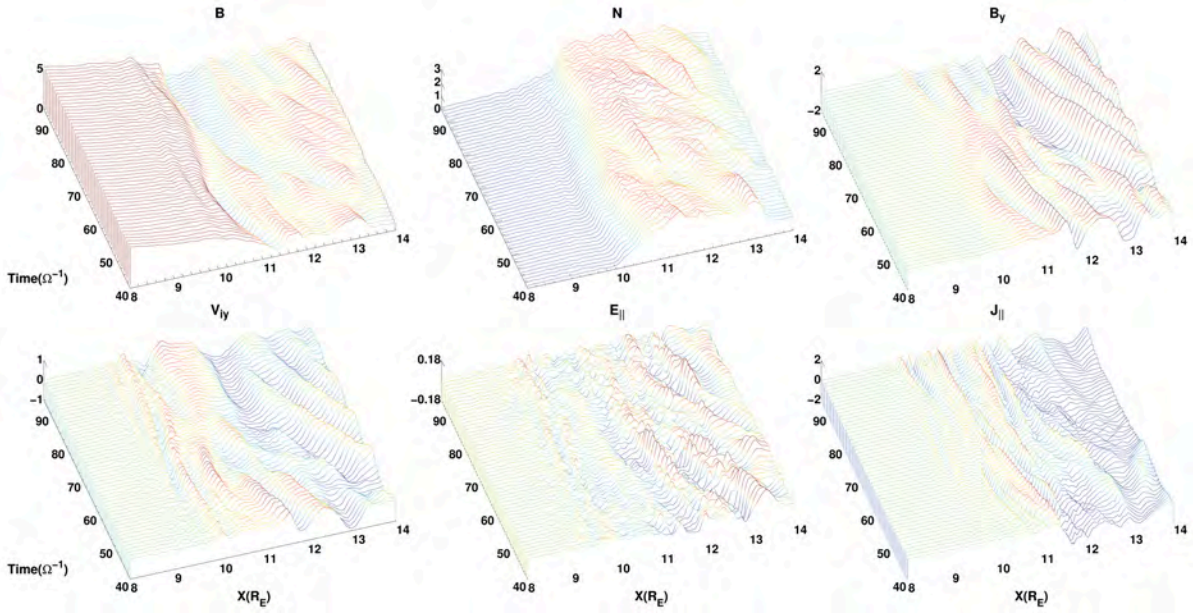

Figure 3.14: Time evolution of spatial profiles of various quantities along the Sun-Earth line during the time interval $t = 40$ - 95, with IMF $M_A = 3$.

most common signatures of KAWs, comes to be much weaker. Also in Figure 3.14, we can see that typical fast-mode wave packets propagate from bow shock at about $t = 40$ to the MPBL at about $t = 80$. The local Alfvén speed is about 0.8 - $0.9V_{A0}$ around $11R_E$, where the compressive waves travel toward the earth with a speed $\sim 2V_{A0}$ in the plasma frame. At this location, the total plasma convection speed is $\sim 3V_{A0}$, so that a net wave propagation speed of $\sim V_{A0}$ in the simulation frame is given, consistent with other hybrid simulations of such shocks [107, 110].

3.3.2 Identification of the Mode Conversion with $M_A = 3$

The spatial contours of B_x, B_y, B, N, V_{ix}, V_{iy}, V_{iz} and $J_\parallel$ are given in Figure 3.15. The results are similar to the $M_A = 5$ case. We can also see the transition of phase relation in Figure 3.16. As discussed in Section 3.2.2 and seen from Figure 3.16, the magnetopause oscillated and swept over the spatial position $(10.5, 0.0, 0.0)R_E$ at times about $t = 50$ and 65, respectively. Figure 3.17 shows the spatial cuts of B, N, B_y, $E_\parallel$ and $J_\parallel$ through the MPBL region along the Sun-Earth line at $t = 93$. Compared to Figure 3.6, one can clearly see a much broader MPBL, with a thickness of almost $1R_E$. Although it shows a much weaker field-aligned current and electric field as discussed above, the overall decay profile on the magnetosphere side, as well as the wave behavior and correlations shown in B_y, $E_\parallel$ and $J_\parallel$, is consistent with theories [6] and the previous case. On the magnetospheric side, however, a series of short wavelength structures of KAW can be perceived, which is different from higher Mach number case where such laminar k_x modes are not observed. Due to the larger and slower oscillations of the MPBL, as well as the non-monotonic magnetosonic and whistler waves downstream of the shock ramp [110, 108], the mode conversion point could change more dramatically over time and space, which may be the reason that the waves are so wide into the left side of the mode conversion point at this moment. In this subcritical shock case of radial IMF, the parallel and perpendicular wavelength is approximately 3 - $8R_E$ and 0.2 - $0.5R_E$, respectively, which is similar to the previous case of $M_A = 5$. The

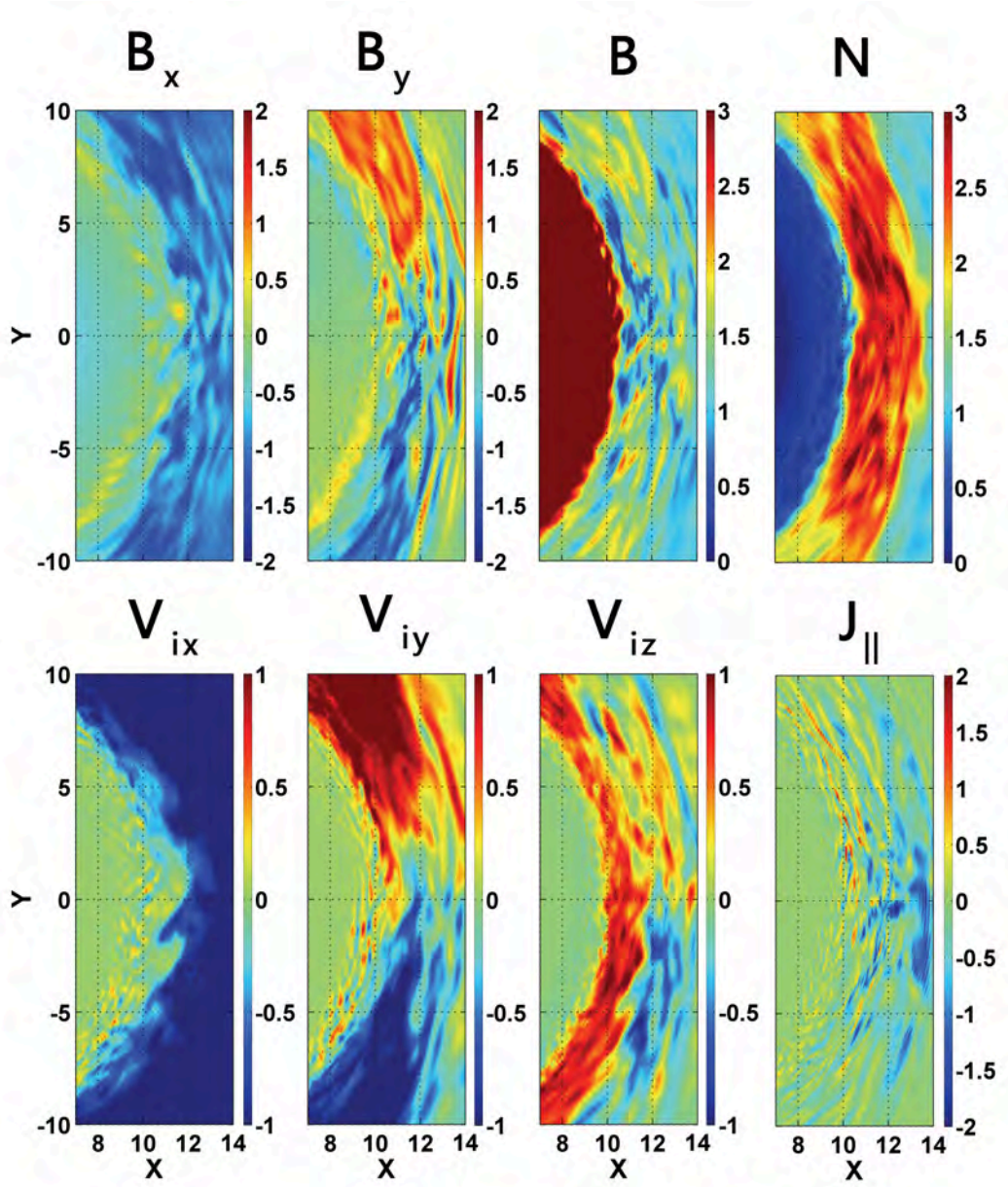

Figure 3.15: Contours of various quantities in the equatorial plane at $t = 89$, with IMF $M_A = 3$.

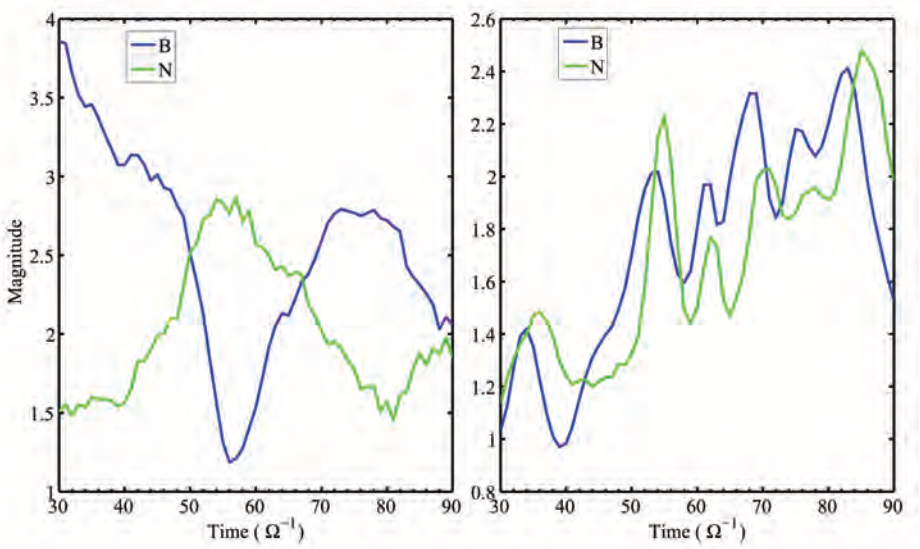

Figure 3.16: Time variations of B and N at two locations along the sun-earth line: (a) anti-phase relation at $x = 10.5R_E$ in MPBL, and (b) in-phase relation at $x = 13.5R_E$ in the magnetosheath, with IMF $M_A = 3$.

relation $\omega^2/\Omega_i^2 \ll 1$ is still justified, with the incident waves $\omega > k_\parallel V_A$. The KAWs' wave polarization relation at $t = 89$ in the subsolar MPBL is shown in Figure 3.18. Again, the relation $\delta E_x \sim 1.1 V_A \delta B_y$ still holds for the similar parameters. In Figure 3.18, the Alfvén mode polarization relation is also nearly satisfied, and the 3-D structures of k_x and k_y modes of KAW aroused in the MPBL could be perceived. The same conclusions regarding to the KAWs' wave structures, therefore, can still be drawn in this critical Mach number case, but with much weaker amplitudes of the wave structures.

3.4 Summary

In summary, I have presented a 3-D global hybrid simulation of mode conversion at the dayside magnetopause associated with the quasi-parallel shock, with radial component only in IMF. The mode conversion from compressional waves originating at the bow shock/foreshock to KAWs is investigated. The main results can be summarized as follows.

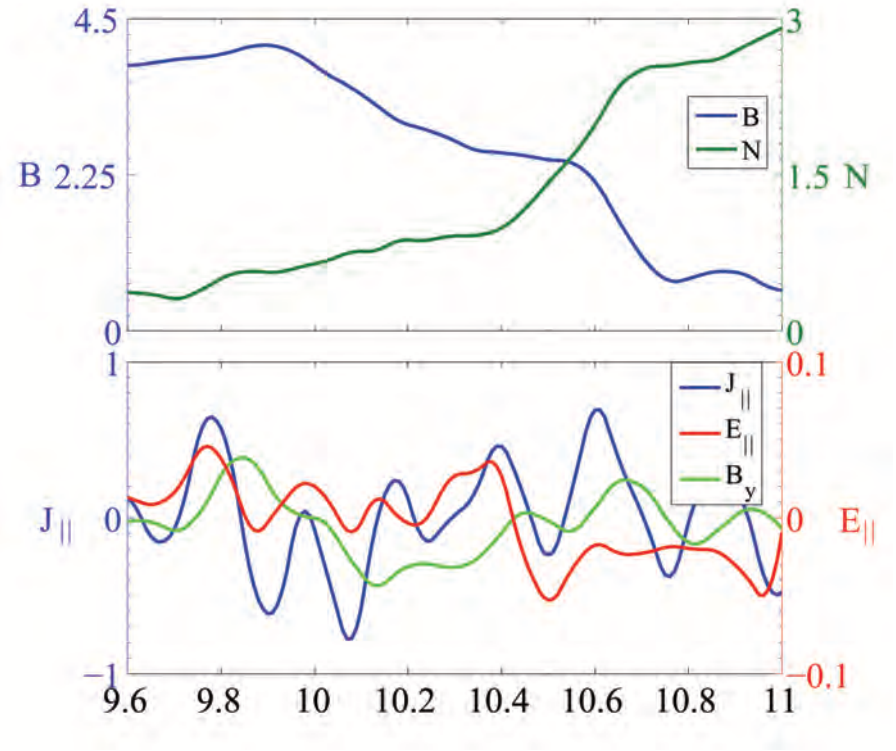

Figure 3.17: Spatial cuts of vairious quantities through the MPBL along the Sun-Earth line at $t = 93$, with IMF $M_A = 3$.

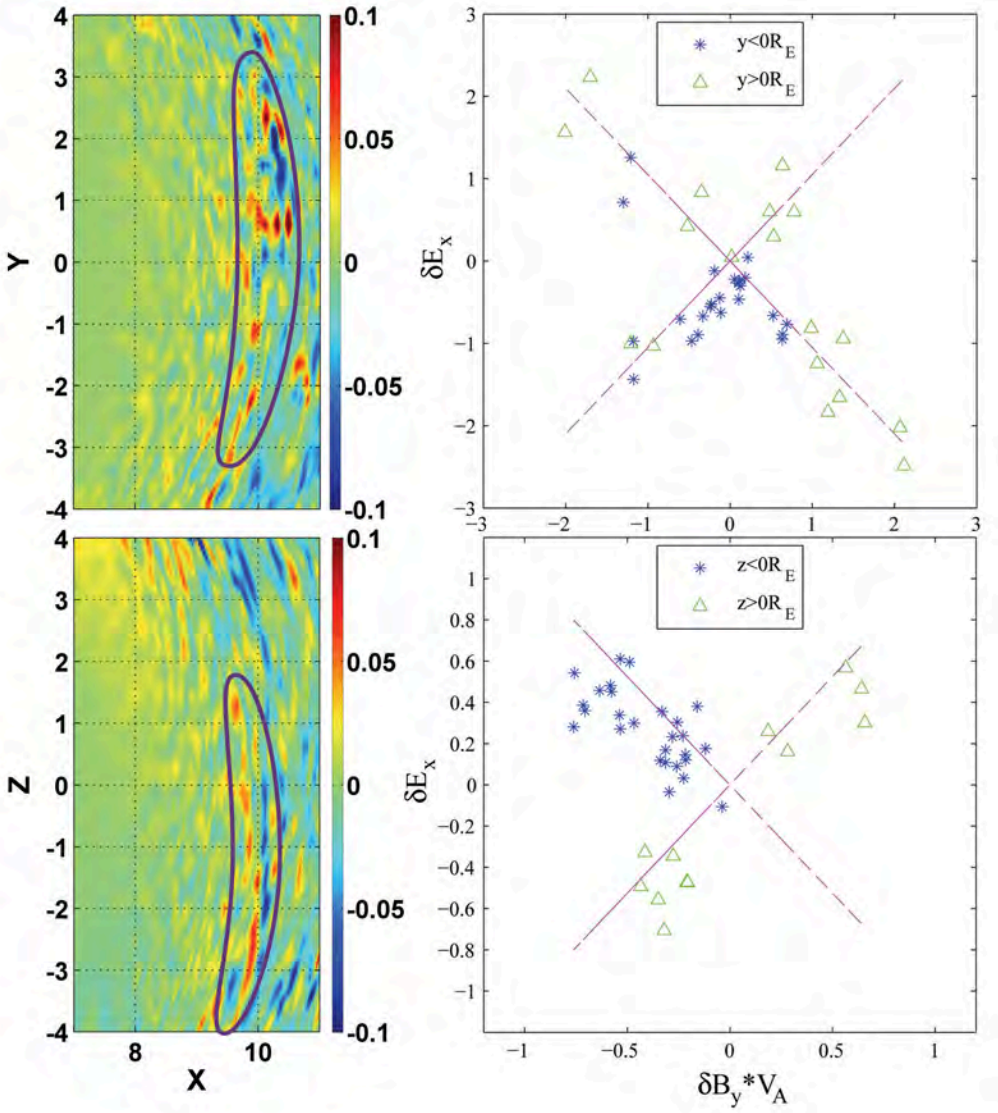

Figure 3.18: Top left: Spatial profile of $E_{\parallel}$ around the MPBL in the equatorial plane at $t = 89$, with $M_A = 3$. Top right: Corresponding polarization relation in the circled regions on the top left showing Alfvén modes propagating in different directions along the field lines. Bottom left: Spatial profile of $E_{\parallel}$ around the MPBL in the noon-meridian plane at $t = 89$, with $M_A = 3$. Bottom right: Corresponding polarization relation in the circled regions on the bottom left showing Alfvén modes. The violet dashed lines on left panels represent the theoretically predicted polarization relation $\delta E_x = \pm 1.1 V_A \delta B_y$ for the KAWs.

1. The wave structure, propagation, and time evolution in the 3-D magnetopause are presented. As the self-generated compressional wave structures propagate from the foreshock toward and impinge on the MPBL, strong $E_{\parallel}$ are excited during their interaction with the MPBL, together with the presence of correlated transverse perturbations in B_y, V_{iy}, and $J_{\parallel}$. These structures, with $k_{\perp}\rho_i \sim k_x\rho_i \sim 0.5$ - 1, are found to be KAWs due to the mode conversion process. The evolution of the KAWs leads to the generation of KAWs dominated by the azimuthal wave numbers k_y, consistent with the previous 3-D hybrid simulation of [7] for mode conversion in a slab geometry of the MPBL.

2. The Alfvén mode test shows that the KAW structures satisfy the Alfvén wave polarization conditions. A spectral analysis for the wave modes dominated by k_y reveals that the dependence of transverse wave polarization of $E_y\left(k_y\right)/B_x\left(k_y\right)$ on the perpendicular wave number k_y is in agreement with the theoretical results for KAWs. The wave spectra of the strongly enhanced $E_{\parallel}$ for these modes also agree with those predicted by theories and previous simulations.

3. These KAW perturbations propagate poleward into the cusps along the MPBL, carrying the electromagnetic energy along field lines. Due to the differential flow convection speeds at various latitudes, the KAW packets expand along the north-south direction and may thus be weakened, while they may also merge with newly formed KAWs due to newly arrived compressional waves.

4. The mode conversion occurs in the MPBL due to the drastic increase of the local Alfvén speed V_A earthward. As the compressional waves approach the MPBL, the Alfvén resonance condition $\omega \simeq k_{\parallel}V_A$ is found to be satisfied at the increased V_A. The resulting KAWs are found to decay into the magnetosphere. The 3-D structures of correlated $E_{\parallel}$ and B_y are presented, indicating the spatial scales of KAWs from mode conversion process.

5. The power spectrum analyses of transverse and compressional components of the magnetic field reveal that the magnetosheath is abundant with compressional waves, while

enhanced transverse waves appear around the MPBL region due to the mode conversion process.

6. The mode conversion is examined for the case of radial IMF with subcritical Mach number ($M_A = 3$). Although the $J_\parallel$ and $E_\parallel$ are weaker, the k_y modes and even k_x modes of KAW are excited in the MPBL significantly, associated with "switch-on" bow shock. Because the MPBL itself becomes broader and oscillatorily more slower, and because the waves downstream from the shock ramp are not monotonic and propagate onto the magnetopause, a much more broader mode conversion region inside the MPBL has been observed.

Chapter 4

Mode Conversion Processes associated with Parallel Shocks

Controlled by IMF B_y and B_z Components at the Magnetopause

4.1 Introduction

In the previous chapter, we have seen the identifications of the basic characteristics of KAWs due to the mode conversion process at the magnetopause associated with a pure quasi-parallel shock without B_y and B_z component. Realistically in the geospace for the quasi-parallel case, however, IMF usually has B_y and B_z component "shifting" the quasi-parallel region and thus modifies the mode conversion process around the MPBL. To study the more realistic nature of mode conversion and see how the B_y and B_z component in IMF controls this process, in this chapter I will perform an analysis of the cases in detail with B_y and B_z component in IMF. How such components in IMF influence on the mode conversion, therefore, as well as the 3-D evolutions especially around the subsolar region, is thus the main focus of this chapter. In this chapter, first I will present the results of case 1 with $B_y = -0.5B_0$ and $B_x = -0.866B_0$ without B_z in IMF, i.e. azimuthal angle $\phi_B = -120°$ and pitch angle $\theta_B = 90°$ in IMF. Then I will show the results of case 2 with $\phi_B = -120°$ and $\theta_B = 70°$ in IMF, i.e. $B_x = -0.470B_0$, $B_y = -0.814B_0$ and $B_z = 0.342B_0$, to conclude this chapter. The case description is listed in Table 4.1.

Case Description	θ	ϕ	B_x	B_y	B_z
Case 1	90°	−120°	-0.866 B_0	-0.5 B_0	0
Case 2	70°	−120°	-0.470 B_0	-0.814 B_0	0.342 B_0

Table 4.1: Brief case description in Chapter 4

4.2 Simulation Results with Case 1 in IMF

4.2.1 Overall Structure

The spatial contours of the magnetic field B with typical geo-space field lines and ion density N at $t = 120$ obtained in case 1 with IMF $B_z = 0$, in the noon meridian and equatorial planes, are shown in Figure 4.1. As expected, the self-generated bow shock and the magnetopause can be recognized around $12R_E$ and $10R_E$, respectively, in the subsolar regions of both B and N contours. Both the bow shock and the magnetopause, however, appear to be "compressed" more seriously around $y = 2 \sim 6R_E$ rather than the subsolar region in this case with B_y component compared with that of no B_y component in previous chapter. This is because in the existence of negative (positive) B_y component in IMF, the quasi-parallel shock regions are "shifted" to the dusk (dawn) side on the bow shock, so that the backstreaming ions can be easily transported away from these regions due to the ion beam instabilities [36]. Thus, it is a natural consequence to see that the magnetosheath around these regions is a lot thinner than other regions. In addition, many of the foreshock waves, as well as the compressional pulses generated around these regions, due to the turbulence in the bow shock [36], are carried downstream (earthward) by the convective plasma flows into the magnetosheath, as can be perceived in Figure 4.1.

This non-symmetric profiles of magnetosheath in B and N can also be distinctively seen from the view of the sun to the earth, as shown in Figure 4.2. For the comparison purpose, the top panel of B and N contours in Figure 4.2 shows the non-symmetric profiles due to the "shifted" quasi-parallel shock regions in the $y - z$ plane cut view locating at $x = 10R_E$ under the influence of B_y component in IMF, while the bottom panel presents the symmetric profiles in the same $y - z$ plane cut view without B_y component in IMF.

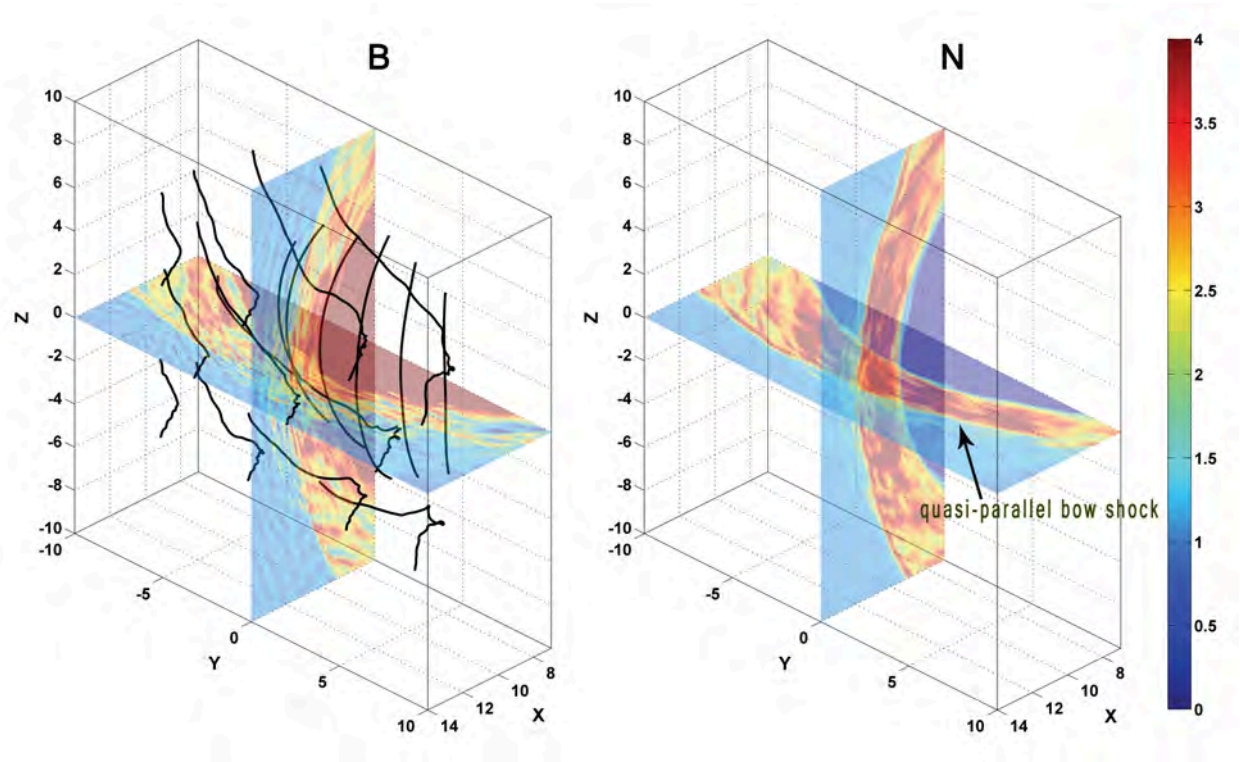

Figure 4.1: Spatial contours of the magnetic field B and ion density N at $t = 120$ showing the 3-D structures of self-consistently generated bow shock and magnetopause, as well as the compressive pulses in the magnetosheath. Typical field lines are also shown in the magnetic field plot.

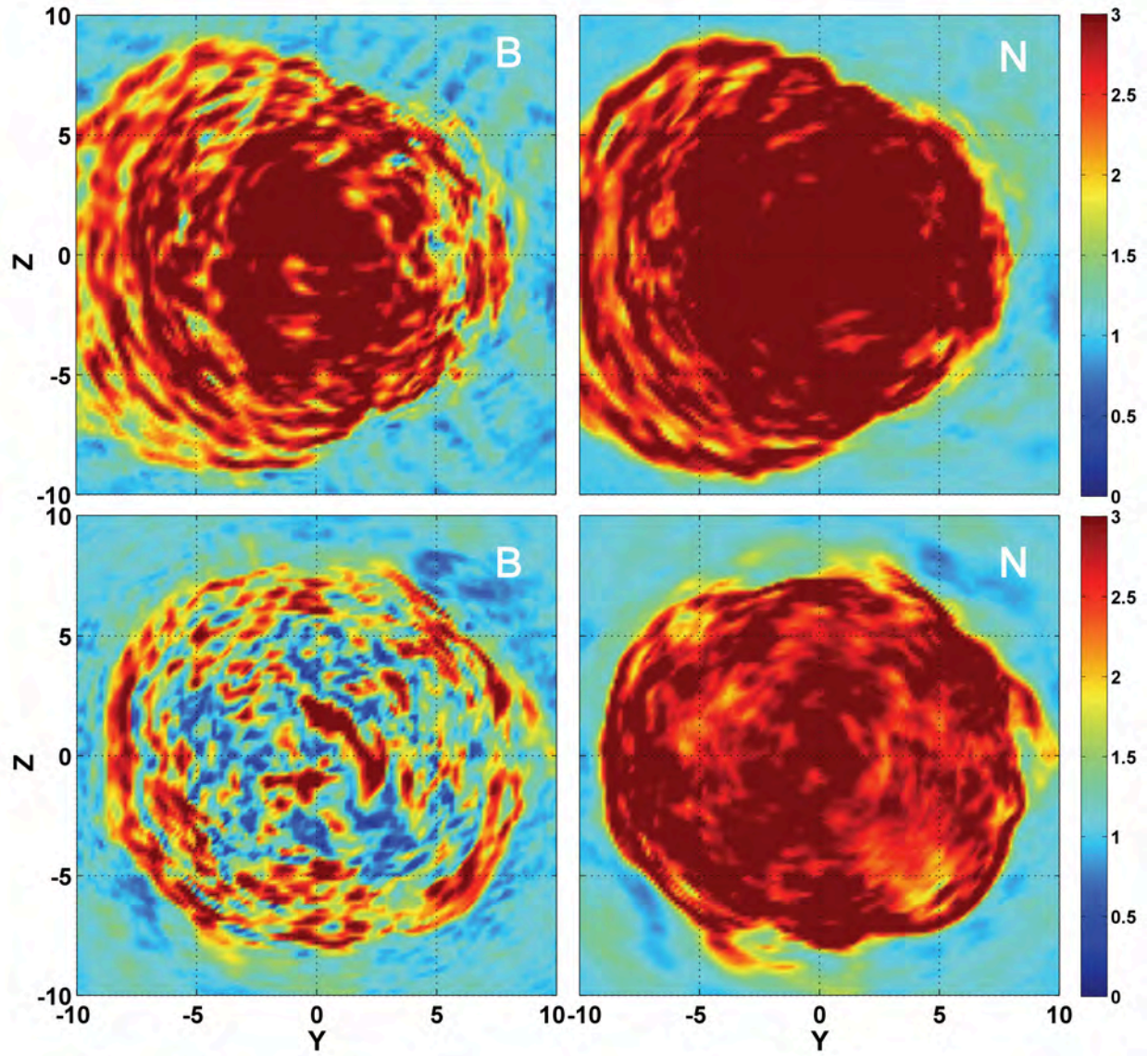

Figure 4.2: The comparison of spatial contours of the magnetic field B and ion density N at $t = 110$, presenting the non-symmetric magnetosheath profiles from Sun-Earth view of the $y - z$ plane at $x = 10R_E$ under the influence of B_y component in IMF (in the top panel), and the symmetric profiles without B_y component in IMF (in the bottom panel).

4.2.2 the Mode Conversion and Generation of KAWs

To see the dynamical propagation of the compressive wave structures, the spatial profiles of various quantities parallel to the Sun-Earth line are drawn in Figure 4.3 in a time sequence of $t = 50$ - 170. From Figure 4.3 we see that the incoming fast-mode compressive wave pulses characterized by the perturbations in B and N repeatedly propagate onto the magnetopause from the bow shock region along the Sun-Earth line. Moreover, along the Sun-Earth line, the magnetopause can be distinguished around $9.8R_E$ from the abrupt increase in B and decrease in N earthward (i.e. in $-x$ direction as before), and the bow shock is located roughly around $11.9R_E$. A typical case of these earthward propagating compressive waves can be described as seen from Figure 4.3 at $t = 100$ when a new packet of wave pulses are generated at the bow shock and carried by the convective solar wind plasma earthward to the MPBL at about $t = 120$. In this case, the typical Alfvén speed is about $1.7V_{A0}$ in the magnetosheath outside the MPBL around $11R_E$, where the compressive waves propagate sunward with a speed about 2 - $3V_{A0}$ in the frame of convective plasma. And since the total convective plasma flow speed is about 2 - $3V_{A0}$, the net propagation speed of 2 - $3V_{A0}$ in the Earth frame of reference is seen. This is pretty similar to the case previously shown in Chapter 3, i.e. without B_y component in IMF, near the Earth's subsolar region. While approaching the magnetopause, the compressional wave pulses are slowing down significantly in x-direction, and consequently impinging onto the magnetopause. In this context, however, the mode conversion process is different from the case without B_y component since the quasi-parallel region is no longer around the subsolar point. Although the azimuthal convective flow speeds are more or less the same between the cases, the wave structures can be readily off the Sun-Earth line/plane due to the existence of B_y component locally in B_y case, so that the interaction time between them and the magnetopause could be dramatically reduced even in the circumstances that the local convective flows are quite similar. Therefore, it can be found that the $E_\parallel$, which is one of the characteristics of KAWs shown in the previous chapter, has much weaker intensity in this case.

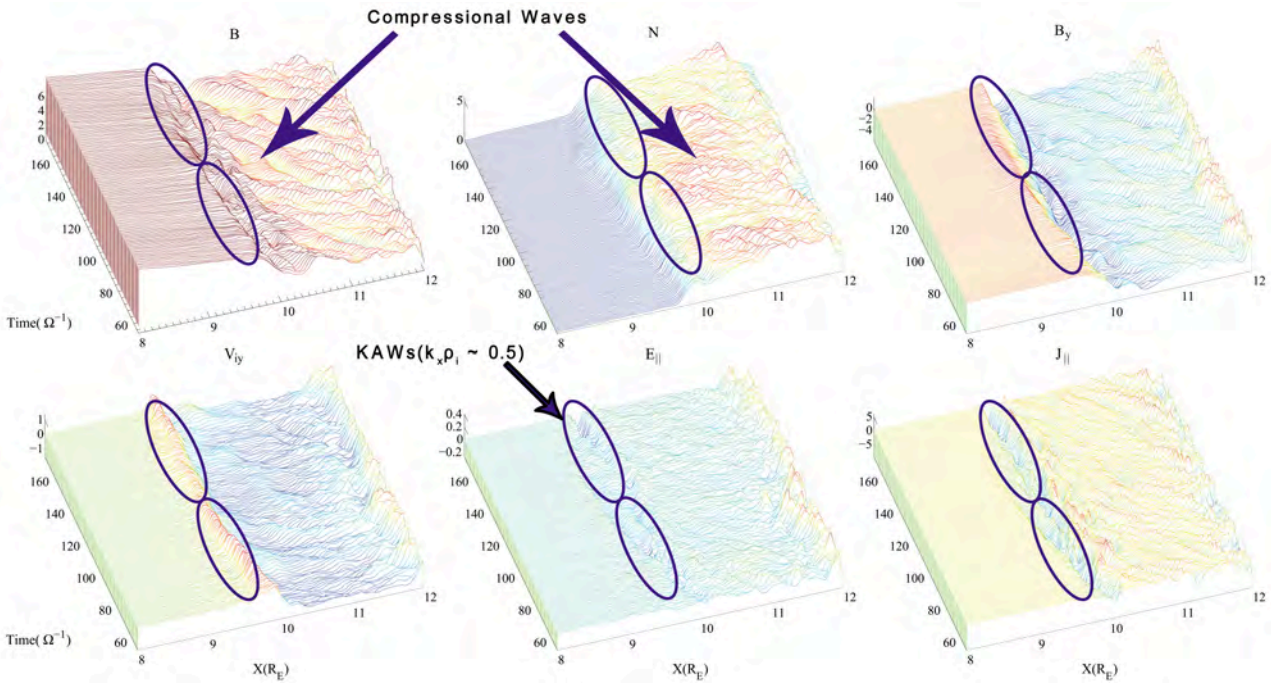

Figure 4.3: Time evolution of spatial profiles of various quantities, along the Sun-Earth line, during the time interval t = 50 - 170. The circles highlight areas with locally excited $E_{||}$ around the MPBL, which have been proved the KAW structures in the previous chapter.

After the wave pulses impact on the MPBL, perturbations in $E_{\parallel}$ are also excited around the transition layer and can be seen in Figure 4.3, from $t \simeq 60$ - 100 to $t \simeq 110$ - 150, as marked in the two circles. The locally excited wave structures are examined predominantly to be of short wave lengths $k_x \rho_i \simeq 0.5$ - 1 similar to the previous cases.

Figure 4.4 shows the spatial contours of B_x, B_y, B, N, V_{ix}, V_{iy}, V_{iz}, and $J_{\parallel}$ in the equatorial plane at $t = 110$. The magnetopause and bow shock are marked on the contours of B and N. Short wave length structures carried earthward by the convective plasma are seen in the magnetosheath, especially around the downstream of the quasi-parallel bow shock, $y \sim 4R_E$. The dynamical propagation of the compressive wave structures, the spatial profiles of various quantities parallel to the Sun-Earth line are drawn in Figure 4.5 in a time sequence of $t = 50$ - 170. Besides, quite similar to the processes in Figure 4.3, the incoming fast-mode compressive wave pulses repeatedly propagate onto the magnetopause from the quasi-parallel bow shock region along the line $(x, 4.0, 0.0)R_E$, and the strong $E_{\parallel}$ was excited locally with the advent of these incoming compressive pulses.

To see the change of polarization of the wave pulses from the bow shock/magnetosheath region to the MPBL, the time variations of B and N along the Sun-Eearth line in the equatorial plane at two distinct locations, around the MPBL $x = 9.9R_E$ and near the bow shock region $x = 11.9R_E$, respectively, are shown in Figure 4.6.

As described in previous chapter, when B is high and N is low, the location $x = 9.9R_E$ is on the magnetospheric side in MPBL; when B is low and N is high, the location $x = 9.9R_E$ is on the magnetosheath side. From Figure 4.6, we can see that during the time $90 \lesssim t \lesssim 160$, this location is swept through repeatedly by the oscillating magnetopause. In this case, it can also be concluded that the MPBL is dominated by the anti-phase relation of B and N, while the magnetosheath region is predominant by the in-phase relation. That is, the change of the wave polarizations still occurs in the existence of B_y component in IMF. Other features are similar to the case without B_y component in IMF discussed in the previous chapter.

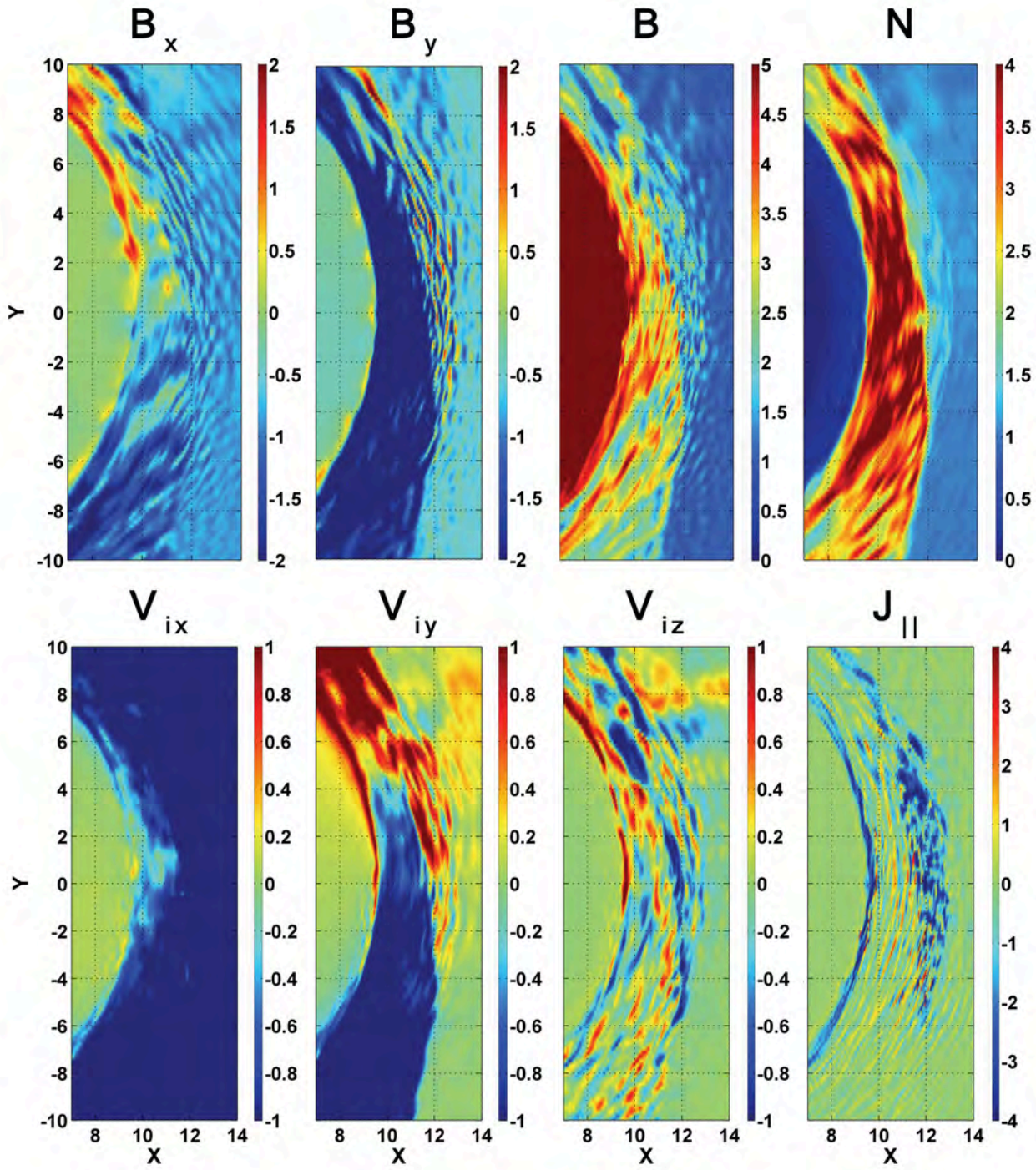

Figure 4.4: Contours of various quantities in the equatorial plane at $t = 110$.

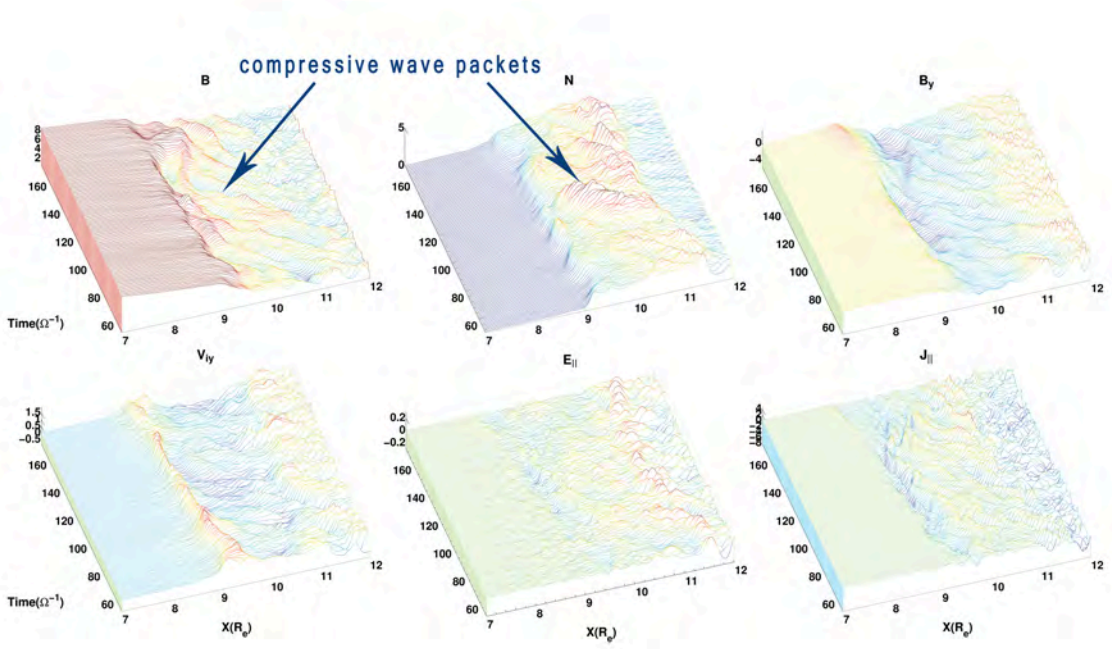

Figure 4.5: Time evolution of spatial profiles of various quantities, along $(x, 4.0, 0.0)R_E$ parallel to the Sun-Earth line, during the time interval $t = 50$ - 170.

With B_y component, the parallel wavelength of incoming waves on the magnetopause in our simulations is measured approximately to be 3 - $8R_E$, with $\rho_i \sim 0.5d_{i0}$ locally, and the perpendicular wavelength to be roughly 0.2 - $0.5R_E$. Around the subsolar region in the MPBL, figure 4.7 shows the spatial profiles of physical quantities and similar to the existence of the predicted Alfvén resonance surface, where $E_{\parallel}$ is strongly excited locally, purely decayed into the magnetosphere, and simply damped to the magnetosheath, consistent with theoretical results [6] as shown in Figure 1.9, so do the $J_{\parallel}$ as in the previous chapter. Besides, the $E_{\parallel}$ and $J_{\parallel}$ are still locally excited and well correlated. In short, these structures are still KAWs identified as in the previous chapter.

The wave polarization relation is similar to what has been given in the previous chapter, $\delta E'_x \simeq \sqrt{1 + k_\perp^2 \rho_i^2} V_A \delta B'_y \simeq 1.1 V_A \delta B'_y$, where $\delta E'_x$ and $\delta B'_y$ are perpendicular to the magnetopause boundary normal, since the relation $k_\perp \rho_i \sim 0.5$ - 1 and $T_e/T_i \sim 0.1$ - 0.2 still hold

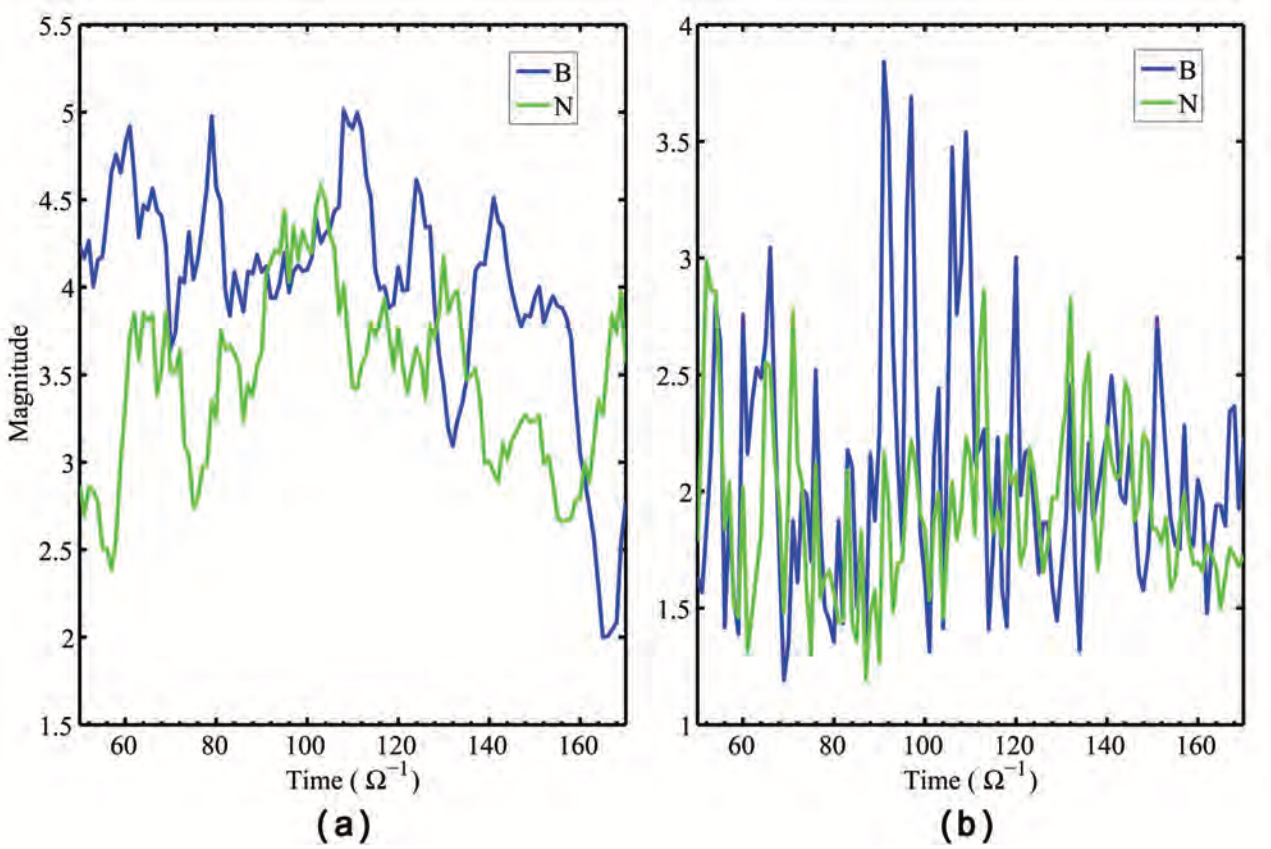

Figure 4.6: Time variations of B and N at two locations $x = 9.9R_E$ and $x = 11.9R_E$ along the Sun-Earth line in the equatorial plane: (a) anti-phase relation at $x = 9.9R_E$ in the MPBL, and (b) predominantly in-phase relation at $x = 11.9R_E$ in the magnetosheath.

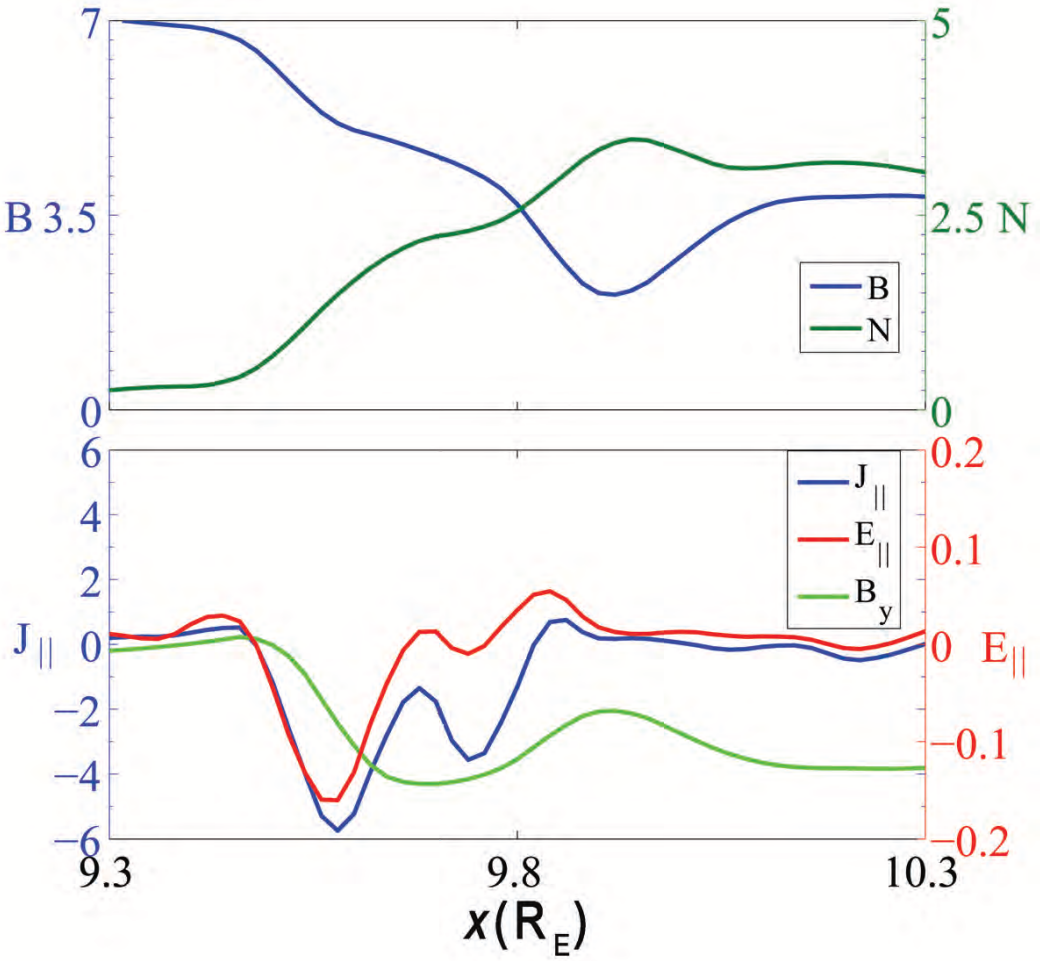

Figure 4.7: Spatial cuts of various quantities through the MPBL along the Sun-Earth line at $t = 170$.

here. Figure 4.8 shows the wave polarization relation, at $t = 170$, which is also nearly consistent with the theoretical lines in the circled region. The polarization properties are pretty similar to the ones shown in the previous chapter. At $t = 170$, around subsolar region at the magnetopause, it can be distinguished that two wave branches propagate northward and southward, respectively, separated around the equatorial plane. While at the same time, the strongly enhanced $E_{\parallel}$ in the equatorial plane simply shows a southward wave propagation branch. In this particular case, $k_y\rho_i \sim 0.5$ - 1 appears in the wave structures in the MPBL.

Since the propagation of shear Alfvén waves in the inner magnetosphere can result in the field line resonance [79], it is expected to see such at radial distances away from the magnetopause boundary [36]. Figure 4.9 shows time sequence of the dominant azimuthal (longitudinal) magnetic field component ($B_y \sim B_\phi$) at two meridian planes, which are located at $\phi = 30^\circ$ near the quasi-parallel (Q-$\parallel$) shock region and $\phi = -30^\circ$ near the quasi-perpendicular (Q-$\perp$) shock region, respectively, along the field lines through the equatorial radius of $L = 7.5R_E$ as a function of S, where S is the distance along the field line with the starting point $S = 0$ ($S = 12R_E$) approximately at the $r = 4R_E$ boundary in the north (south). The vertical axis of each plot represents the scale of the corresponding time sequence from $t = 40$ to $t = 120$ while the relative amplitude of the perturbations in all times of the sequences is scaled the same correspondingly. Note that the selected field line (flux tube) is only approximately the same line at different times, whereas the magnetic field in the magnetosphere would experience low frequency oscillations as a result of foreshock oscillations. The transverse distortion of magnetic field in B_ϕ (approximately B_y in this context), as a response to the compressional waves, is present and bounces between the north and the south boundaries in both Q-$\parallel$ and Q-$\perp$ region. Figure 4.9 shows that the amplitude of these oscillations at $\phi = 30^\circ$ is larger than those at $\phi = -30^\circ$; that is, the field line oscillations in the Q-$\parallel$ are more intense than those in the Q-$\perp$.

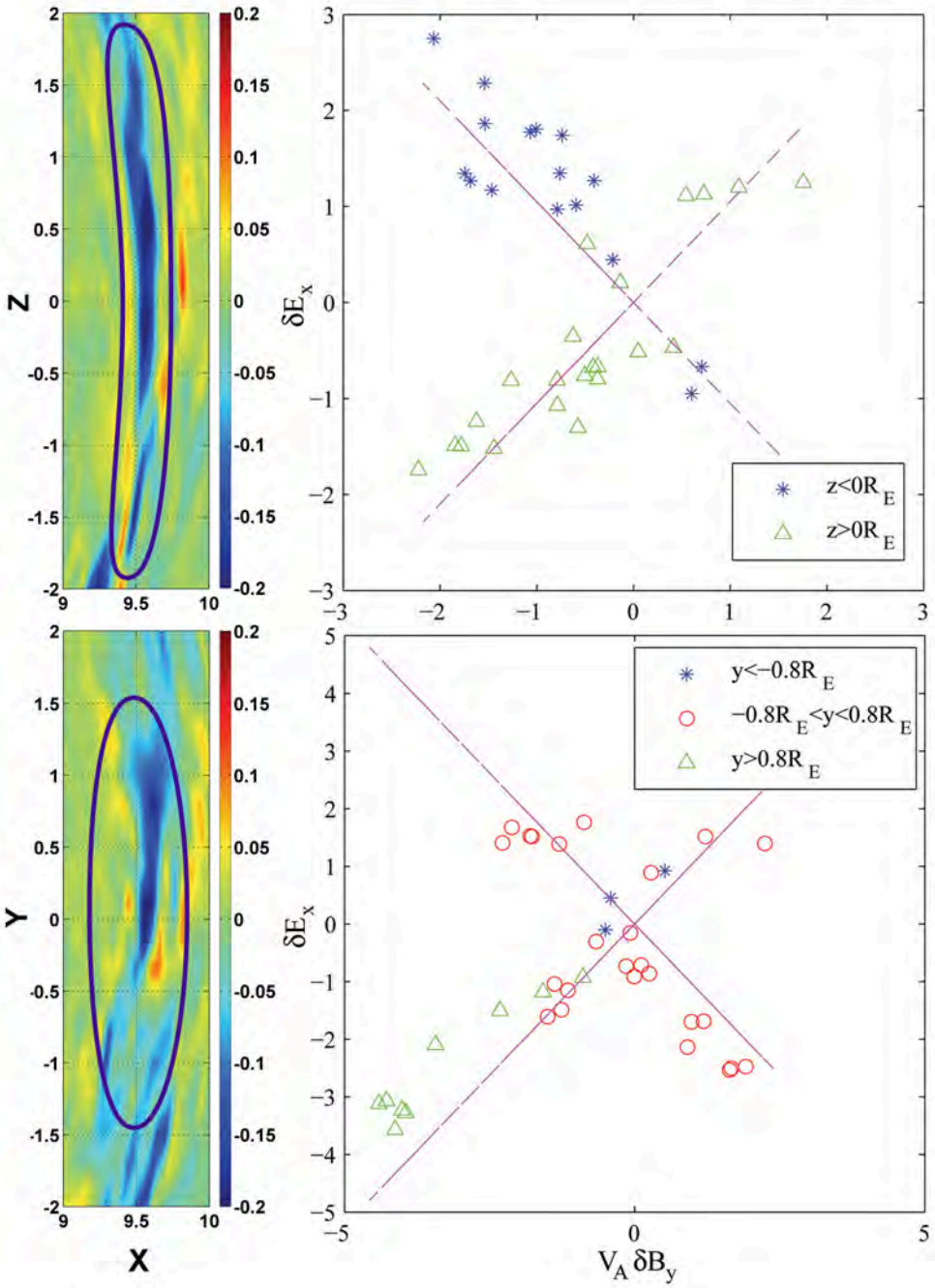

Figure 4.8: Top left: Spatial profile of $E_{\parallel}$ around the MPBL in the noon-meridian plane at $t = 130$. Top right: Corresponding polarization relation in the circled regions on the top left showing Alfvén modes propagating in different directions along the field lines. Bottom left: Spatial profile of $E_{\parallel}$ around the MPBL in the equatorial plane at $t = 130$; Bottom right: Corresponding polarization relation in the circled regions on the bottom left showing Alfvén modes. The violet dashed lines on left panels represent the theoretically predicted polarization relation $\delta E_x = \pm 1.1 V_A \delta B_y$ for the KAWs.

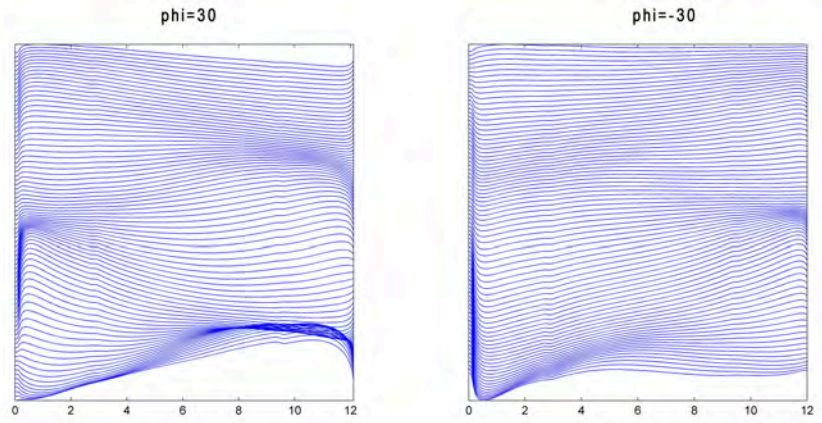

Figure 4.9: Time sequence of the longitudinal magnetic field component B_y along the field lines at $L = 7.5$ in the meridian plane at $\phi = 30°$ (right) and $\phi = -30°$ (left) as a function of S, where S is the distance along the field line from north to south. The vertical axes representing time sequence are from $t = 40$ to $t = 120$. In these meridian planes, B_y is dominant so that $B_y \sim B_\phi$.

4.2.3 Global Distribution and Propagation of the Alfvén waves

To see the longitudinal and latitudinal global structures associated with the mode conversion in the existence of B_y component in IMF, the poleward and duskward movement of KAWs originating from the subsolar region due to the mode conversion is tracked and presented in Figure 4.10 with twelve snapshots from $t = 100$ to $t = 155$. The subsolar region is abundant of compressional drivers in front of the magnetopause. As a result, KAWs continuously form in the subsolar area, downstream of the quasi-parallel shock. They are seen to propagate not only along the field lines down to the cusp region, but also carried away by the convective flow much more quickly than the previous case without B_y component shown in Chapter 3. At $t = 100$, a group of KAW structures are excited near the subsolar region around the MPBL. As time evolves, they are carried away from the subsolar region with the convective speed of about 0.3 - $0.4V_A$, and because the KAWs also propagate along the field lines poleward, we see a much broader expansion poleward than tailward. In addition,

the poleward propagation speed is about V_A, consistent with the prediction of Alfvén waves. Note that in these snapshots the northward propagation is especially emphasized with the circled region. It should also be pointed out that, for this single wave packet, it seems much stronger in the northern hemisphere than in the south at $t = 150$ and $t = 155$, because there are newly formed and stronger KAWs in the north part, and thus merged with the tailward KAWs assuming stronger than that in the south. On average, however, the KAW structures tend to be symmetric in both northern and southern hemispheres. During such time interval (i.e. $\Delta t \sim 5$), about 1 - 2 incoming pulses arrive at the MPBL.

4.3 Simulation Results with Case 2

4.3.1 Overall Structure

For case 2, with all non-zero components in IMF, the spatial contours of the magnetic field B with typical geo-space field lines and ion density N at $t = 90$, in the noon meridian and $y = -3R_E$ planes, are shown in Figure 4.11. As expected, the self-generated bow shock and the magnetopause can be recognized around $13R_E$ and $10R_E$ in the subsolar regions, respectively. In the existence of positive B_z component in IMF, the quasi-parallel shock regions are "shifted" to the south side on the bow shock, i.e. Q-$\parallel$ on the dusk and south side for case 2, where the backstreaming ions can be easily transported away from these regions due to the ion beam instabilities [36].

The non-symmetric profiles of magnetosheath in B and N can also be seen from the view of the sun to the earth, as shown in Figure 4.12. From this figure, we can clearly see the "shift" of the magnetopause profile in B as discussed previously.

Figure 4.13 shows the spatial contours of B_x, B_y, B, N, V_{ix}, V_{iy}, V_{iz}, and $J_\parallel$ in the equatorial plane at $t = 90$. The magnetopause and bow shock are marked on the contours of B and N. Short wave length structures carried earthward by the convective plasma are seen in the magnetosheath, especially around the downstream of the quasi-parallel bow shock, $y \sim 4R_E$ and $z \sim -2R_E$.

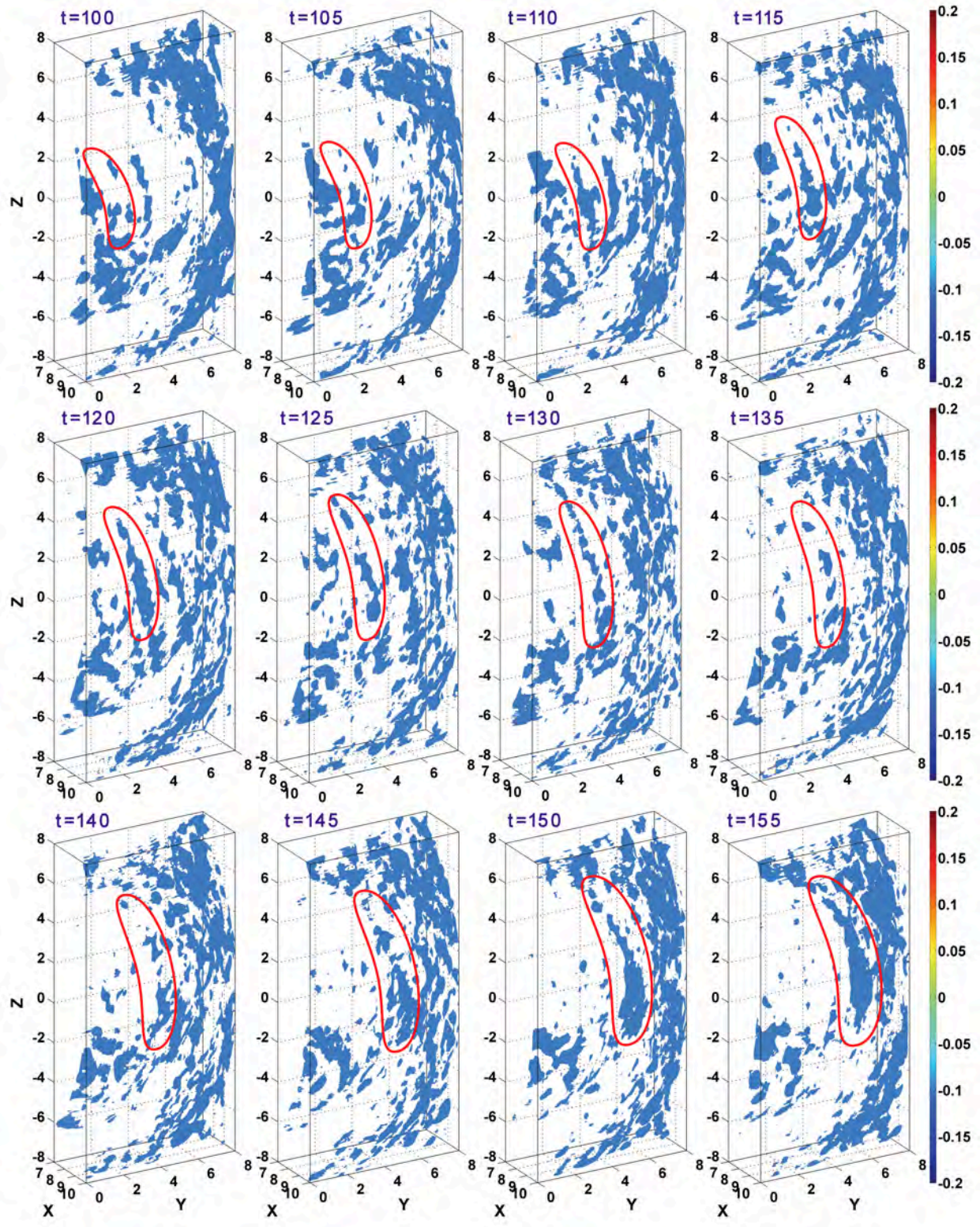

Figure 4.10: Isosurface plot of $E_{\parallel}$ with tracked circles showing the same KAW structure generated near the subsolar region from $t = 100$ to $t = 155$ for case 1 in Table 4.1.

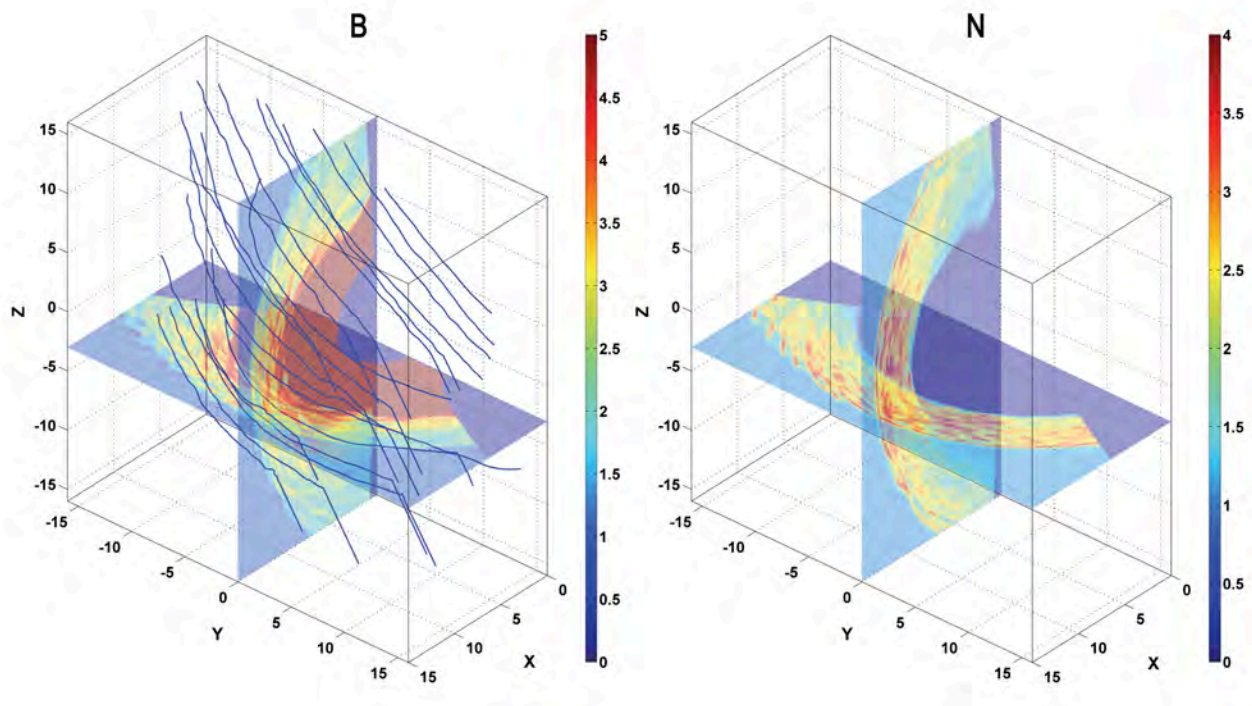

Figure 4.11: Spatial contours of the magnetic field B and ion density N at $t = 90$ showing the 3-D structures of self-consistently generated bow shock and magnetopause, as well as the compressive pulses in the magnetosheath. Typical field lines are also shown in the magnetic field plot. The Q-$\parallel$ region is now located at the dusk and south side.

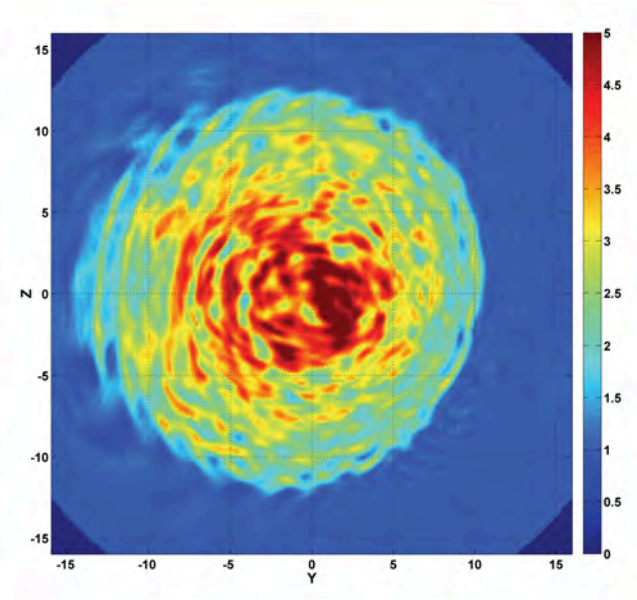

Figure 4.12: The comparison of spatial contours of the magnetic field B at $t = 90$, presenting the non-symmetric magnetosheath profiles from Sun-Earth view of the $y - z$ plane at $x = 10R_E$ under the influence of B_z and B_y component in IMF.

4.3.2 Mode Conversion and Propagation of KAWs

The spatial profiles of various quantities parallel to the Sun-Earth line are drawn in Figure 4.14 in a time sequence of $t = 40$ - 95. From Figure 4.14 we see that the incoming fast-mode compressive wave pulses repeatedly propagate onto the magnetopause from the bow shock region along the Sun-Earth line. Moreover, along the Sun-Earth line, the magnetopause can be distinguished around $10R_E$, and the bow shock is located roughly around $13R_E$, inconsistent with the expectation of thicker magnetosheath in the existence of B_z in IMF. After the wave pulses impact on the MPBL, perturbations in $E_{\parallel}$ are also excited around the transition layer and can be seen in Figure 4.14. The locally excited wave structures are examined predominantly to be of short wave lengths $k_x\rho_i \simeq 0.5$ - 1 similar to the previous cases.

The change of polarization of the wave pulses from the bow shock/magnetosheath region to the MPBL along the sun-earth line can be seen from Figure 4.15, the time variations of B and N along the Sun-Eearth line in the equatorial plane at two distinct locations, around

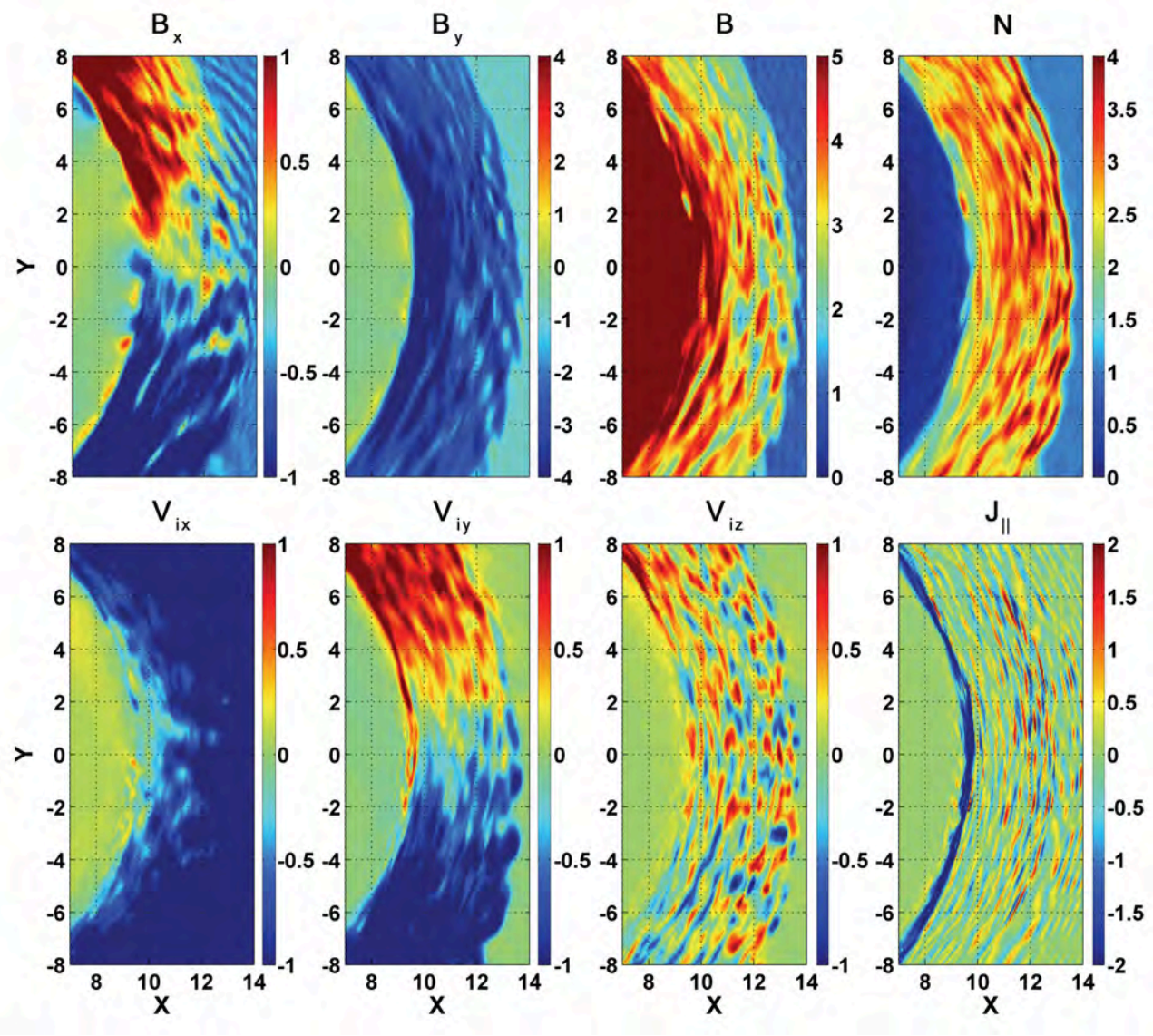

Figure 4.13: Contours of various quantities in the equatorial plane at $t = 90$.

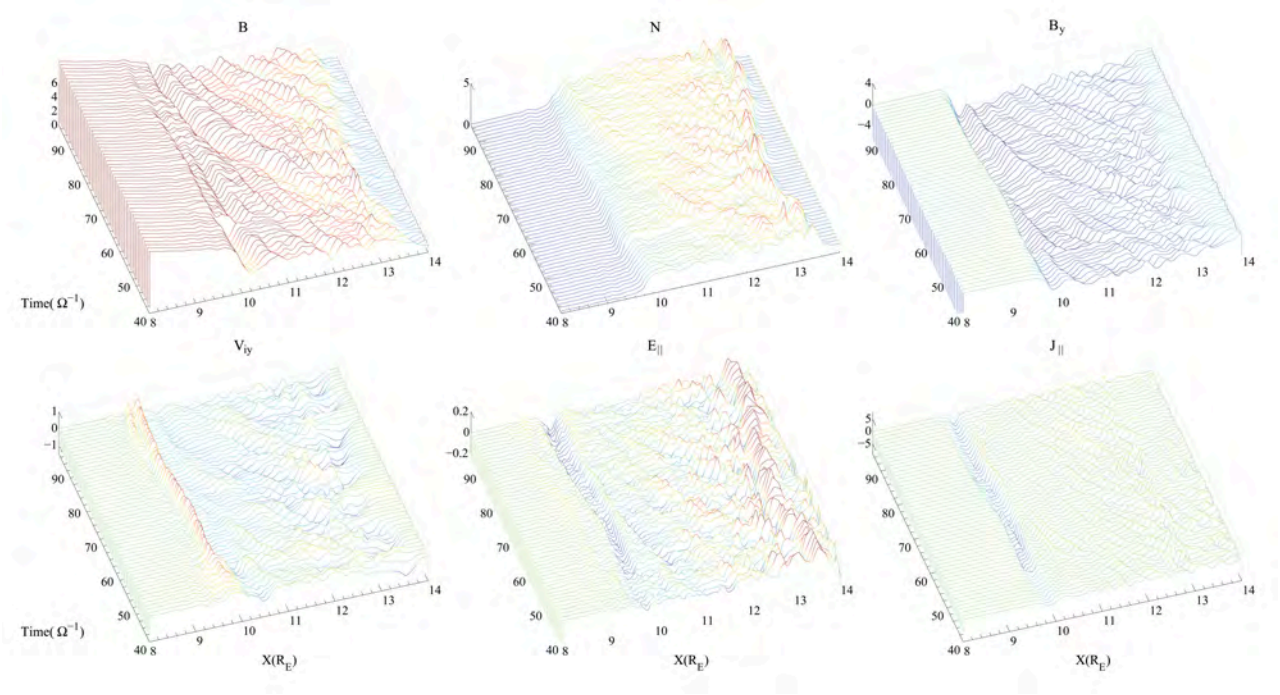

Figure 4.14: Time evolution of spatial profiles of various quantities, along the Sun-Earth line, during the time interval $t = 40$ - 95.

the MPBL $x = 10.5R_E$ and near the bow shock region $x = 13R_E$, respectively. In this case, it can also be concluded that the MPBL is dominated by the anti-phase relation of B and N, while the magnetosheath region is predominant by the in-phase relation. That is, the change of the wave polarizations still occurs in the existence of B_z and B_y component in IMF. Other features are similar to the case without these components in IMF discussed in the previous chapter.

In the existence of B_z and B_y components, the parallel wavelength of incoming waves on the magnetopause in our simulations is measured approximately to be 3 - $8R_E$, with $\rho_i \sim 0.5d_{i0}$ locally, and the perpendicular wavelength $\sim$ 0.2 - $0.5R_E$, quite the same in previous cases. Figure 4.16 shows the Alfvén resonance surface around the subsolar region in the MPBL. Although B_z and B_y is dominant in the magnetosheath side, the $E_{||}$ and $J_{||}$ are still locally excited and well correlated. In short, these structures are still KAWs identified as in the previous chapter.

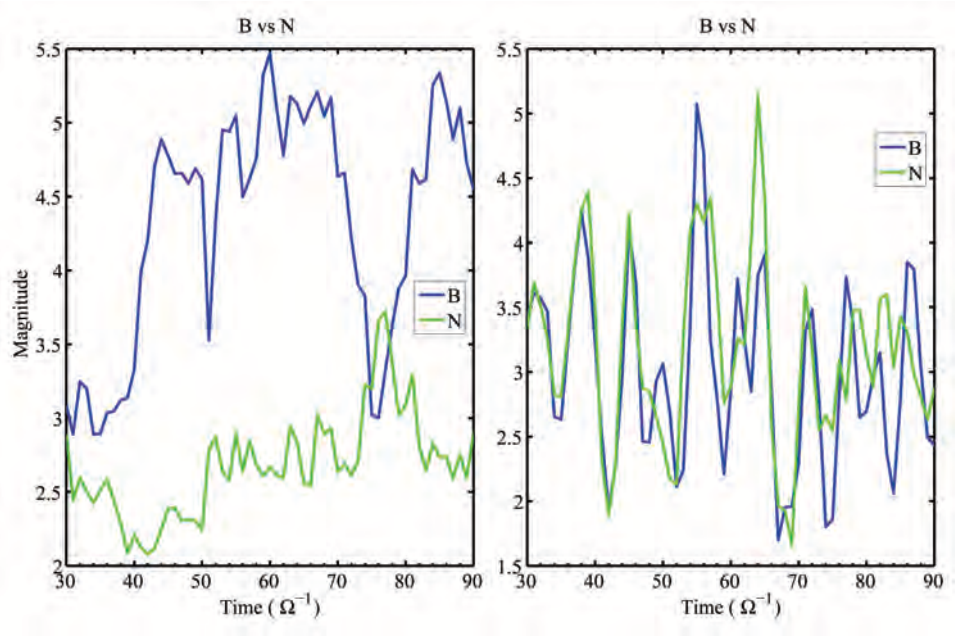

Figure 4.15: Time variations of B and N at two locations $x = 10.5R_E$ and $x = 13R_E$ along the Sun-Earth line in the equatorial plane: (a) anti-phase relation at $x = 10.5R_E$ in the MPBL, and (b) predominantly in-phase relation at $x = 13R_E$ in the magnetosheath.

To see the longitudinal and latitudinal global structures associated with the mode conversion in the existence of B_y component in IMF, the poleward and duskward movement of KAWs originating from the subsolar region due to the mode conversion is tracked and presented in Figure 4.17 with snapshots from $t = 51$ to $t = 91$. The subsolar region is abundant of compressional drivers in front of the magnetopause. As a result, KAWs continuously form in the subsolar area, downstream of the quasi-parallel shock. They are seen to propagate not only along the field lines down to the cusp region, but also carried away by the convective flow much more quickly than the previous case without B_y component shown in Chapter 3. At $t = 81$, a group of KAW structures are excited near the subsolar region around the MPBL. As time evolves, they are carried away from the subsolar region with the speed of about 0.3 - $0.4V_A$, and because the KAWs also propagate along the field lines poleward, we see a much broader expansion poleward than tailward. In addition, the poleward propagation speed is about V_A, consistent with the prediction of Alfvén waves. Note that in these

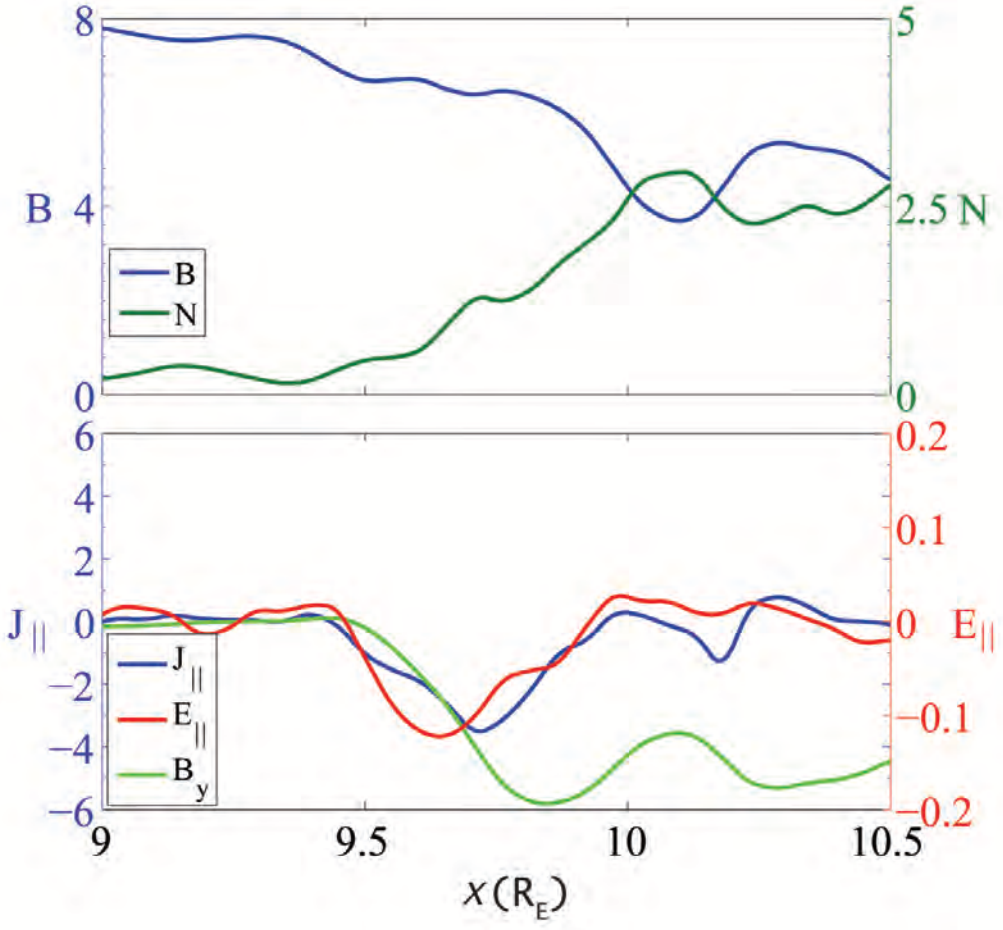

Figure 4.16: Spatial cuts of various quantities through the MPBL along the Sun-Earth line at $t = 90$.

snapshots the northward propagation is especially emphasized with the circled region. It should also be pointed out that it seems much stronger in the northern hemisphere than in the south at $t = 81$ and $t = 91$, because there are newly formed and stronger KAWs in the north part, and thus merged with the tailward KAWs assuming stronger than that in the south.

4.4 Comparison of Simulation Results of Mode Conversion with Satellite Observations

In both hybrid simulations and observations, the change of the wave polarization from compressive modes in the magnetosheath to transverse modes in the MPBL have been observed, and wave power spectra are also consistent, shown in Figure 1.5, 3.4, and 3.5, respectivly. Moreover, at the higher wave number with $k_\perp \rho_i \sim 1$ and $k_\perp \gg k_\parallel$, the waves exhibit similar characteristics of KAW modes, as well as the wave spectrum of $E_{\perp\nu}(k_\perp)/B_{\perp\phi}(k_\perp)$ ($E_y(k_y)/B_y(k_y)$) as a function of $k_\perp$ (k_y) for the azimuthal (k_y) modes, as shown in Figure 1.7 and Figure 3.9. Also as discussed in Section 3.2.4, by comparing the values of the effective parallel electric field associated with the transit time damping $E_{TD} = -\left[m_i v_{i\perp}^2 / \left(2\bar{B}\right)\right] ik_\parallel B_\parallel \left(k_y\right)/e$ and the Landau damping based on the quasilinear theory $E_{LD} = E_\parallel \left(k_y\right)$, the magnitude of the transit time damping in the simulations is roughly 4 - 8 times of that of the Landau damping, consistent with satellite observations [62]. For a typical IMF of $10nT$ and a solar wind density of $5/c.c.$, the wave Poyting flux normal to the magnetopause boundary S_z is $\sim 1.5 \times 10^{-5} W/m^2$ averaged over the wave packet period in the simulations, consistent with the observations of [4] (Figure 1.6). Besides these features, our hybrid simulations are capable of providing more detailed analysis of wave structures, and the Alfvén resonance condition and locally excited $E_\parallel$ at the MPBL are especially examined and proved these KAW modes. Beyond the satellite observations, the propagation of these KAWs due to mode conversion has been studied and presented in Section 3.2.5, 4.2.3 and 4.3.2.

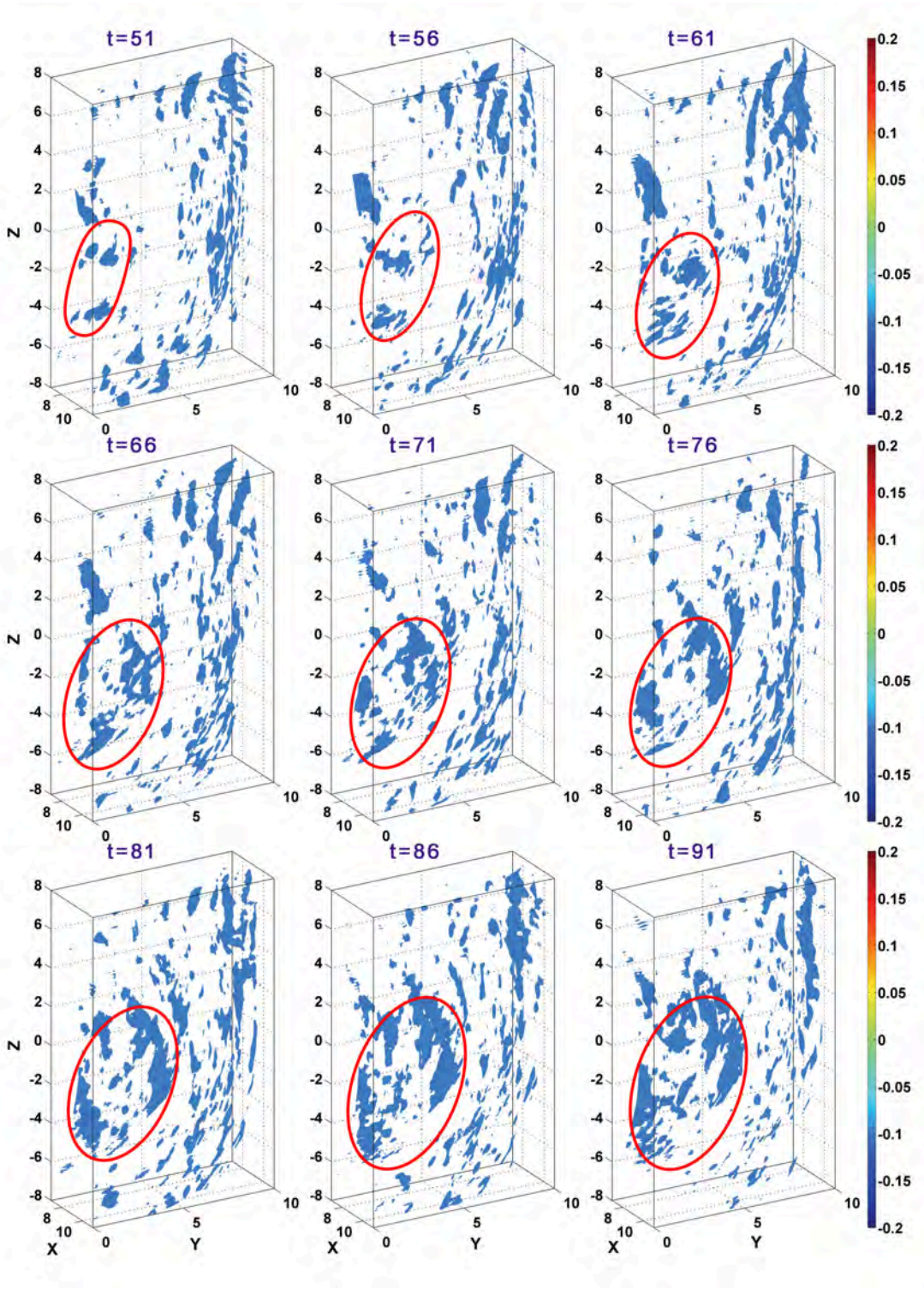

Figure 4.17: Isosurface plot of $E_{\parallel}$ with tracked circles showing the same KAW structure generated near the subsolar region from $t = 51$ to $t = 91$ for case 2 in Table 4.1.

4.5 Comparison of Simulation Results of Field-Aligned Currents with Satellite Observations

Figure 4.18 shows typical field-aligned electric field as well as the field-aligned current density in the equatorial plane, with typical field lines through the strong perturbations in the MPBL from the equatorial plane back into the ionosphere. Also, in the equatorial plane the strong perturbations in $E_{\|}$ indicate the KAWs around the MPBL. The typical magnetic field lines locally in Figure 4.18 are still similar to that of dipole field into the ionosphere, so it may be well seen that these perturbations can be mapped to the inner boundary of the magnetosphere and thus partly can be regarded as ionospheric current density [111]. Note that since the background current round the magnetopause is from dawn to dusk [112], a steadily negative field-aligned current component is observed in Figure 4.18. For $B \simeq 10nT$ and $N \simeq 5c.c.^{-1}$ in the solar wind normalization scale, one has $J_0 \sim 3 \times 10^{-7} A \cdot m^{-2}$. In the previous 2-D model [111], this mapping could be estimated by a factor of $\sqrt{B_M/B_I} \sim \sqrt{(1R_E)^2/(10R_E)^2} = 0.1$, where B_M and B_I are the magnetic field strengths at the magnetopause and the ionosphere, respectively. For the strong perturbations in $E_{\|}$, characterizing the KAWs, on the magnetopause shown in Figure 4.18, a field-aligned current density of $\sim$ 2 - $4J_{\|}$ is seen. Because of the 3-D nature of the geo-magnetic field topology, the B field and the cross-section area of flux tubes vary as r^{-3}. Therefore, in the assumption that nearly 4-6% of the magnetopause currents would be able to propagate into the ionosphere, the field-aligned current density $J_{\|}$ that would penetrate the magnetosphere into the ionosphere is of the order of $10^{-6} A \cdot m^{-2}$, consistent with previous 2-D estimation [111] and observations [113, 114, 115, 116, 117, 118].

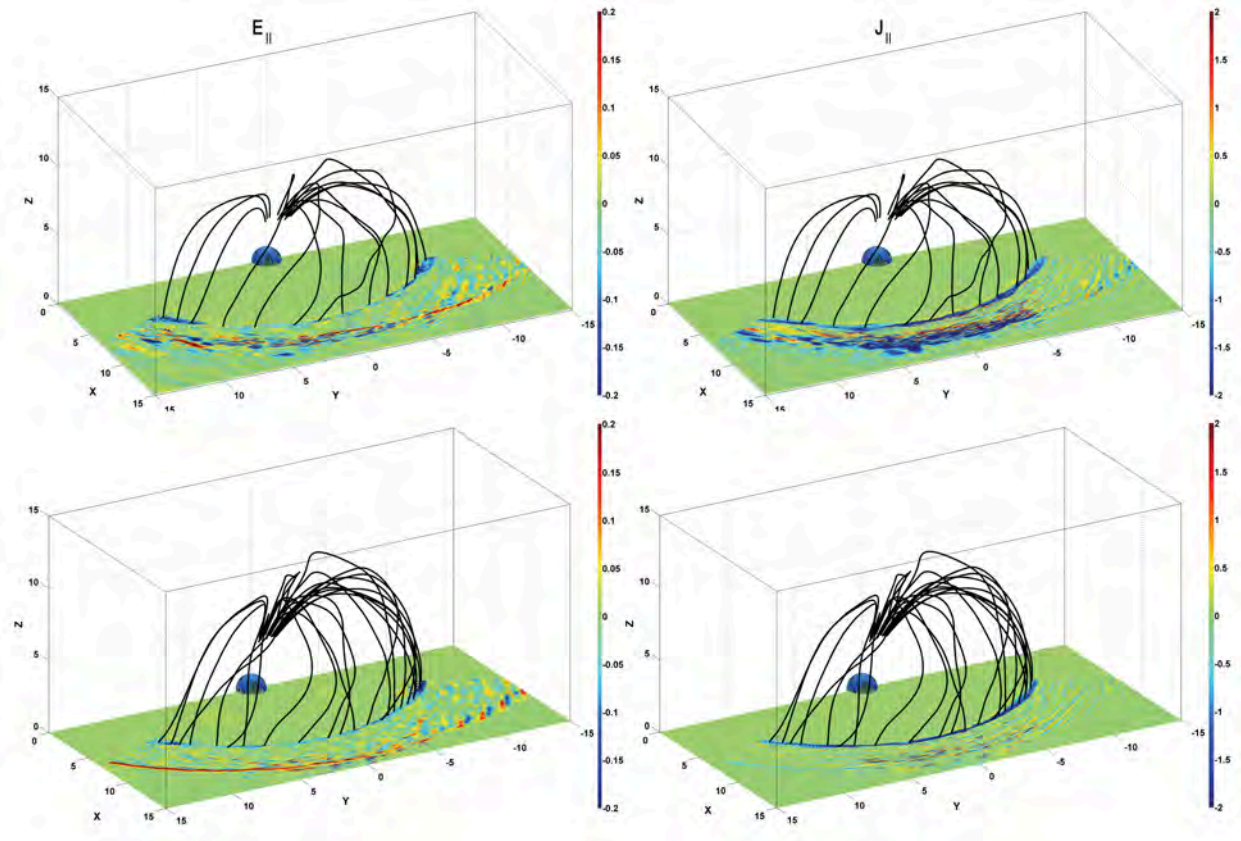

Figure 4.18: The field-aligned electric field and current density in the equatorial plane with typical field lines through the strong perturbations into the ionosphere. The top panel shows the case of $B_x = -0.866B_0$, $B_y = -0.5B_0$ and $B_z = 0$ in IMF at $t = 170$; the bottom panel corresponds to the case of $B_x = -0.470B_0$, $B_y = -0.814B_0$ and $B_z = 0.342B_0$ in IMF at $t = 90$.

4.6 Summary

In summary, 3-D global hybrid simulations of mode conversion at the dayside magnetopause under various IMF conditions have been carried out. The results are also compared with satellite observations at the dayside magnetopause. Meanwhile, 3-D broadband structures of KAWs in the downstream of the quasi-parallel shock are tracked. The global propagation and evolution of the waves are presented. The main results can be summarized as follows.

1. The structure, propagation, and time evolution of KAWs, with $k_\perp \rho_i \sim 0.5$ - 1 and satisfied with the Alfvén resonance condition $\omega \simeq k_\parallel V_A$, from mode conversion in the 3-D magnetopause are identified and presented for cases with various IMF conditions.

2. Mode conversion in the downstream of the Q-$\parallel$ shock and magnetospheric field line oscillations at Q-$\parallel$ region are more intense than those in Q-$\perp$.

3. The Alfvén mode test shows that the KAW structures satisfy the Alfvén wave polarization conditions, and the spectral analysis for the wave modes dominated by the azimuthal wave number (or mainly k_y in the case with a radial IMF) substantiate these KAW characteristics.

4. The KAW perturbations, carrying the Poynting flux and field-aligned currents, propagate poleward into the cusp region along the MPBL, and are carried away azimuthally by the convection plasma flows.

5. Due to the different flow convection speeds at various latitudes, the KAW packets expand along the north-south direction and may thus be weakened, while they may also merge with newly formed KAWs due to newly arrived compressional waves.

Chapter 5

Summary and Future Work

In summary, 3-D global hybrid simulations of mode conversion at the dayside magnetopause associated with the quasi-parallel shock have been carried out. The mode conversion from compressional waves originating at the bow shock/foreshock to KAWs is investigated. The main results can be summarized and listed below.

1. The wave structure, propagation, and time evolution in the 3-D magnetopause are presented. As the self-generated compressional wave structures propagate from the foreshock toward and impinge on the MPBL, strong $E_{\parallel}$ are excited during their interaction with the MPBL, together with the presence of correlated transverse perturbations in B_y, V_{iy}, and $J_{\parallel}$. These structures, with $k_{\perp}\rho_i \sim 0.5$ - 1, are found to be KAWs due to the mode conversion process for cases with various IMF conditions.

2. The Alfvén mode test shows that the KAW structures satisfy the Alfvén wave polarization conditions. Especially, the evolution of the KAWs lead to the generation of KAWs dominated by the azimuthal wave numbers k_y in radial IMF, consistent with the previous 3-D hybrid simulation for mode conversion in a slab geometry of the MPBL. A spectral analysis for the wave modes dominated by k_y reveals that the dependence of transverse wave polarization of $E_y(k_y)/B_x(k_y)$ on the perpendicular wave number k_y is in agreement with the theoretical results for KAWs. Besides, the wave spectra of the strongly enhanced $E_{\parallel}$ for these modes agree with those predicted by theories and simulations.

3. These KAW perturbations propagate poleward into the cusps around the MPBL, carrying the electromagnetic energy along field lines. Due to the differential flow convection speeds at various latitudes, the KAW packets expand along the north-south direction and may thus be weakened, while they may also merge with newly formed KAWs due to newly

arrived compressional waves, and carried away azimuthally by the convection plasma flows under various IMF conditions.

4. The mode conversion occurs in the MPBL due to the drastic increase of the local Alfvén speed V_A earthward. As the compressional waves approach the MPBL, the Alfvén resonance condition $\omega \simeq k_{\parallel} V_A$ is found to be satisfied at the increased V_A. The resulting KAWs are found to decay into the magnetosphere. The 3-D structures of correlated $E_{\parallel}$ and B_y are presented, indicating the spatial scales of KAWs from mode conversion process.

5. The power spectrum analyses of transverse and compressional components of the magnetic field reveal that the magnetosheath is abundant with compressional waves, while enhanced transverse waves appear around the MPBL region due to the mode conversion process.

6. Mode conversion in the downstream of the Q-$\parallel$ shock and magnetospheric field line oscillations at Q-$\parallel$ region are more intense than those in Q-$\perp$.

As seen in the preceding chapters, the current work mainly deal with the identification of KAWs and their propagations due to the mode conversion process at the dayside magnetopause under various IMF conditions. Plasma heating and transport across the magnetopause globally in the resulting KAWs, however, has not been investigated at all. Plasma heating by the KAWs from mode conversion can be hardly predicted because one cannot rule out other possibilities, such as ion Landau damping, that are mixed in the whole problem. Particle transport is extremely hard to be calculated or estimated, in the 3-D hybrid global simulations, not only because of the strong perturbation of the incident magnetic pulses in the ambient magnetic field, but because of the complication of the 3-D nature of the MPBL and the non-uniformity of the convective magnetized plasmas. Besides, the electron effects, such as electron Landau damping, are not included in the current hybrid model at all. But with the development of the computational power and impovement of the model, these issues will be casted light on in the foreseeable future.

Bibliography

[1] B. T. Tsurutani and P. Rodriguez, "Upstream waves and particles: An overview of ISEE results," *J. Geophys. Res.*, vol. 86, pp. 4317–4324, 1981.

[2] M. G. Kivelson and C. T. Russell, *Introduction to Space Physics*. Cambridge University Press, 1995.

[3] J. R. Johnson, C. Z. Cheng, and P. Song, "Signatures of mode conversion and kinetic Alfvén waves at the magnetopause," *Geophys. Res. Lett.*, vol. 28, pp. 227–230, Jan. 2001.

[4] C. C. Chaston, M. Wilber, F. S. Mozer, M. Fujimoto, M. L. Goldstein, M. Acuna, H. Reme, and A. Fazakerley, "Mode conversion and anomalous transport in Kelvin-Helmholtz vortices and kinetic Alfvén waves at the Earth's magnetopause," *Phys. Rev. Lett.*, vol. 99, p. 175004, Oct. 2007.

[5] M. J. Engebretson, L. J. Zanetti, T. A. Potemra, W. Baumjohann, and H. Luhr, "Simultaneous observations of Pc 3-4 pulsations in the solar wind and in the Earth's magnetosphere," *J. Geophys. Res.*, vol. 92, p. 10053, 1987.

[6] A. Hasegawa and L. Chen, "Kinetic processes in plasma heating by resonant mode conversion of Alfvén wave," *Phys. Fluids*, vol. 19, pp. 1924–1934, 1976.

[7] Y. Lin, J. R. Johnson, and X. Y. Wang, "Three-dimensional mode conversion associated with kinetic alfvén waves," *Phys. Rev. Lett.*, vol. 109, p. 125003, 2012.

[8] D. W. Swift, "Use of a hybrid code for a global-scale plasma simulation," *J. Comput. Phys.*, vol. 126, p. 109, 1996.

[9] S. Puri and M. Tutter, "Lower-hybrid-resonance heating of a plasma in a parallel-plate waveguide," *Nucl. Fusion*, vol. 13, p. 55, 1973.

[10] T. H. Stix and R. W. Palladino, "Experiments on ion cyclotron resonance," *Phys. Fluids*, vol. 1, p. 446, 1958.

[11] W. M. Hooke and S. Bernabei, "Direct observation of waves propagating near the lower-hybrid-resonance frequency," *Phys. Rev. Lett.*, vol. 28, pp. 709–709, Mar 1972.

[12] A. Hasegawa and L. Chen, "Plasma heating by Alfvén-wave phase mixing," *Phys. Rev. Lett.*, vol. 32, pp. 454–456, 1974.

[13] A. Hasegawa and L. Chen, "Kinetic process of the plasma heating by Alfvén wave," *Phys. Rev. Lett.*, vol. 35, p. 370, 1975.

[14] R. Cross, *An Introduction to Alfvén Waves*. Taylor and Francis, 1988.

[15] D. A. Gurnett and B. A., *Introduction to plasma physics*. Cambridge, 2005.

[16] J. L. Linsky and S. S., *Physics of Solar and Stellar Coronae: G.S. Vaiana Memorial Symposium*. Springer, 1993.

[17] J. Kohl and C. S., *Coronal Holes and Solar Wind Acceleration*. Springer, 1999.

[18] K. Russell and P. P. William, "The effect of wave-particle interactions on the propagation of cosmic rays," *Astrophysical Journal*, vol. 156, p. 445, 1969.

[19] L. Song and L. Xie, "Generation of the Alfvénic turbulence in the solar wind," *Chin. J. Geophys.*, vol. 46, pp. 621–629, 2003.

[20] B. T. Tsurutani and W. D. Gonzalez, "The cause of high-intensity long-duration continuous AE activity (HILDCAAs): Interplanetary Alfvén wave trains," *Planet Space Sci.*, vol. 35, pp. 405–412, 1987.

[21] C. Z. Cheng and J. R. Johnson, "A kinetic-fluid model," *J. Geophys. Res.*, vol. 104, pp. 413–428, Jan. 1999.

[22] J. R. Johnson and C. Z. Cheng, "Stochastic ion heating at the magnetopause due to kinetic Alfvén waves," *Geophys. Res. Lett.*, vol. 28, pp. 4421–4424, Dec. 2001.

[23] A. Hasegawa and L. Chen, "Parametric decay of kinetic Alfvén wave and its application to plasma heating," *Phys. Rev. Lett.*, vol. 36, pp. 1362–1365, 1976.

[24] C. S. Salem, G. G. Howes, D. Sundkvist, S. D. Bale, C. C. Chaston, C. H. K. Chen, and F. S. Moser, "Identification of kinetic Alfvén wave turbulence in the solar wind," *Astrophysical Journal Letters*, vol. 745, pp. 1–5, 2012.

[25] J. R. Johnson and C. Z. Cheng, "Kinetic Alfvén waves and plasma transport at the magnetopause," *Geophys. Res. Lett.*, vol. 24, pp. 1423–1426, June 1997.

[26] L. Chen and A. Hasegawa, "Plasma heating by spatial resonance of Alfvén wave," *Phys. Fluids*, vol. 17, pp. 1399–1403, July 1974.

[27] J. V. Hollweg, "Kinetic Alfvén wave revisited," *J. Geophys. Res.*, vol. 104, pp. 14811–14819, 1999.

[28] H. Grad, "Plasmas," *Phys. Today*, vol. 22, pp. 34–44, 1969.

[29] J. Tataronis and W. Grossmann, "Decay of MHD waves by phase mixing," *Z. Phys.*, vol. 261, pp. 203–216, 1973.

[30] S. Chapman and J. Bartels, *Geomagnetism*. Oxford Univeristy Press, 1940.

[31] R. T. Merrill, *The Magnetic Field of the Earth, Volume 63: Paleomagnetism, the Core, and the Deep Mantle (International Geophysics)*. Academic Press, 1998.

[32] W. H. Campbell, *Introduction to Geomagnetic Fields*. Cambridge University Press, 2003.

[33] C. P. Sonett and I. J. Abrams, "The distant geomagnetic field, 3, Disorder and shocks in the magnetopause," *J. Geophys. Res.*, vol. 68, pp. 1233–1263, 1963.

[34] M. M. Hoppe, C. T. Russell, L. A. Frank, T. E. Eastman, and E. W. Greenstadt, "Upstream hydromagnetic waves and their association with backstreaming ion populations: ISEE 1 and 2 observations," *J. Geophys. Res.*, vol. 86, pp. 4471–4492, 1981.

[35] S. A. Fuselier, M. F. Thomsen, F. M. Ipavich, and W. K. H. Schmidt, "Suprathermal He^{2+} in the Earth's foreshock region," *J. Geophys. Res.*, vol. 100, pp. 17107–17116, 1995.

[36] Y. Lin and X. Y. Wang, "Three-dimensional global hybrid simulation of dayside dynamics associated with the quasi-parallel bow shock," *J. Geophys. Res.*, vol. 110, p. A12216, 2005.

[37] S. Chapman and V. C. A. Ferraro, "A new theory of magnetic storms," *Terr. Magn. Atmosph. Elec.*, vol. 36, pp. 77–97, Jun 1931.

[38] S. Chapman and V. C. A. Ferraro, "A new theory of magnetic storms," *Terr. Magn. Atmosph. Elec.*, vol. 37, pp. 421–429, Dec 1932.

[39] C. T. Russell and R. C. Elphic, "Initial ISEE magnetometer results: Magnetopause observations," *Space Sci. Rev.*, vol. 22, pp. 681–715, 1978.

[40] C. T. Russell and R. C. Elphic, "ISEE observations of flux transfer events at the dayside magnetopause," *Geophys. Res. Lett.*, vol. 6, pp. 33–36, 1979.

[41] T. D. Phan and G. Paschmann, "Low-latitude dayside magnetopause and boundary layer for high magnetic shear 1. Structure and motion," *J. Geophys. Res.*, vol. 101, pp. 7801–7816, 1996.

[42] T.-D. Phan, G. Paschmann, and B. U. Ö. Sonnerup, "Low-latitude dayside magnetopause and boundary layer for high magnetic shear 2. Occurrence of magnetic reconnection," *J. Geophys. Res.*, vol. 101, pp. 7817–7828, 1996.

[43] Y. Lin and H. Xie, "Formation of reconnection layer at the dayside magnetopause," *Geophys. Res. Lett.*, vol. 24, p. 3145, 1997.

[44] S. A. Fuselier, K. J. Trattner, and S. M. Petrinec, "Cusp observations of high- and low-latitude reconnection for northward interplanetary magnetic field," *J. Geophys. Res.*, vol. 105, pp. 253–266, Jan. 2000.

[45] K. Nykyri, A. Otto, B. Lavraud, C. Mouikis, L. M. Kistler, A. Balogh, and H. Rème, "Cluster observations of reconnection due to the Kelvin-Helmholtz instability at the dawnside magnetospheric flank," *Ann. Geophys.*, vol. 24, pp. 2619–2643, Oct. 2006.

[46] M. Andre, A. Vaivads, and Y. V. Khotyaintsev, "Magnetic reconnection and cold plasma at the magnetopause," *Geophys. Res. Lett.*, vol. 37, p. L22108, 2010.

[47] P. Song, C. T. Russell, R. J. Fitzenreiter, J. T. Gosling, M. F. Thomsen, D. G. Mitchell, S. A. Fuselier, G. K. Parks, R. R. Anderson, and D. Hubert, "Structure and properties of the subsolar magnetopause for northward interplanetary magnetic field - Multiple-instrument particle observations," *J. Geophys. Res.*, vol. 98, p. 11319, July 1993.

[48] A. Otto and D. H. Fairfield, "Kelvin-Helmholtz instability at the magnetotail boundary: MHD simulation and comparison with Geotail observations," *J. Geophys. Res.*, vol. 105, pp. 21175–21190, 2000.

[49] H. Hasegawa, K. Maezawa, T. Mukai, and Y. Saito, "Plasma entry across the distant tail magnetopause 2. Comparison between MHD theory and observation," *J. Geophys. Res.*, vol. 107, pp. SMP 6–1 to SMP 6–8, 2002.

[50] S. V. Badman and S. W. H. Cowley, "Significance of Dungey-cycle flows in Jupiter's and Saturn's magnetospheres, and their identification on closed equatorial field lines," *Annales Geophysicae*, vol. 25, pp. 941–951, 2007.

[51] C.-P. Wang, L. R. Lyons, T. Nagai, J. M. Weygand, and R. W. McEntire, "Sources, transport, and distributions of plasma sheet ions and electrons and dependences on interplanetary parameters under northward interplanetary magnetic field," *J. Geophys. Res.*, vol. 112, p. 10224, Oct. 2007.

[52] P. Song, C. T. Russell, and C. Y. Huang, "Wave properties near the subsolar magnetopause: Pc 1 waves in the sheath transition layer," *J. Geophys. Res.*, vol. 98, pp. 5907–5923, Apr. 1993.

[53] G. Paschmann, W. Baumjohann, N. Sckopke, and T. D. Phan, "Structure of the dayside magnetopause for low magnetic shear," *J. Geophys. Res.*, vol. 98, pp. 13,409, 1993.

[54] G. Le and C. T. Russell, "The thickness and structure of high beta magnetopause current layer," *Geophys. Res. Lett.*, vol. 21, pp. 2451–2454, 1994.

[55] B. T. Tsurutani and R. M. Thorne, "Diffusion processes in the magnetopause boundary layer," *Geophys. Res. Lett.*, vol. 9, pp. 1247–1250, 1982.

[56] R. R. Anderson, C. C. Harvey, M. M. Hoppe, and B. T. Tsurutani, "Plasma waves near the magnetopause," *J. Geophys. Res.*, vol. 87, pp. 2087–2107, 1982.

[57] L. Rezeau, A. Morane, S. Perraut, A. Roux, and R. Schmidt, "Characterization of Alfvenic fluctuations in the magnetopause boundary layer," *J. Geophys. Res.*, vol. 94, pp. 101–110, Jan. 1989.

[58] M. J. Engebretson, L. J. Cahill, Jr., R. L. Arnoldy, B. J. Anderson, and T. J. Rosenberg, "The role of the ionosphere in coupling upstream ULF wave power into the dayside magnetosphere," *J. Geophys. Res.*, vol. 96, pp. 1527–1542, Feb. 1991.

[59] B. J. Anderson, S. A. Fuselier, S. P. Gary, and R. E. Denton, "Magnetic spectral signatures in the Earth's magnetosheath and plasma depletion layer," *J. Geophys. Res.*, vol. 99, pp. 5877–5891, Apr. 1994.

[60] J. H. Clemmons, F. P. Pfaff, O. W. Lennartsson, M. F. S., S. H. J., W. K. Peterson, J. D. Scudder, C. A. Kletzing, P. J. Chi, D. D. Wallis, and D. E. Larson, "Observations of traveling Pc5 waves and their relation to the magnetic cloud event of January 1997," *J. Geophys. Res.*, vol. 105, pp. 5441–5452, 2000.

[61] Y. V. Bogdanova, A. N. Fazakerley, C. J. Owen, K. B., C. N., G. B., A. M., C. P., R. H., B. J. M., L. M. Kistler, and B. A., "Correlation between suprathermal electron bursts, broadband extremely low frequency waves, and local ion heating in the midaltitude cleft/low-latitude boundary layer observed by Cluster," *J. Geophys. Res.*, vol. 109, p. A12226, 2004.

[62] C. Chaston, J. Bonnell, J. P. McFadden, C. W. Carlson, C. Cully, O. Le Contel, A. Roux, H. U. Auster, K. H. Glassmeier, V. Angelopoulos, and C. T. Russell, "Turbulent heating and cross-field transport near the magnetopause from THEMIS," *Geophys. Res. Lett.*, vol. 35, p. L17S08, 2008.

[63] T. Izutsu, H. Hasegawa, T. K. M. Nakamura, and M. Fujimoto, "Plasma transport induced by kinetic Alfvén wave turbulence," *Phys. Plasmas*, vol. 19, p. 102305, 2012.

[64] T. Tamao, "Transmission and coupling resonance of hydromagnetic disturbances in the non-uniform Earths magnetosphere," *Sci. Rep. Tohoku Univ., Ser. 5, Geophys.*, vol. 17, no. 2, p. 43, 1965.

[65] C. Uberoi, "Alfvén Waves in Inhomogeneous Magnetic Fields," *Phys. Fluids*, vol. 15, pp. 1673–1675, 1972.

[66] D. J. Southwood, "Some features of field line resonances in the magnetosphere," *Planet. Space Sci.*, vol. 22, pp. 483–491, Mar. 1974.

[67] A. Hasegawa, K. H. Tsui, and A. S. Assis, "A theory of long period magnetic pulsations. III - Local field line oscillations," *Geophys. Res. Lett.*, vol. 10, pp. 765–767, 1983.

[68] Y. Lin, X. Y. Wang, and S.-W. Chang, "Connection between bow shock and cusp energetic ions," *Geophys. Res. Lett.*, vol. 34, p. L11107, 2007.

[69] X. Y. Wang, Y. Lin, and S.-W. Chang, "Hybrid simulation of foreshock waves and ion spectra and their linkage to cusp energetic ions," *J. Geophys. Res.*, vol. 114, p. A06203, 2009.

[70] P. Kajdic, X. Blanco-Cano, N. Omidi, and C. T. Russell, "Multi-spacecraft study of foreshock cavitons upstream of the quasi-parallel bow shock," *Planetary and Space Science*, vol. 59, pp. 705–714, 2011.

[71] A. Hasegawa and K. Mima, "Anomalous transport produced by kinetic Alfvén wave turbulence," *J. Geophys. Res.*, vol. 83, pp. 1117–1123, 1978.

[72] L. C. Lee, J. R. Johnson, and Z. W. Ma, "Kinetic Alfven waves as a source of plasma transport at the dayside magnetopause," *J. Geophys. Res.*, vol. 99, p. 17405, Sept. 1994.

[73] L. Chen, "Theory of plasma transport induced by low-frequency hydromagnetic waves," *J. Geophys. Res.*, vol. 104, pp. 2421–2428, 1999.

[74] Y. Yao, C. C. Chaston, K. Glassmeier, and V. Angelopoulos, "Electromagnetic waves on ion gyro-radii scales across the magnetopause," *Geophys. Res. Lett.*, vol. 38, p. L09102, 2011.

[75] K. Stasiewicz, C. E. Seyler, F. S. Mozer, G. Gustafsson, J. Pickett, and B. Popielawska, "Magnetic bubbles and kinetic Alfvén waves in the high-latitude magnetopause boundary," *J. Geophys. Res.*, vol. 106, pp. 29503–29514, Dec. 2001.

[76] C. C. Chaston, L. M. Peticolas, C. W. Carlson, J. P. McFadden, F. Mozer, M. Wilber, G. K. Parks, A. Hull, R. E. Ergun, R. J. Strangeway, M. Andre, Y. Khotyaintsev, M. L. Goldstein, M. Acuña, E. J. Lund, H. Reme, I. Dandouras, A. N. Fazakerley, and A. Balogh, "Energy deposition by Alfvén waves into the dayside auroral oval: Cluster and FAST observations," *J. Geophys. Res.*, vol. 110, p. A02211, 2005.

[77] C. C. Chaston, C. W. Carlson, W. J. Peria, R. E. Ergun, and J. P. McFadden, "FAST observations of inertial Alfvén waves in the dayside aurora," *Geophys. Res. Lett.*, vol. 26, pp. 647–650, 1999.

[78] C. C. Chaston, J. W. Bonnell, L. Clausen, and V. Angelopoulos, "Correction to "energy transport by kinetic-scale electromagnetic waves in FAST plasma sheet flows"," *J. Geophys. Res.*, vol. 117, p. A12205, 2012.

[79] L. Chen and A. Hasegawa, "A Theory of Long-period Magnetic Pulsations, 1. Steady State Excitation of Field Line Resonance," *J. Geophys. Res.*, vol. 79, pp. 1024–1032, 1974.

[80] L. Chen and A. Hasegawa, "A Theory of Long-Period Magnetic Pulsations, 2. Impulse Excitation of Surface Eigenmode," *J. Geophys. Res.*, vol. 79, pp. 1033–1037, 1974.

[81] M. J. Engebretson, L. J. Zanetti, T. A. Potemra, and M. H. Acuna, "Harmonically structured ULF pulsations observed by the AMPTE CCE magnetic field experiment," *Geophys. Res. Lett.*, vol. 13, p. 905, 1986.

[82] M. J. Engebretson, L. J. Zanetti, T. A. Potemra, D. M. Klumpar, R. J. Strangeway, and M. H. Acuna, "Observations of intense ULF pulsation activity near the geomagnetic equator during quiet times," *J. Geophys. Res.*, vol. 93, p. 12795, 1988.

[83] J. C. Samson, J. A. Jacobs, and G. Rostoker, "Latitude-Dependent Characteristics of Long-Period Geomagnetic Micropulsations," *J. Geophys. Res.*, vol. 76, pp. 3675–3683, 1971.

[84] L. J. Lanzerotti, A. Hasegawa, and N. A. Tartaglia, "Morphology and interpretation of magnetospheric plasma waves at conjugate points during december solstice," *J. Geophys. Res.*, vol. 77, pp. 6731–6745, 1972.

[85] J. C. Samson and G. Rostoker, "Latitude-dependent characteristics of high-latitude Pc 4 and Pc 5 micropulsations," *J. Geophys. Res.*, vol. 77, pp. 6133–6144, 1972.

[86] C. Z. Cheng, "A kinetic-magnetohydrodynamic model for low-frequency phenomena," *J. Geophys. Res.*, vol. 96, pp. 21,159–21,171, 1991.

[87] Y. Lin, J. R. Johnson, and X. Y. Wang, "Hybrid simulation of mode conversion at the magnetopause," *J. Geophys. Res.*, vol. 115, p. A04208, 2010.

[88] Y. Lin, X. Wang, L. Chen, and Z. Lin, "A gyrokinetic electron and fully kinetic ion plasma simulation model," *Plasma Phys.Control.Fusion*, vol. 47, p. 657, 2005.

[89] B. B. Kadomtsev, *Plasma Turbulence*. Academic, New York, 1965.

[90] A. Hasegawa, "Method of integration of the Boltzmann equation in the presence of spatial gradients," *Phys. Fluids*, vol. 8, pp. 761–762, 1965.

[91] S. J. Buchsbaum and A. Hasegawa, "Longitudinal plasma oscillations near electron cyclotron harmonics," *Phys. Rev.*, vol. 143, pp. 303–309, Mar 1966.

[92] H. A. Antosiewicz, *Handbook of Mathematical Functions*. U.S. Government Printing Office, Washington, D. C., 1964.

[93] O. A. Pokhotelov, O. G. Onishchenko, R. Z. Segdeev, and R. A. Treumann, "Nonlinear dynamics of inertial Alfvén waves in the upper ionosphere: Parametric generation of electrostatic convective cells," *J. Geophys. Res.*, vol. 108, p. 1291, Jul 2003.

[94] S. R. Cranmer and A. A. van Ballegooijen, "Alfvenic turbulence in the extended solar corona: Kinetic effects and proton heating," *Astrophys. J.*, vol. 594, pp. 573–591, May 2003.

[95] W. X. Wang, T. S. Hahm, W. W. Lee, G. Rewoldt, J. Manickam, and W. M. Tang, "Nonlocal properties of gyrokinetic turbulence and the role of EB flow shear," *Phys. Plasmas*, vol. 14, p. 072306, Jul 2007.

[96] B. Tan, Y. Lin, J. D. Perez, and X. Y. Wang, "Global-scale hybrid simulation of dayside magnetic reconnection under southward IMF: Structure and evolution of reconnection," *J. Geophys. Res.*, vol. 116, p. A02206, 2011.

[97] B. Tan, Y. Lin, J. D. Perez, and X. Y. Wang, "Global-scale hybrid simulation of cusp precipitating ions associated with magnetopause reconnection under southward IMF," *J. Geophys. Res.*, vol. 117, p. A03217, 2012.

[98] X. Blanco-Cano, N. Omidi, and C. T. Russell, "Global hybrid simulations: Foreshock waves and cavitons under radial interplanetary magnetic field geometry," *J. Geophys. Res.*, vol. 114, p. A01216, 2009.

[99] A. V. Streltsov, W. Lotko, J. R. Johnson, and C. Z. Cheng, "Small-scale, dispersive field line resonances in the hot magnetospheric plasma," *J. Geophys. Res.*, vol. 103, pp. 26559–26572, 1998.

[100] R. G. Stone and B. T. Tsurutani, *Collisionless Shocks in the Heliosphere: A Tutorial Review*. American Geophysical Union, 1985.

[101] B. T. Tsurutani and R. G. Stone, *Collisionless Shocks in the Heliosphere: Reviews of Current Research*. American Geophysical Union, 1985.

[102] E. W. Greenstadt and M. M. Mellott, "Plasma wave evidence for reflected ions in front of subcritical shocks: ISEE 1 and 2 observations," *J. Geophys. Res.*, vol. 92, pp. 4730–4734, 1987.

[103] E. W. Greenstadt, F. V. Coroniti, S. L. Moses, B. T. Tsurutani, N. Omidi, K. B. Quest, and D. Krauss-Varban, "Weak, quasi-parallel profiles of Earth's bow shock: A comparison between numerical simulations and ISEE 3 observations on the far flank," *Geophys. Res. Lett.*, vol. 18, pp. 2301–2304, 1991.

[104] E. W. Greenstadt, F. V. Coroniti, S. L. Moses, and E. J. Smith, "Plasma wave profiles of Earth's bow shock at low Mach numbers: ISEE 3 observations on the far flank," *J. Geophys. Res.*, vol. 97, pp. 10841–10848, 1992.

[105] V. A. Thomas, D. Winske, and N. Omidi, "Re-forming supercritical quasi-parallel shocks: 1. one- and two-dimensional simulations," *J. Geophys. Res.*, vol. 95, pp. 18809–18819, 1990.

[106] D. Winske, N. Omidi, K. B. Quest, and V. A. Thomas, "Re-forming supercritical quasi-parallel shocks: 2. mechanism for wave generation and front re-formation," *J. Geophys. Res.*, vol. 95, pp. 18821–18832, 1990.

[107] D. Krauss-Varban and N. Omidi, "Structure of medium Mach number quasi-parallel shocks: Upstream and downstream waves," *J. Geophys. Res.*, vol. 96, pp. 17,715–17,731, 1991.

[108] M. F. Thomsen, J. T. Gosling, T. G. Onsager, and C. T. Russel, "Ion and electron heating at the low-Mach-number quasi-parallel bow shock," *J. Geophys. Res.*, vol. 98, pp. 3875–3888, 1993.

[109] M. H. Farris, C. T. Russel, R. J. Fitzenreiter, and K. W. Ogilvie, "The subcritical, quasi-parallel, switch-on shock," *Geophys. Res. Lett.*, vol. 21, pp. 837–840, 1994.

[110] N. Omidi, K. B. Quest, and D. Winske, "Low Mach number parallel and quasi-parallel shocks," *J. Geophys. Res.*, vol. 95, pp. 20717–20730, 1990.

[111] Y. Lin, "Global hybrid simulation of the magnetopause reconnection layer and associated field-aligned currents," *J. Geophys. Res.*, vol. 106, pp. 25451–25465, 2001.

[112] A. Nishida, *Magnetospheric plasma physics.* Center for Academic Publications Japan/D. Reidel Publishing Co., 1982.

[113] A. J. Zmuda and J. C. Armstrong, "The diurnal flow pattern of field-aligned currents," *J. Geophys. Res.*, vol. 79, pp. 4611–4619, 1974.

[114] T. Iijima and T. A. Potemra, "The amplitude distribution of field-aligned currents at northern high latitudes observed by Triad," *J. Geophys. Res.*, vol. 81, p. 2165, 1976.

[115] T. Iijima and T. A. Potemra, "Field-aligned currents in the dayside cusp observed by Triad," *J. Geophys. Res.*, vol. 81, p. 5971, 1976.

[116] M. Sugiura and T. A. Potemra, "Net field-aligned currents observed by Triad," *J. Geophys. Res.*, vol. 81, pp. 2155–2164, 1976.

[117] R. Elphic, J. W. Bonnell, R. Strangeway, L. Kepko, R. E. Ergun, J. P. McFadden, C. W. Carlson, W. Peria, C. A. Cattell, D. Klumpar, E. Shelley, W. Peterson, E. Moebius, L. Kistler, and R. Pfaff, "The auroral current circuit and field-aligned currents observed by FAST," *Geophys. Res. Lett.*, vol. 25, pp. 2033–2036, 1998.

[118] P. Nenovski, "Comparison of simulated and observed large-scale, field-aligned current structures," *Ann. Geophys.*, vol. 26, pp. 281–293, 2008.